**Vilnius Gediminas Technical University**
**Semiconductor Physics Institute**

**Frederick Walter Clarke**

# FARADAY ROTATION ANALYSIS OF NARROW GAP SEMICONDUCTORS: AN OPTICAL ALTERNATIVE TO THE HALL TEST

**Doctoral Dissertation**

**Physical Sciences, Physics (02P),**
**Condensed Matter (P260)**

**Vilnius, 2006**

Doctoral dissertation was performed between 1990 – 2005 at the U.S. Army Aviation and Missile Command, U.S. Army Space and Missile Defense Command and the Semiconductor Physics Institute (Vilnius, Lithuania)

The dissertation is defended as an external work.

Scientific Consultant:
Dr Habil Saulius BALEVIČIUS (Semiconductor Physics Institute, Physical Sciences, Physics – 02P)

**Vilniaus Gedimino technikos universitetas**
**Puslaidininkių fizikos institutas**

**Frederick Walter Clarke**

# FARADĖJAUS EFEKTO TYRIMAI SIAURATARPIUOSE PUSLAIDININKIUOSE: OPTINĖ ALTERNATYVA HOLO MATAVIMAMS

**Daktaro disertacija**

**Fiziniai mokslai, fizika (02P),**
**kondensuotos medžiagos (P260)**

**Vilnius, 2006**

Disertacija rengta 1990 – 2005 m. JAV kariuomenės aviacijos ir raketų departamente, JAV kariuomenės kosminės ir raketinės gynybos departamente bei Puslaidininkių fizikos institute.

Disertacija ginama eksternu.

Mokslinis konsultantas:
Habil. dr. Saulius BALEVIČIUS (Puslaidininkių fizikos institutas, fiziniai mokslai, fizika – 02P)

# Contents

# ACKNOWLEDGEMENTS

I would like to thank Dr. Michael Lavan, Deputy Director of the Space and Missile Defense Command (SMDC) Technical Center, Dr. Larry Lee Altgilbers, and Mrs. Gisele Wilson, Director of the Sensors Directorate, for their generous support. I am also grateful to Habil. Dr. Saulius Balevičius, head of the High Power Pulse Laboratory, Semiconductor Physics Institute, for helpful discussions and assistance, and to Dr. Nerija Žurauskienė, Semiconductor Physics Institute, for helpful assistance.

# Faraday Rotation in Narrow Gap Semiconductors: An Optical Alternative to the Hall Test

## Introduction

$Hg_{1-x}Cd_xTe$ was first synthesized at the Royal Radar Establishment, Malvern, England in 1958[1]. It has become the most important infrared detector/sensor material in the 8-12 micron atmospheric window [1-3]. It is recognized as especially valuable because its wavelength sensitivity between 3 and 30 μm is controllable through composition, the Cd mole fraction, x. But HgCdTe still has significant material quality problems, such as fluctuations of composition, Hg vacancies and variations in Cd content, Te and HgTe precipitates and inclusions, and bulk and surface instabilities due to the weak Hg-Te bond [3-4]. This decreases yield and uniformity of detectors and sensors, especially large area sensors such as focal plane arrays. Replacement of HgCdTe with harder closely related alloys, HgZnTe [5-7] has been suggested. The basic figure of merit, $\alpha/G$, where $\alpha$ is the IR absorption coefficient and G is the thermal free carrier generation rate, is close for all these materials, but overall, these materials offer no real advantage over HgCdTe. The coefficient of thermal expansion for HgCdTe is close to Si used in the detector readout circuits, reducing failures due to thermal cycling [1]. And $Hg_{1-x}Cd_xTe$ has the unique advantage of having almost the same lattice constant between $0.20 \leq x \leq 1.00$. This allows the use of a single substrate, 4% Zn CdZnTe, for growth of HgCdTe thin films.

In the 1980's and early 1990's, infrared sensors were made from bulk HgCdTe wafers. Hall or Van der Pauw tests (both referred to as Hall tests) performed on sample wafers were inadequate. The required soldered contacts effectively "dope" the material by adding carriers and depressing the mobility, giving erroneous results. More significantly, Hall tests give only an average result for the area between the contacts, which can be several square centimeters. The characteristics of a detector much smaller in area could be and often were significantly different from the tests. As a result, the only way to verify the material was to fabricate the detector and test it. A better testing method was needed. An optical test to screen carrier concentration and mobility was considered. Optical methods are fast, non-destructive, capable of examining small areas, and can be automated for integration into a production environment. Optical methods are considerably less sensitive than electrical methods like the Hall test. Generally, they are limited to carrier concentrations above $10^{15}$-$10^{16}$ $cm^{-3}$. But this is sufficient for HgCdTe for $x \leq 0.30$ and InSb, an infrared detector material with properties very similar to HgCdTe.

To use any optical method to measure carrier concentration, N, or mobility, μ, the refractive index, n, and effective mass, m*, must be known. The refractive index is carrier concentration, temperature, wavelength, and composition, i.e., Cd mole fraction, x, dependent. For example, the refractive index in moderately doped n-type InSb drops 30% from 4.0 to 2.8 between 5 μm and 17 μm [8]. The best method for determining refractive index is by measuring reflection. This would be useful for mapping HgCdTe wafers where composition and carrier concentration varies from spot to spot. But, the most difficult problem with optical screening of HgCdTe is that the effective mass at higher than liquid helium temperature is unknown. Comprehensive magneto-optical studies of HgCdTe by foremost experts, Weiler [9], and Seiler, Littler, and Weiler [10] report only electron effective mass formulas for the band edge effective mass, $m^*_{be}$, based on various band models. The results of two studies [11-12] attempting to measure the effective mass at room temperature differed significantly from the formulations. It is essential that the effective mass be known for a particular composition at the screening temperature in order to optically screen for carrier concentration. This work was performed using Faraday rotation spectra and absorption. Faraday rotation, at infrared wavelengths, is a method for measuring the ratio, $N/m^{*2}$ for carriers in semiconductors. Mobility is proportional to a ratio of Faraday rotation to absorption. Hall tests were used to determine free electron concentration, N, and Faraday rotation was subsequently used to determine m* for electrons in $Hg_{1-x}Cd_xTe$ between $0.20 \leq x \leq 0.30$ and $77K \leq T \leq 296K$. Once m* is known for a material, Faraday rotation alone can be used to screen for carrier concentration. The Faraday rotation method was developed and validated using n-type InSb, GaAs, and Si samples for which the effective masses are known, and then applied to determine m* for electrons in HgCdTe.

**Objectives**

The objectives of this effort are to develop a fast, relatively simple, nondestructive method of measuring carrier concentration and mobility in semiconductors using Faraday rotation and a ratio of Faraday rotation, θ, and absorption, α and develop a method for measuring the effective mass, m*, in narrow band semiconductors such as InSb and HgCdTe:

- Measure m* in HgCdTe vs. temperature, T.
- Measure m* in InSb, GaAs, and Si vs. T.

- Relate experimentally determined m* to theoretical band edge effective mass, $m^*_{be}$ calculations in HgCdTe.
- Measure proportionality between mobility and the ratio of free carrier Faraday rotation and absorption, $\theta/\alpha$.

**Novelty of this Effort**

Novelties of this effort include methods for measurement of Faraday rotation and effective mass in narrow gap semiconductors by:

- Device and method for increasing signal to noise ratio in $CO_2$ laser system Faraday rotation measurements.
- Device and method for producing a high resolution infrared Faraday rotation spectrum and direct measurement of m* or carrier concentration using the spectrum in semiconductors including HgCdTe and other narrow gap semiconductors.
- Development of a new method of using a ratio of free carrier Faraday rotation and absorption for simple and fast determination of free carrier mobility.
- Systematic empirical determination of m* in $Hg_{1-x}Cd_xTe$ vs. temperature and x for $0.20 \leq x \leq 0.30$ and relation to theoretical band edge effective mass, $m^*_{be}$, calculations.

**Goals of this Effort**

The goals of this effort are to develop a fast, relatively simple, nondestructive method of measuring carrier concentration and mobility in semiconductors that is suitable for automation in a high volume production environment:

- Develop optical apparatus and methods for measuring and separating Faraday rotation components, especially in narrow band semiconductors, so that free carrier concentration or m* can be determined optically at any temperature.

- Develop a means of using a ratio of two simple straight forward measurements, Faraday rotation and absorption, to determine free carrier mobility optically in semiconductors.
- Test and validate the apparatus and methodologies on semiconductors of known effective mass and mobility such as InSb, GaAs, Si and Ge.
- Systematically measure m* in $Hg_{1-x}Cd_xTe$ vs. temperature and x for $0.20 \leq x \leq 0.30$ and determine its relationship to theoretical band edge effective mass, $m^*_{be}$, calculations. This will be useful generally in the study of HgCdTe and allow determination of carrier concentration in HgCdTe at any temperature.

**Validation of Results**

The main results of this scientific research have been presented to several international conferences including SPIE August 2004, May 1996, April 1994, and the II-VI conference in October 1996. They have also been published in *The Journal of Applied Physics*, *The Journal of Electronic Materials*, and *Semiconductor Science and Technology.* Two United States patents have been issued for devices invented in this work to measure and separate Faraday rotation components used to determine m* or carrier concentration in semiconductors.

**Main propositions of the Dissertation**

(Statements to be defended)

1. The infrared Faraday rotation spectrum of a narrow gap semiconductor gives m* or carrier concentration unambiguously and enables separation of the free carrier and interband components of the Faraday rotation spectrum. This method is immune to multiple internal reflections, fast, non-destructive, and easily automated.

2. Experimentally measured values of m* in $Hg_{1-x}Cd_xTe$ for $77\ K \leq T \leq 296\ K$ and $0.20 \leq x \leq 0.30$ are higher than theoretical values calculated for electrons at the bottom of the band, $m^*_{be}$, because of the non-parabolic nature of the conduction band in this material. The difference between the two values increases with temperature as expected according to: $m^* = (4.52 \times 10^{-3}\ T + 0.78)\ m^*_{be}$.

3. Faraday rotation of free electrons can be determined separately in n-HgCdTe due to the low mobility of holes relative to electrons. Free electron absorption can be determined separate from hole absorption in n-HgCdTe doped at the $10^{17}$ $cm^{-3}$ level where electrons would out number holes by at least 100 to 1. The technique of determining electron mobility from a ratio of its Faraday rotation to its absorption can, therefore, be applied to n-HgCdTe doped at the $10^{17}$ $cm^{-3}$ level.

4. A semi-classical model of the three Faraday rotation components, interband, spin, and plasma (free carrier) partially predicts actual results. The combination of interband (without spin) and plasma components alone, appear to predict actual experimental results in HgCdTe and InSb fairly well especially at higher temperatures. The spin component appears to be inconsistent with actual results in most cases especially at higher temperatures.

**Structure of the Dissertation**

The dissertation consists of the preface, introduction, three chapters, summary and main conclusions, references, list of publications and abstract (in Lithuanian).

**Content of the Dissertation**

**Chapter I** presents an introduction and review of previous work on optical (infrared) methods of measuring carrier concentration, N, and mobility, μ, in semiconductors. These methods include: variations of the basic plasma edge reflection (spectrum) method which offers a method of determining the carrier concentration to effective mass ratio, N/m*, and the relaxation time, τ; free carrier absorption studies that provide N/m* and conductivity, $\sigma_o = Ne\mu$, where e is the electron charge; and infrared Faraday rotation due to free carriers that provides $N/m^{*2}$. The ratio of free carrier Faraday rotation, θ, to absorption, α, provides a quantity proportional to the carrier's mobility. Thus, if the proportionality were known, mobility could be determined by two fairly simple, straight forward measurements without the necessity of knowing m*, N, or the refractive index, n
. The differences in the proportionality between materials at different temperatures are due to the differences in resident carrier scattering mechanisms in the materials. Faraday

rotation is immune to scattering mechanisms in the infrared. Studies of infrared absorption that would support calculation of the proportionality between μ and θ/α in the "classical" and quantum regimes are reviewed in HgCdTe, InSb, GaAs, Si and Ge. Microwave Faraday rotation and helicon wave studies are also briefly reviewed.

**Chapter II** presents descriptions of three methods for measurement of Faraday rotation. The first describes a device for increasing the signal to noise ratio and measurement of Faraday rotation at individual wavelengths. The second describes a method of obtaining a high resolution Faraday rotation spectrum for use in measuring m*. The third describes a proposed device for obtaining usable Faraday rotation measurements in thin films. A "cold contact" technique is described for performing Hall tests without the contamination that usually results from conventional soldered contacts. Finally, n-type HgCdTe, InSb, GaAs, Si, and Ge samples used in the work are described and characterized.

**Chapter III** presents experimental results of Faraday rotation and absorption measurements in n-type HgCdTe, InSb, GaAs, Si, and Ge to determine carrier concentration and mobility. Effective mass was measured in each sample including HgCdTe. This is the first systematic measurement of m* in $Hg_{1-x}Cd_xTe$ for temperatures between 77 K and 296 K and $0.20 \leq x \leq 0.30$. A linear factor, m**, relating m* to theoretical band edge effective mass, $m^*_{be}$, calculations is reported.

**Summary and Main Conclusions** presents the general conclusions and results of the research and describes their practical applications.

**References** include articles, books, and scientific authorities consulted to compile the introduction and sources of data and information used in this work.

**List of publications** presents patents and articles in scientific journals and proceedings in which the main results of the research described in this dissertation have been published.

**Abstract** written in Lithuanian, presents a short description of the work.

# CHAPTER I

# OPTICAL NON-DESTRUCTIVE METHODS OF ASSESSING CARRIER CONCENTRATION AND MOBILITY

**(Literature Review)**

## A. Reflection Studies

As mentioned above, reflection measurements offer the best choice for independent measurement of the refractive index, n. Reflection measurements can be performed in the same chamber using the same scan as absorption. It also offers a basic method for determining the ratio of N/m* and the relaxation time, τ, independently, using the Drude-Lorentz theory for the real and imaginary parts of the dielectric constant, $\varepsilon = n_o^2$ [12-15]:

$$n^2 - k^2 = n_o^2(1 - \omega_p^2/(\omega^2 + 1/\tau^2)) \quad (1)$$

$$2nk\omega = \frac{(1/\tau)n_o^2\omega_p^2}{\omega^2 + (1/\tau)^2} \quad (2)$$

where n is the refractive index, $\omega_p$ is the plasma resonance frequency, $\omega_p^2 = N e^2/\varepsilon\varepsilon_o m^* m_o$, e is the electronic charge, $\varepsilon_o$ is the permittivity of free space, $m_o$ is the free electron mass, k is the absorption index related to the absorption coefficient, α, by $\alpha = 4\pi k/\lambda$, and λ and ω are the wavelength and frequency of the incident radiation. Reflection measurements only apply to the surface of the material to the penetration depth, $dp = \lambda/4\pi k$ [16], of the reflected radiation. For thin films, reflection is preferable for assessing carrier concentration over Hall tests when the substrate is comparable or more conductive than the film to be examined [17]. Under the condition, $\omega^2\tau^2 >> 1$, which is almost always met at infrared wavelengths, and n>>k, equations (1) and (2) become:

$$n^2 - k^2 = n_o^2(1 - \omega_p^2/\omega^2) \quad (3)$$

or

$$n^2 - k^2 = n_o^2 - Ne^2/m_o m^* \varepsilon_o \omega^2 \quad (4)$$

$$2nk\omega = \frac{(1/\tau)n_o^2\omega_p^2}{\omega^2}$$

Equation (3) shows that the refractive index decreases with increasing plasma frequency i.e., increasing carrier concentration, N, and/or decreasing m*. Figure 1 [15] shows a plot of Eq. (3) versus wavelength squared, $\lambda^2$, indicating a linear decrease in $n^2$ with $\lambda^2$, under the

approximation conditions, $k^2 = 0$, and $\omega^2\tau^2 >> 1$. Figure 2 [14-15] shows a plot of reflection versus wavelength squared for an n-type GaAs sample. Reflection shows a minimum at some $\lambda_{min}$ or $\omega_{min}$ at approximately the plasma frequency, $\omega_p$, as n goes through n = 1 according to:

$$R = \frac{(n-1)^2 + k^2}{(n+1)^2 + k^2} \quad \text{with } k = 0 \quad R = \frac{(n-1)^2}{(n+1)^2} \tag{5}$$

The refractive index continues to drop with wavelength, approaching 0, as R approaches 1. For a finite scattering time, $\tau$, the minimum reflection is not zero and the maximum reflection at the plasma frequency only approaches 1. The minimum is lowest, the spike to R = 1 or the plasma edge is sharpest, and $\omega_{min}$ and $\omega_p$ are closest for high mobility materials. In the case of high mobility materials like n-type InSb, and GaAs, $\tau$ is large and the absorption coefficient and k are small. This causes a low well defined $R_{min}$ in these materials as the refractive index, n, approaches 1. Under these conditions, m* can be

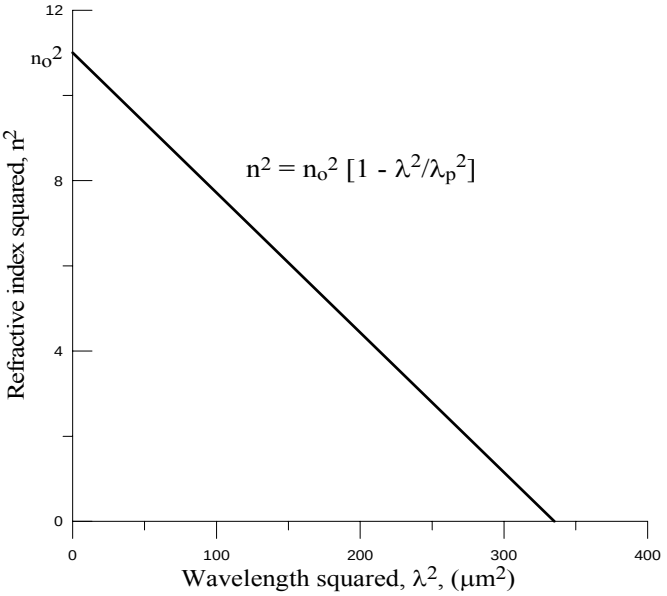


Fig. 1. Plot of the dielectric constant vs. wavelength squared of an n-type GaAs sample ($N = 2.86 \times 10^{18}$ $cm^{-3}$), showing the decrease due to free carriers. The mimimum occurs at $\lambda^2 = \lambda_p^2$. After [15].

estimated using Drude theory with n =1 and k = 0 [18]:

$$m^* \approx 4\pi Ne^2/(m_o^2\omega_{min}^2(n_o^2 - 1)) \tag{6}$$

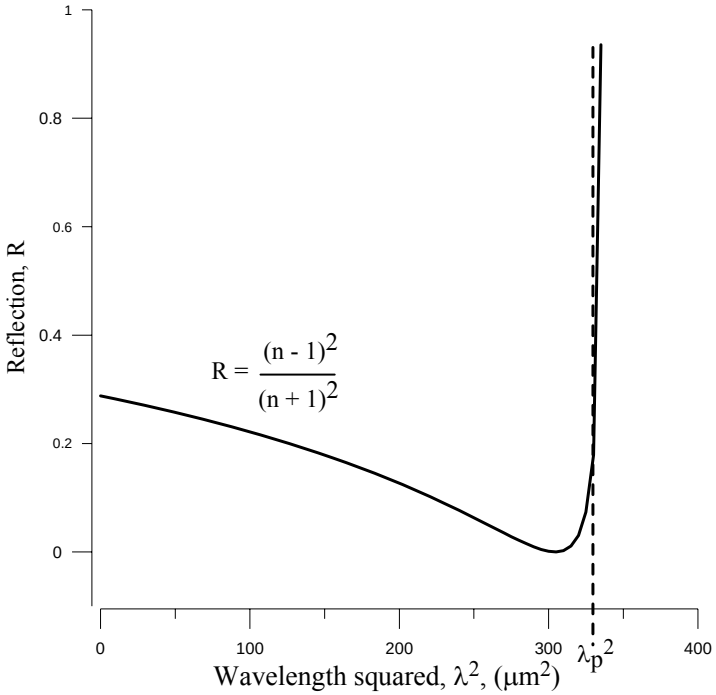


Fig. 2. Reflection versus wavelength squared for an n-type GaAs sample ($N = 2.86 \times 10^{18}$ $cm^{-3}$). The minimum occurs where the refractive index, n =1, at $\lambda^2 = (n_o^2 - 1)\lambda_p^2/n_o^2$ (see fig. 1). The plasma edge peak occurs at $\lambda_p^2$. After [15].

As scattering time gets shorter, the plasma edge broadens, and $\omega_p$ may locate along the plasma edge making it impossible to precisely determine the plasma frequency from the plot. Moss et al. [13-14] derived a correction factor, $\omega_p/\omega_{min}$, from Eq. (4) and (5) and a relationship for $\tau\omega_{min}$ derived from Eq. (1) (2) and (5) that allows precise determination of $\omega_p$, N/m*, and an approximate $\tau$ from $\omega_{min}$ and $R_{min}$. These values are plotted in figures 3 and 4. The scattering time (derived from figure 4) is only approximate for materials with a distribution of scattering times but it was used to determine mobility, $\mu = e\tau/m^*m_o$, with good results [14] for n-and p-GaAs at room temperature, which in n-type, at least, is known to have three dominant scattering mechanisms. The plasma edge reflection technique outlined by Moss et al. becomes insensitive to carrier concentrations below $10^{17}$ $cm^{-3}$ [19-20]. But it is the basis for more sophisticated reflection curve fit techniques that are sensitive to carrier concentrations on the order of $10^{15}$-$10^{16}$ $cm^{-3}$ [20-21].

Spitzer, Fan, and Whelan [8, 18] used reflectivity and absorption measurements to determine the ratio N/m* using;

$$\varepsilon = n_o^2 + 4\pi\chi = n^2 - k^2 \quad (7)$$

where $\chi$ is the electronic susceptibility due to free carriers in cgs units,

$$\chi = -Ne^2 / \omega^2 m^* m_o \quad (8)$$

This technique has the advantage of determining N/m* using the slope of a plot of $n^2$-$k^2$ vs. $\lambda^2$ of a reflectance scan anywhere in the free carrier region, not necessarily at the plasma frequency. The disadvantage of the technique is that the electronic susceptibility, $\chi$, in Eq. (8) is the electronic susceptibility for all carriers. This technique cannot be used to experimentally measure N/m* for intrinsic InSb or HgCdTe at room temperature which have equal or nearly equal numbers of holes and electrons in the $10^{16}$ $cm^{-3}$ range. The basic plasma edge technique discussed in [19-20, 22] can be used to determine carrier concentration in n-type GaAs for $5 \times 10^{17}$ $cm^{-3} \leq N \leq 8 \times 10^{18}$ $cm^{-3}$ in the free carrier region between 7 and 31 μm. Kushev et al. [23] used it in p-type $PbS_xSe_{1-x}$, a narrow-gap semiconductor.

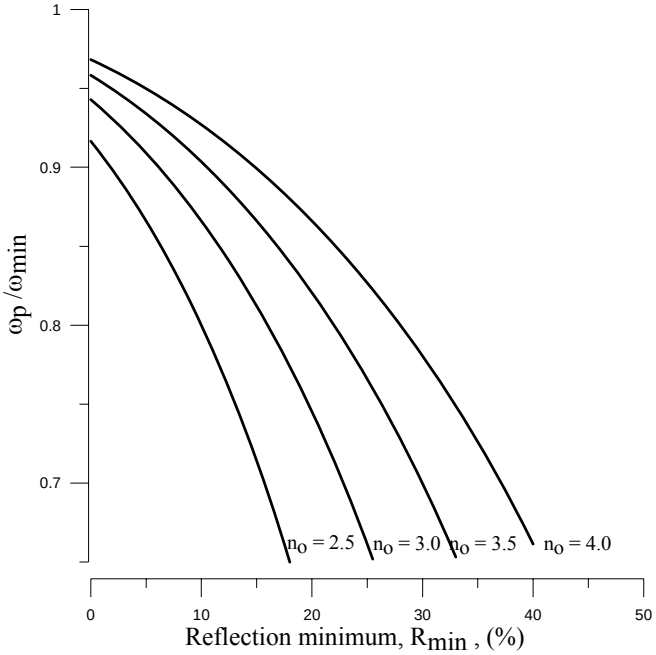


Fig. 3. The reflection minimum dependence on plasma frequency, $\omega_p$, normalized to the reflection minimum frequency, $\omega_{min}$. $n_o$ in the plot are values of the high frequency refractive index, where $n_o^2 = \varepsilon$, the dielectric constant of the material. After Moss et al. [13-14].

Thomas et al. [24] and Rheinländer [25] used the technique with a slight variation for degenerate samples to determine effective masses in n-type GaInAs ($0.87 \times 10^{18} \leq N \leq 12 \times 10^{18}$ $cm^{-3}$), InAsSb alloys in the 5 to 20 μm range, and p-type ($0.7 \times 10^{19} \leq P \leq 3 \times 10^{19}$ $cm^{-3}$) CdSb in the 5 to 30 μm range.

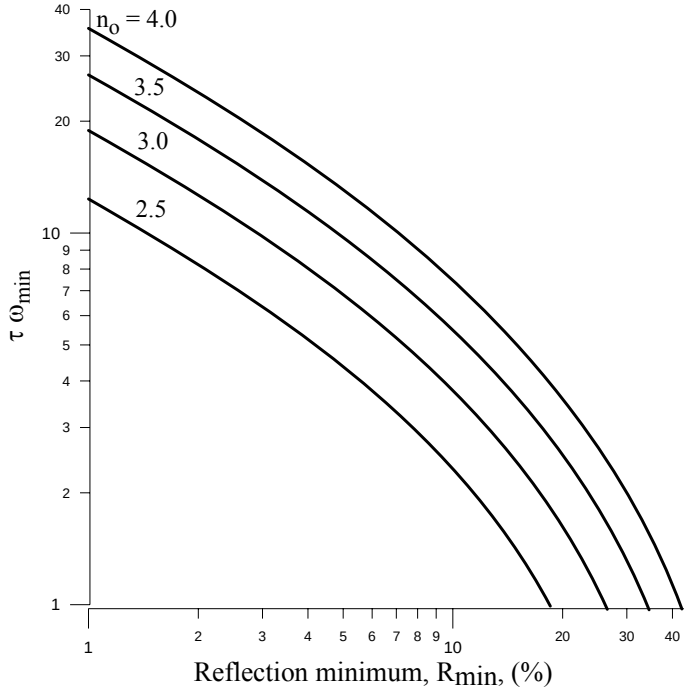


Fig. 4. Dependence of the reflection minimum on free carrier scattering/relaxation time, τ. After Moss et al. [13-14].

The close proximity of other bands, most notably, the Reststrahlen band, interferes and changes the position and shape of the reflection minimum. In this case a lattice component is added to the dielectric constant, Eq. (1) and (2) [19, 21],

$$(n - ik)^2 = n_o^2 \left( 1 + \frac{\omega_L^2 - \omega_T^2}{\omega_T^2 - \omega^2 + i\omega\Gamma} - \frac{\omega_p^2}{\omega(\omega - i/\tau)} \right) \qquad (9)$$

where $\omega_L$ is the longitudinal-optic-phonon frequency, $\omega_T$ is the transverse optic-phonon frequency, and $\Gamma$ is the phonon damping constant. The real and imaginary parts of Eq. (9) are substituted for n and k, respectively in the reflectance equation, Eq. (5). Plasmon-phonon theory predicts that reflection has two minimums, one on either side of $\omega_T$ [21]. In pure and semi-insulating GaAs the carrier concentration is very low and effectively $\omega_p = 0$.

Eq. (9) substituted into Eq. (5) can be fit to the reflectance spectrum of intrinsic GaAs to find the lattice parameters, $\omega_L$, $\omega_T$, $\Gamma$, and $n_o^2$. Holm et al. [21] used Eq. (9) and Eq. (5) to plot two sets of $R_{min}$ vs. $\omega_{min}$ curves for n-type GaAs on either side the Reststrahlen band, $\omega_T$, at 37 μm or 268 $cm^{-1}$. Plasma frequency or N/m* and τ can be determined directly from the plots using $\omega_{min}$ and $R_{min}$ measured on either side of the Reststrahlen band. The plots show higher mobilities yield lower $R_{min}$, confirming observations made by Spitzer et al. [8, 18]. Holm et al. used the plots to measure N in n-GaAs between $3 \times 10^{16}$ and $3 \times 10^{18}$ $cm^{-3}$. Perkowitz and Breecher [20] produced plots identical to Holm on the long wavelength side of the Reststrahlen band and used them to determine N in n-GaAs, between $5 \times 10^{15}$ and $4 \times 10^{18}$ $cm^{-3}$ within 4% of Hall test data. This method expands and generalizes the basic plasma edge reflection method of Moss et al. The plasma edge technique was used to determine τ, N, and m* in InSb [8,27-29], InAs/GaAs [30], n-type GaAs[18,31-39], GaInAs and InAsSb [40], n and p-type GaSb/GaSb [41], n-GaSb/GaAs [42-43], AlGaAs/GaAs [44], GaN/sapphire [45], n-type GaN/GaN [46], polysilicon/Si [47], n-Si [48-56] and HgCdTe [57-59]. Nesmelova et al. [58] measured plasma edge reflection between 2-40 microns and determined effective mass in n-HgCdTe for x = 0.17, 0.175, and 0.200 doped in the $10^{17}$-$10^{18}$ $cm^{-3}$ range. The single layer reflection equation, Eq (5), was expanded to include multiple internal reflection in a thin film on a substrate in [30]. In [49], the reflection minimum of the envelope formed by the interference fringe oscillations was used to determine carrier concentration in n-type silicon films on Si substrates. J. Kavaliauskas et al. and Eidžiūnas et al. [60-64] used Drude classical dispersion models to analyze spectroscopic reflection data between 8 and 250 microns in various surface studies of HgMnTe and HgCdTe compounds. In [60], Kavaliauskas et al. performed reflectivity analysis from 20 μm to 200 μm of p-type $Hg_{1-x}Cd_xTe$ (x = 0.21) thin films on semi-insulating CdTe substrates. The study used back reflection off the CdTe substrate in the region of the Reststrahlen band taking into account multiple internal reflections in the substrate. The parameterized model profiled the Cd mole fraction, x, the relaxation time, τ, and the plasma frequency as a function of depth of the film using a succession of etches and reflection measurements. In [61-62], Kavaliauskas et al. matched reflection models to experimental data to profile defect surfaces and free carrier profiles resulting from bombardment of the surface by a flux of positive ions. Additionally, Eidžiūnas et al. [63] used different models to analyze reflection data from samples containing small particle inclusions and aggregate precipitates in HgCdTe. In [64], reflectance of single crystal HgCdTe (x = 0.25) was analyzed using the Kramers-Kronig method to determine the

effective low frequency dielectric constant caused by optical transitions in the 0.1 to 25 micron range. The effective number of electrons per atom contributing to the transitions was calculated. Schumann and Phillips [65] examined the $\omega^2\tau^2>>1$ assumption in Eq (3). They plotted plasma reflectivity wavelength minimums between 1 μm ≤ λ ≤ 100 μm vs. carrier concentration in the $10^{18}$ $cm^{-3}$ to $10^{21}$ $cm^{-3}$ range for p-type Si, n-Si, n-Ge, and n-GaAs. Using Eq (3), they observed calculated carrier concentrations were consistently lower than actual observed values. In p-type Si, they were an order of magnitude lower at p-type dopant concentration, P = $10^{18}$ $cm^{-3}$; in n-Si they ranged from 50% to 300% lower. They were closer in n-Ge and very close to actual values in n-GaAs. The general inaccuracy of the assumption appears to be material dependent and could, perhaps, indicate a trend towards greater accuracy for higher mobility materials i.e., larger $\tau/m^*$ fraction, but this is not indicated by the authors.

## B. Infrared Free Carrier Absorption Studies

Free carrier absorption is absorption of a photon by a free electron or hole accompanied by scattering of the carrier. In the conduction band, the electron makes a transition from its initial state to a final state within the conduction band using the energy of the photon. Subsequent scattering of the electron in the crystal by various mechanisms is then necessary to transfer the momentum associated with the final state to the electron because the photon has negligible momentum. The free carrier absorption region is a region in the infrared that is usually free of interfering lattice effects generally found at wavelengths beyond the bandgap wavelength to the Reststrahlen band between 1 to 35 μm for many semiconductors, including Si, Ge, GaAs, HgCdTe, and InSb. Using $\omega_p^2 = N e^2/\varepsilon\varepsilon_o m^* m_o$, $\mu = e\tau/m_o m^*$, $\sigma_o = Ne\mu$, and $\alpha = 2\omega k/c$, in Eq. (1) and (2) with the conditions: $\omega^2\tau^2>>1$, n>>k, gives [13, 66]:

$$\frac{1}{\alpha n} = \frac{\varepsilon_o c}{\sigma_o} + \frac{4\pi^2 \varepsilon_o c^3 \sigma_o m_o^{\,2}}{e^4} \frac{m^{*2}}{\lambda^2 N} \qquad (10)$$

A plot of $1/\alpha n$ vs. $\lambda^{-2}$ in Eq. (10) is linear with slope and intercept proportional to conductivity, $\sigma_o = Ne\mu$, so that mobility, μ, and the $N/m^*$ ratio can be determined. This method was used in n-Si between 1 and 6 μm in [66-68]. The free carrier absorption, α, was normalized to the refractive index, n, because it is not a constant due to dispersion by free

carriers. This assumes that the free carrier absorption is proportional to $\lambda^2$ as predicted by classical theory in Si.

Moss [13] introduced the equation below from classical derivations of free carrier absorption and Faraday rotation:

$$\mu = \frac{C\theta}{\alpha LB} = \frac{e\tau}{m_o m^*} \tag{11}$$

where $\theta$ is the Faraday rotation, L is the sample thickness, and B is the magnetic field strength. The beauty of this equation is that, if the proportionality, C, is known, mobility can be determined with two relatively simple measurements using the same apparatus without any knowledge of $\tau$ or effective mass, m*. The normalized Faraday rotation measurement, $\theta$/LB, supplies m* and the relaxation time, $\tau$, is supplied by the free carrier absorption, $\alpha$. In the equation, $\mu$, $\alpha$, $\theta$, m*, and $\tau$ apply to the particular carrier, either electron or hole. For electron mobility, the absorption and Faraday rotation must be due to the electrons in the material alone. This is not a problem in doped semiconductors such as Si, Ge, and GaAs where the doped carriers outnumber the minority carrier by several orders of magnitude. Both HgCdTe and InSb have high intrinsic carrier concentrations in the $10^{16}$ $cm^{-3}$ range due to their small bandgaps. Faraday rotation due to holes is insignificant compared to electrons because of the large effective mass of holes compared to electrons in these materials [69]. But at n-type doping levels below $10^{18}$ $cm^{-3}$, hole absorption is significant and cannot be neglected or separated from that of electrons. This means that absorption cannot be used to screen for mobility in very nearly intrinsic HgCdTe and InSb using this equation. Another major problem with this equation is that the proportionality between $\tau$ and $\alpha$ contained in C is not straight forward. It can be measured as it was in this work. The effective mass was measured using Faraday rotation measurements, and measured absorption was combined with Hall mobilities to solve for C at a particular wavelength. C is a property of the particular material that is temperature, wavelength, and carrier concentration dependent. To calculate C the relationship between free carrier absorption and $\tau$ must be determined. This requires formulation or calculation of the free carrier absorption, $\alpha$, or the absorption cross-section, $\alpha$/N, and the mobility. This is a complex problem that is outlined from the literature below. In the classical derivation of Eq. (11), C is a constant equal to 2. Moss [13] points out that this derivation only holds if the assumption of an energy independent scattering/relaxation time holds. According to Seeger [70], the relaxation time in general has a power law dependence on the carrier's kinetic

energy, $\varepsilon$, $\tau = \tau_o(\varepsilon/k_bT)^r$, where $k_b$ is the Boltzman constant, T is the absolute temperature, and r is the power law exponent. In addition, use of a single $\tau$ is only a rough approximation according to Fan [71-73]. This requires that the formulation take into account multiple $\tau$'s corresponding to the various dominant scattering mechanisms in the material.

Due to conservation of momentum requirements, absorption cannot take place without phonon interaction, i.e., lattice vibration or imperfection or impurity. This can be seen in a typical energy band diagram of electron energy in momentum or k space. An increase in energy vertically in the diagram requires a change in momentum horizontally to follow the shape of the band. A lattice phonon is emitted or absorbed with the absorption of the photon through a virtual intermediate state [74-78]. Authors in [73-78] use a second order quantum mechanical perturbation method to calculate the absorption coefficient by adding a perturbation term to the normal or unperturbed electron and lattice wave functions. The perturbation term is similar to the unperturbed lattice term but includes the electron interaction with the photon and the wave vector of the imperfection (phonon). Haga and Kimura (HK) [76] describe two kinds of intermediate states. A direct intermediate where a photon is absorbed; the electron makes a virtual transition to a higher energy state by virtue of the photon's energy. Then a phonon is absorbed, assisting the transition by a transfer of momentum to the electron that corresponds to the higher sub-band. The order could be reversed; a phonon is absorbed and the electron is virtually transitioned to the momentum of a higher conduction sub-band, then a photon is absorbed, raising the energy of the electron. An indirect intermediate involves a third sub-band higher in energy than both the original and the final sub-band. The electron absorbs a photon and transitions to a higher energy sub-band, interacts with a phonon, and transitions to the momentum and lower energy of the final sub-band. The wavelength dependence of the absorption depends on the type of intermediate and the energy gaps between them. The proportionality between $\alpha$ and $\tau$ is similarly affected. HK formulated absorption in terms of three component absorptions due to three dominant scattering mechanisms in n-type GaAs [79], and InSb [77]; acoustic phonon, $\alpha_{ac}$, optical phonon, $\alpha_{op}$, and impurity scattering, $\alpha_{imp}$ (impurity scattering dominates in Si, and Ge [80]), where $\alpha = \alpha_{ac} + \alpha_{op} + \alpha_{imp}$. HK does not assign a particular intermediate type or even rule out that both may be present in each of the particular scattering mechanisms. HK neglected compensation, i.e. assumed $N_{imp}/N = 0$, where $N_{imp}$ is the concentration of ionized and unionized impurities. Using the indirect type intermediate, they report good qualitative results matching the shape of the experimental absorption spectra in the 1-10 micron range of n-GaAs samples with $1.3 \times 10^{17}$ cm$^{-3}$ < N < $5.4 \times 10^{18}$

$cm^{-3}$ at 300 K and 100 K. Quantum mechanical absorption cross sections for n-GaAs are given by HK in [79] for various electron concentrations. Table I shows the wavelength dependencies of the three components for a moderately doped n-GaAs sample as derived by HK and other authors.

Early work by Fan et al. [71] introduces classical expressions derived from Kronig's theory [81-82] for free carrier absorption in the 1.5 to 10 micron range. The calculated cross sections were generally significantly larger in Ge and smaller in Si than the observed values. Later, Fan et al. in [83] derived quantum mechanical expressions based on the coulombic interaction between the charged impurity and the electron for free carrier absorption due to impurity scattering that agree fairly well with observed values in Ge. These expressions were simplified by considering scattering by an ionized impurity an inverse bremsstrahlung effect. Bremsstrahlung is the deflection of an electron as it passes through the electric field of a nucleus or impurity atom [84]. Deflection or acceleration of a charged particle like an electron requires absorption or emission of a photon. Wolfe [85] added an electron screening constant to the derivations of a semi-classical and a quantum mechanical expression for the impurity scattering absorption cross section. The two expressions become the same for moderate screening and impurity concentration at low frequencies, i.e. photon energies, $\hbar\omega \ll E_f$, where $E_f$ is the Fermi energy, but where $\omega^2\tau^2 \gg 1$ still applies. Seeger [70] gives separate explicit numerical expressions for quantum mechanical calculations of mobility and absorption cross sections for several scattering mechanisms including acoustical deformation, polar optical phonon, and ionized impurity scattering. Using mechanical properties required in these expressions for InSb [86-87], GaAs [88], Ge [89-90], and Si [91-92] does not appear to give results accurate enough to be useful. These are estimates based on actual measured mobilities and absorptions in this work and absorption cross sections given in HK [77, 79] and table I.

**GaAs**

Vakulenko and Lisita (VL) [94] were the first to use HK's free carrier absorption theory to calculate mobility in an n-GaAs sample, $N = 4.5 \times 10^{17}$ $cm^{-3}$. They partially recalculated some parts of HK's quantum mechanical expressions and simplified others assuming photon energies, $\hbar\omega$, were less than the electron kinetic energy, $k_bT$. According to Dumke's [78] quantum analysis, classical and quantum mechanical expressions should give the same values at $\hbar\omega = k_bT$. Mobility can be calculated from HK absorption expressions equated to

the classical absorption expression, which is proportional to $N\lambda^2/\mu$ when $\omega^2\tau^2 \gg 1$. Perkowitz [95-96] also calculated mobility in n-GaAs using HK quantum mechanical absorption expressions in the classical expression for wavelengths between 50 μm and 500 μm. The condition, $k_bT > \hbar\omega$, corresponds to $\lambda \geq 50$ μm at 300 K and $\omega^2\tau^2 \gg 1$ corresponds to $\lambda \leq 500$ μm at 77 K. Between these wavelengths and temperatures, $\alpha_{ac}$ and $\alpha_{imp}$ are expected to have $\lambda^2$ dependencies, as required, for all carrier concentrations, N, whether degenerate or non-degenerate. The $\alpha_{op}$ component requires an additional condition, that $N \geq 10^{17}$ $cm^{-3}$ for the $\lambda^2$ dependence to hold. Perkowitz's calculations agreed with VL's calculation for their $N = 4.5 \times 10^{17}$ $cm^{-3}$ sample and Ehrenreich's [97] Kane theory mobility calculations for $N \geq 10^{17}$ $cm^{-3}$. Below $N \approx 10^{17}$ $cm^{-3}$, Perkowitz's calculations diverge a bit from Ehrenreich's theoretical calculations due to approximations in the $\alpha_{op}$ component as expected. Ehrenreich's and Perkowitz's theoretical mobility calculations agreed with n-GaAs mobility data compiled by Sze et al. [98] for $10^{17}$ $cm^{-3} \leq N \leq 10^{18}$ $cm^{-3}$. For $N \geq 10^{18}$ $cm^{-3}$, both authors' mobilities are higher by 20-30%. In [96] Perkowitz found experimental absorptions between 50 μm and 500 μm conformed to a $\lambda^2$ dependence, as long as $\omega^2\tau^2 \gg 1$ still held for these higher mobility samples, for carrier concentrations at the $10^{15}$ $cm^{-3}$ and $10^{16}$ $cm^{-3}$ levels, well below the predicted $10^{17}$ $cm^{-3}$ requirement. Dumke's [78] quantum mechanical analysis concluded that classical theory effectively overestimates the density of states and the electron population at low energies, $\hbar\omega < k_bT$ and $\hbar\omega < E_f$ for non-degenerate and degenerate semiconductors respectively. This effect is compensated by classical theory's neglect of electron energy which results in underestimation of absorption of individual electrons. As a result, these compensating errors allow accurate absorption calculations using classical theory within 8% of quantum calculations for photon energies up to 15 $k_bT$, or $\lambda \geq 3$ μm at room temperature for non-degenerate semiconductors, and within 14% for energies up to 8 $E_f$ for degenerate semiconductors.

Osamura and Murakami derived explicit expressions for the three components in n-GaAs in [99]. For the $\alpha_{ac}$ component, they used Fan's [72] expression for conductivity, $\sigma = (\varepsilon/4\pi)P_a$, where $P_a$ is the probability of absorption of a photon by an electron, and Bardeen and Shockley's [100] expression for mobility due to acoustic scattering. Fan incorporated the energy and momentum of lattice perturbations of acoustical vibrational mode phonons and the kinetic energy distribution of electrons into the Drude expression for free carrier absorption. The $\alpha_{op}$ component was derived from Visvanathan's [101] polar optical mode analysis, and $\alpha_{imp}$ was derived from the ionized impurity analysis in Visvanathan [102] and Rosenberg and Lax [103]. Walukiewicz and Jastrzebski et al. [104-106] modified HK

theory to include the compensation ratio, $N_{imp}/N$. They found that quantitative agreement between free carrier absorption measurements in [18, 107-108] and theory only occurred with compensation included. The modified theory changes proportions and wavelength dependencies of the three absorption components as shown in table I. They also derived an expression for the compensation ratio in terms of the absorption components. Jensen [109-110] used infrared absorption data in [18, 96,107] to independently calculate absorption cross sections in n-GaAs using Kane's energy band theory (referenced in [109-110]). Jensen [110] used these absorption cross sections to calculate $1/\tau$ and mobility for absorptions at wavelengths between 8.7 to 867 μm. Additional infrared free carrier absorption measurements in n-GaAs are available in [111-113].

**Table I. n-GaAs Free Electron Absorption Cross-Section Data.**

| Author [Ref] | $\alpha_{ac}$ | | $\alpha_{op}$ | | $\alpha_{imp}$ | | $\alpha/N$ ($\times 10^{-17}$cm$^2$) |
|---|---|---|---|---|---|---|---|
| HK [79] | $\lambda^2$ | 4% | $\lambda^{2.4}$ | 35% | $\lambda^{3.3}$ | 61% | 6.07 |
| VL [94] | $\lambda^2$ | 5% | $\lambda^{2.4}$ | 52% | $\lambda^{3.3}$ | 43% | 4.07 |
| Jensen [109] | $\lambda^{1.5\text{-}2.5}$ | --- | $\lambda^3$ | | $\lambda^4$ | | 3.54 |
| Walukiewicz et al. [104-106] | $\lambda^{1.5}$ | 6% | $\lambda^{2.5}$ | 65% | $\lambda^{3.5}$ | 29% | 4.59 |
| Osamura et al. [99] | $\lambda^{1.5}$ | 9% | $\lambda^{1.5}$ | 29% | $\lambda^{3.3}$ | 63% | 3.50 |

† Wavelength dependencies and percentages of free electron absorption components, and total absorption cross-section in a moderately doped n-GaAs sample, $N \approx 1\text{-}5 \times 10^{17}$ cm$^{-3}$, at 10 μm, and 300 K by various authors.

## InSb

Demidenko and von Baltz et al.'s [114-115] quantum mechanical analysis of non-parabolic bands, such as those in InSb and HgCdTe, concluded that the non-parabolicity contribution to absorption is very small for wavelengths beyond the absorption edge, $\hbar\omega \ll E_g$, where Eg is the bandgap energy, and for electron concentrations larger than $10^{17}$ cm$^{-3}$ in moderately doped n-type samples, where the electron Fermi energy, $E_f > \hbar\omega$. Jensen performed absorption coefficient calculations at 300 K in n-InSb using Kane's band theory in [116]. He attributes most of the absorption to optical phonon scattering 100 to 1 over acoustical using an acoustical deformation potential value of 7.2 eV [117]. He notes that the effect of including intermediate states in the calculation causes a heavy $\lambda^3$ dependence in the absorption coefficient. He gives the components as; $\alpha_{op}(\lambda^3)$ $0.134 \times 10^{-16}$ cm$^2$, and $\alpha_{imp}(\lambda^4)$ $0.085 \times 10^{-16}$ cm$^2$ for a total of $0.22 \times 10^{-16}$ cm$^2$ at 9 μm and $N \leq 10 \times 10^{18}$ cm$^{-3}$ compared to Kurnick and Powell's [118] measured $0.23 \times 10^{-16}$ cm$^2$. Jensen and Demidenko dispute HK's [77] results for InSb. HK calculated optical and impurity absorption components that were significantly smaller than measured absorptions in [118] and others referenced in [77]. This led them to assign a value of 30 eV to the acoustical deformation potential and to

assign acoustic scattering as the dominant mechanism over optical scattering. Acoustic deformation potential values reported in the literature for n-InSb vary from 7.2 eV [117, 119], 13-14 eV [120-122], 16.2-19 eV [123-124] to 30 eV [125]. HK used experimental absorption measurements from authors referenced in [75] that were higher than Kurnick and Powell's [118]. This led to a slightly higher calculated cross section of $0.29 \times 10^{-16}$ cm$^2$ at 9 μm at 300 K with components; $\alpha_{ac}(\lambda^2)$ $0.182 \times 10^{-16}$ cm$^2$, $\alpha_{op}(\lambda^{2.3})$ $0.075 \times 10^{-16}$ cm$^2$, and $\alpha_{imp}(\lambda^3)$ $0.034 \times 10^{-16}$ cm$^2$. Free carrier absorption in n-InSb is also presented in [126-128].

**HgCdTe**

Free carrier absorption measurements are available for n-type, p-type, and intrinsic $Hg_{1-x}Cd_xTe$ in [129], n-type [130-138], HgTe (x = 0) [139], and CdTe (x = 1) in references [110-121]. Mroczkowski and Nelson [129] measured absorption beyond the fundamental absorption edge in n- and p-type samples between $5 \le \lambda \le 20$ μm, $0.20 \le x \le 0.30$, and $77 \le T \le 300$K. They calculated the free hole cross section as $\sigma_p = 3.5 \times 10^{-16} \lambda^2$ cm$^2$ and the electron cross section, $\sigma_n = 3 \times 10^{-19} \lambda^{2.4}$ cm$^2$. Finkman et al. [130-131] developed parameterized models based on empirical data for refractive index for $0.20 \le x \le 1$, $2 \le \lambda \le 40$ μm at 300 K, and a temperature and wavelength dependent absorption model based on Urbach's empirical absorption model. The samples were intrinsic so no separate electron and hole cross sections were determined. Hougen [132] and Gopal et al. [133] used this refractive index model to analyze absorption and profile composition vs. depth in liquid phase epitaxy HgCdTe films for $0.20 \le x \le 0.30$ on CdZnTe and CdTe substrates. Several authors [134-143] have worked to quantitatively model excess absorption encountered in HgCdTe. Tian et al. [134] explained it as due to p-type inclusions where holes exist in the n-type material as majority carriers and add excess absorption with their much larger cross section. HgCdTe is a very similar material to InSb. Both possess the same dominant scattering mechanisms and absorption components, $\alpha_{ac}$, $\alpha_{op}$, and $\alpha_{imp}$. Gurauskas et al. [135] adapted the HK model [77] for n-InSb to moderately doped n-HgCdTe (x = 0.20). Hole concentration was considered negligible. Their calculations showed absorption components' dependence on wavelength varied with wavelength range and were carrier concentration and temperature dependent. Absorptions at 10 to 50 μm are in the transition region between quantum and classical. The wavelength dependencies of the three components tend to vary as $\lambda^2$ as photon energy approaches $k_bT$ or $\lambda \approx 50$ μm at 300 K. The $\alpha_{imp}$ component wavelength dependency varies as $\lambda^{3.5} - \lambda^{4.5}$ for $10^{18} \le N \le 10^{15}$ cm$^{-3}$ at 10

μm. The exponential dependence is lowest and drops fastest to $\lambda^2$ for higher doping/N in agreement with Perkowitz's [95] $N \geq 10^{17}$ cm$^{-3}$ threshold requirement for $\alpha_{imp}$ approaching $\lambda^2$ dependence at $\lambda \geq 50$ μm. Gurauskas et al. [135] used Mie light scattering/absorption theory for homogenous particles to account for absorption by Te inclusions and HgTe semimetal phase particles. The combined HK and Mie cross sections matched experimental absorption spectra fairly closely. They concluded composition fluctuations, crystal imperfections, and an unknown particle size distribution were sources of unaccounted for absorption. Dingrong et al. [136-138, 143] derived a number of models based on HK theory. In [136] they modified the $\alpha_{op}$ component to include two kinds of optical phonons present in HgCdTe [144], "HgTe" like and "CdTe" like. They based their $\alpha_{imp}$ component on Long's [145] low temperature ionized impurity analysis. Since the Fermi energy was a factor, the Moss-Burstein [13, 146-148] dopant band widening effect was taken into account. They proposed precipitates, excess compensation, and plasmons as sources of excess absorption. Plasmons are quantized units of oscillation energy of the free electron cloud [149]. In [137] they attribute excess absorption to hole interband transitions and Te and HgTe precipitates referring to Gurauskas et al. [135]. In [138, 143] they recalculate the model by eliminating precipitates and replace them with plasmons. Since plasmons are a free carrier effect, they are considered another absorption component, $\alpha_p$. Calculated absorption components and wavelength dependencies of the above models for $N \approx 10^{18}$ cm$^{-3}$ are compared in table II.

**Table II. HgCdTe Free Electron Absorption Cross-Section Data.**

| Author [Ref] | $\alpha_{ac}$ | | $\alpha_p$ | | $\alpha_{op}$ | | $\alpha_{imp}$ | | $\alpha/N$ ($\times 10^{-16}$cm$^2$) |
|---|---|---|---|---|---|---|---|---|---|
| Mrocakowski [129] | | | | | $\lambda^{2.4}$ | | | | 2.0 |
| Gurauskas [135] | $\lambda^2$ | 1% | | | $\lambda^{2.8}$ | 78% | $\lambda^{3.5}$ | 21% | 2.56 |
| Dingrong [136] | $\lambda^2$ | --- | | | $\lambda^{2.3}$ | 24% | $\lambda^{3.5}$ | 76% | 3.0 |
| Dingrong [138, 143] | --- | --- | $\lambda^{13}$ | 41% | $\lambda$ | 27% | $\lambda^{1.4}$ | 32% | 3.2 |

† Free electron absorption components, and cross-section in moderately ($N \approx 5 \times 10^{17}$ to $10^{18}$ cm$^{-3}$) doped n-HgCdTe, $0.19 \leq x \leq 0.22$, at 15 μm and 300 K. Mrocakowski et al.'s [129] experimental cross section for $N \approx 4 \times 10^{16}$ cm$^{-3}$ is included for comparison.

**Si, Ge**

Free carrier absorption measurements for Si appear in [150-160]. Isenberg et al. [150] proposed a parameterized basic Drude model (Eq. (10)) to account for free carrier anomalies seen in n-Si for $N > 3 \times 10^{16}$ cm$^{-3}$. Other authors [154-160] measured electron absorption cross sections, $\alpha/N$, between about 0.6 to $1 \times 10^{-16}$ cm$^2$ at 10 μm for $N \leq 9 \times 10^{17}$ cm$^{-3}$ and about $2 \times 10^{-16}$ cm$^2$ for $10^{18} \leq N \leq 10^{19}$ with a wavelength dependence of $\lambda^2$ for all

temperatures. Absorption cross sections for lattice and ionized impurity scattering were derived quantum mechanically and compared to experimental data for Ge by Fan et al. [83] and Rosenberg and Lax [103]. Measurements were made roughly between $5 \leq l \leq 40$ μm and $78\ K \leq T \leq 450\ K$. Both expressions fit better at high temperature (450K) were lattice scattering dominates. Rosenberg's results were off increasingly at lower temperatures. Mishima et al. [152-153] used the Drude linear plot method above in n-poly-silicon. They measured considerably higher optically measured mobilities than Hall mobilities. This was attributed to grain boundaries in the poly-silicon [66,161-162]. Theoretical expressions for absorption components are presented in [71-73, 80, 83, 163].

## C. Faraday Rotation and Other Magneto-Optical Studies

Faraday rotation is the rotation of the plane of polarization of light as it passes through a material in the presence of a magnetic field parallel to the light. It is a dispersion effect (dependence of refractive index, n, on the wavelength/frequency of light) related to the cyclotron resonance absorption of electrons and holes between the right and left circularly polarized components of a plane polarized light beam [164]. The two components correspond to frequency arguments, $\omega + \omega_c/2$ and $\omega - \omega_c/2$, where $\omega_c = Be/m_o m^*$, is the cyclotron resonance frequency. Faraday rotation is defined by:

$$\theta = (\omega L / 2c)(n_- - n_+) = (\omega L / 2c)[n(\omega - \omega_c / 2) - n(\omega + \omega_c / 2)] \qquad (12)$$

where $n_-$ and $n_+$ are refractive indexes for opposite circular polarizations and the equation on the right uses notation intended as $n = f(\omega)$ in the bracketed term. The well known formula for Faraday rotation for free carriers in the infrared region applies for $\omega\tau \gg 1$:

$$\theta = \frac{e^3 BL}{8\pi^2 c^3 \varepsilon_o n m^{o2}} \frac{N\lambda^2}{m^{*2}} = \frac{e^3 BL}{2\pi c^4 n m_o^{\ 2}} \frac{N\lambda^2}{m^{*2}} \qquad (13)$$

MKS units cgs units

where $e = 1.602 \times 10^{-19}$ C in MKS units and $e = 4.8 \times 10^{-10}$ esu, and $\varepsilon_o = 1$ in cgs units. The equation was first derived by Mitchell [165] then by Moss et al. [13, 166-167] and others [15, 168-169] using the classical Drude approach. Faraday rotation is a form of the Hall

effect. Klinger et al. [170] derived the equation in terms of elongation constants of the crystal, Verdet constant, V, where Faraday rotation is given by, $\theta = VBL$, and the Hall constant, $R_H = r/Ne$, where r is the material dependent Hall scattering factor. Experimental methods for infrared Faraday rotation measurements accurate to 1/100 and 1/60 of a degree have been devised and are presented in [171-172] respectively. Faraday rotation is a nonreciprocal effect [173]. It is additive if it is internally reflected in the sample [164]. This basic property is used to double Faraday rotation in a simple device in [173]. In measuring Faraday rotation it is usually regarded as an interfering effect known as multiple internal reflection (MIR) which must be compensated for in thin low absorbing samples. The effect is analyzed in detail and compensating formulas derived in several references [15, 164, 174-179]. Faraday rotation in semiconductors has two main components: one due to free carriers, called the plasma component, and one due to transitions across the bandgap, called the interband component. In narrow-gap semiconductors the interband component is large and significant well beyond the band edge. Separation of the free carrier component so that Eq. (13) can be used to determine effective mass or carrier concentration has been problematic and the reason m*, has so far, not been measured systematically in HgCdTe at temperatures above liquid helium temperature.

When absorption is present, the beam becomes elliptically polarized due to a differential absorption between the two components [70, 171].

$$E = (\omega L / 2c)(k_- - k_+) \qquad (14)$$

where $k_-$, and $k_+$ are the indexes of absorption for the two polarizations. Ellipticity, E, is defined as the ratio of the minor axis to the major axis. The angle between the initial polarization and the major axis is the Faraday rotation angle. Ellipticity is independent and has no effect on the Faraday rotation angle. General expressions for Faraday rotation and ellipticity have been derived by Donovan and Webster [180-182] for all frequencies using Drude and the Boltzman transport equation. The Boltzman transport equation relates the rate of change of the electron distribution function caused by an electric field in the material to the rate of change of the electron distribution function caused by collisions with phonons, imperfections, other carriers, or any other scattering mechanism [183]. Bennet et al. [184] derived general quantum mechanical expressions for Faraday rotation in transmission and reflection (the magneto optical Kerr effect ). Infrared Faraday rotation, where $\omega\tau \gg 1$ almost always applies, is independent of the particular scattering mechanisms and $\tau$ [13, 15, 166-

169, 185-186]. Ellipticity on the other hand is explicitly dependent on scattering and $\tau$ [70, 184, 186]. The ratio of $E/\theta$ at infrared wavelengths where $\omega\tau \gg 1$ applies is $2/\omega\tau$. At microwave frequencies where $\omega\tau \ll 1$ the ratio flips and $E/\theta \approx \omega\tau$. The two techniques in combination can be used to measure $\tau$ and $N/m^{*2}$.

Magneto-optical experiments in semiconductors began in 1956 [167]. Application of $\pm$ B to plasma edge reflection causes two reflection minimums, corresponding to the two opposite polarizations, to appear at $\pm \omega_c/2$ on either side of the B = 0 reflection minimum [15, 167, 188-191]. Corresponding extrema, positive and negative, appear in the Faraday rotation and ellipticity spectra at roughly the same points. The Voigt effect [13, 70, 192-194] is possibly a worthwhile complement to Faraday rotation in the study of HgCdTe. This is rotation of the plane of polarization with the poles of the magnet and the lines of the magnetic field at 90˚ to the light beam. A Faraday rotation set up would require some modification to accommodate this measurement. This would mainly require changes in the sample cryostat and mounting. The cryostat would need to be redesigned to minimize the gap in the magnet in the Voigt geometry, and the mounting would require that the cryostat be moved up and down and side to side from the top of the magnet, rather than from the side as in the Faraday geometry. The Voigt effect provides $N/m^{*3}$ rather than $N/m^{*2}$. Between the two techniques, N and m* can be determined entirely optically. Moss [13] notes that the effect has only been observed in a few favorable materials, InAs, GaAs [192], and InSb [193], but should be observable in a high mobility material like HgCdTe. The ratio of Voigt to Faraday rotation for, $\omega > \omega_p, \omega_c, 1/\tau$, is $e\lambda B/2\pi c^2 m^*$. This works out to a factor of 15 times less signal in n-InSb [193] at 10.6 microns and 1T. The signal, of course, increases with higher fields and longer wavelengths. The problem with increasing the magnetic field in these high mobility materials is their heavy dependence of m* on magnetic field. This was shown by Teitler and Palik [194] in InAs for B up to 7T and in HgCdTe by Weiler [9] in cyclotron resonance measurements up to 16T. The magnetic field dependence is more or less linear and extrapolation of an m* vs. B plot yields the low field m* as the intercept.

**HgCdTe**

A few Faraday rotation studies [11-12, 159(4*), 195-197(5*), 199(1*), 200(2*), 201(3*), 202(6*), 203-204(7*)] have been conducted in HgCdTe for $0.20 \leq x \leq 0.30$ and $x = 0.37$ [11]. These are mainly concerned with mapping carrier concentration and composition (Cd mole fraction, x) across samples of this difficult material. The effective mass was

unknown except for several cyclotron resonance studies at 4.2 K, many referenced in a comprehensive review on HgCdTe in Dornhaus and Nimtz [205]. Elizarov et al. [12, 195] knew low temperature studies and theoretical band edge effective mass calculations were inadequate for carrier concentration profiling at higher temperatures given the non-parabolic bands of HgCdTe. Balkanski and Amazallag [186] note that the effective mass at temperature and at different carrier concentrations is only equal to the band edge or very low temperature effective mass for parabolic bands. For non-parabolic bands, m* depends on the carrier density through the Fermi energy. Elizarov made Faraday rotation measurements between 4 and 13 microns and found effective masses to be about a factor of two larger at 295 K than band edge effective mass calculations. Instrumentation for measuring high resolution infrared rotation spectra between 5 and 20 microns were developed in [159(4*), 197(5*)-198, 200(2*), 201(3*)] and used to determine effective mass in [199(1*), 200(2*), 202(6*)]. The resonant spin flip Faraday rotation component found in HgCdTe and InSb was studied in HgCdTe in [203-204(7*)] and in InSb [206]. It was proposed in [204(7*)] as a promising effect for carrier concentration screening. These studies are analyzed later in the HgCdTe section.

**InSb**

Infrared (2-25 μm) Faraday rotation has been used to determine m* and its carrier concentration and temperature dependence in n-InSb [147, 200(2*), 202(6*), 207-211]. The effective mass is an important parameter in the study of energy band structure [164]. It is directly related to the interband momentum matrix element, P, and is inversely related to the curvature of the energy, E, versus momentum, k, curve of the conduction band. The momentum at the Fermi level, $k_F$, is directly related to the carrier concentration, N, so determination of m* at several concentrations can be used to determine, $(dE/dk)_F$, the curvature at the Fermi level using $1/m^* = (1/\hbar^2\ k_F)(dE/dk)_F$ for degenerate non-parabolic bands [207-211]. This curve can be integrated numerically to give the E vs k curve. The curvature of non-degenerate non-parabolic bands such as those in InSb and HgCdTe, can also be determined this way but the E-k relationship must be known [207].

**Si, Ge**

Infrared Faraday rotation studies in Si and Ge are published in [211-216] and [217-221] respectively. Ukhanov et al. [185, 212] measured Faraday rotation in Si, Ge, InSb, InAs,

and GaAs at wavelengths beyond the bandgap to determine effective mass and gives a general review of Faraday rotation in semiconductors in [185]. Walton et al. [213] used a combination of dispersion from reflection measurements, and Faraday rotation in the 1-25 micron range at 293 K to determine carrier concentration and effective mass entirely optically. They and others [214-215] used a $\theta/LB = a\lambda^{-2} + b\lambda^{2}$ model to describe total Faraday rotation. The interband component was represented as $a\lambda^{-2}$ and the free carrier component as $b\lambda^{2}$. Walton obtained a straight line plotting $\theta\lambda^{2}/LB$ vs. $\lambda^{4}$, in $\theta\lambda^{2}/LB = b\lambda^{4}+a$. This gives $N/m^{*2}$ in the slope, b, and the interband component as the intercept, a. Stramska et al. [216] measured Faraday rotation and ellipticity in n and p-type samples. Similar interband plots were obtained for Ge in [218-219]. Walton et al. [220] measured infrared Faraday rotation between about 3 and 14 microns in uniaxially stressed samples in an attempt to measure m* anisotropy. They observed that compressive stress reduced the interband component and increased the free carrier component. Boswarva and Lidiard [221] calculated components of interband rotation in terms of the theoretical interband energy transitions and used these to determine the g factors in Ge.

**GaAs**

Cardona [222] measured plasma edge reflection and Faraday rotation in GaAs between 1 and 10 microns to measure m* as a function of temperature and N. He noted the sign of the interband component is the same as that due to free electrons. The sign is that of the combined interband g-factors for holes and electrons [186]. Cardona showed using energy band calculations that the effective mass obtained using Faraday rotation is identical with the effective mass obtained in reflectivity measurements. His data indicate a positive offset to the rotation. Mashukov [223] attributed the offset to interband transitions that do not go to zero but tend to approach a constant value with wavelength. Alfano and Baird [224] attributed the offset to multiple internal reflections (MIR) in the sample. They measured rotation between 1-10 microns and obtained a straight line plot of rotation vs. $\lambda^{-2}$ between 2-7 microns using the interband model mentioned above. They introduced a simple expression to correct for MIR. Other simple expressions for MIR were introduced in [217, 225]. According to these formulas, MIR accounts for about 2-9% excess rotation in GaAs for $N = 10^{17}$ - $10^{18}$ $cm^{-3}$ around 10 microns for a 0.5 mm thick sample. Ukhanov [226] measured m* as a function of N. He observed a linear increase of the offset with N. Other m* determinations using infrared Faraday rotation were conducted in [227-229]. Lax and

Mavroides give a comprehensive treatment of interband magneto-optical theoretical models and effects in [230]. This includes a model showing the interband component approximately proportional to $\lambda^{-2}$ for wavelengths sufficiently far from the energy gap.

## D. Mobility

### Si, Ge, GaAs

Early theoretical mobility models in Si and Ge were developed by Conwell et al. [231-234], Brooks [80, 235], Bardeen and Shockley [100] and others [163, 236]. These are expressions for the two dominant scattering mechanisms in Si and Ge; lattice and ionized impurity scattering [231-234], neutral scattering including frozen out ionized impurities [236], intervalley scattering [163], screening of ionized impurities by free electrons [85] and other lesser effects [235]. Karpus et al. [237-239] formulated momentum relaxation time expressions for the two dimensional electron gas (2-DEG) structures that exist at the AlGaAs/GaAs interface [237-238] and in one dimensional electron gas in GaAs quantum wires [239]. Karpus showed that acoustical deformation phonon scattering is dominant in both structures at low temperatures. Theoretical results matched experimental data fairly closely in the 2-DEG between 10 K and 50 K [238], where scattering by acoustical phonons dominates. Si, Ge, and GaAs, are well characterized materials theoretically and empirically. Mobility models for these materials have been incorporated in highly successful device simulation programs such as HP-SPICE and others for many years. Mobility models are available for these materials that can be tailored for the particular application; i.e. carrier concentration, temperature, etc. for use in Eq. (11).

### InSb

Kane derived the band structure for pure InSb using the quantum k-p method in [240]. It was used as the basis of mobility models derived in [241-245]. Ehrenreich [241] concluded optical polar scattering dominates in pure InSb. Pfeffer et al. [242] and Zawadzki et al. [241-242] include ionized impurity scattering for N up to $10^{19}$ $cm^{-3}$. Zawadzki's results show ionized impurity scattering dominates for $N > 10^{17}$ $cm^{-3}$ and acoustical deformation scattering surpasses optical phonon scattering for $N > 2 \times 10^{18}$ $cm^{-3}$ at room temperature. The non-parabolic nature of the conduction band manifests itself in wave

functions of the periodic lattice structure that retain a large p-like orbital component. Several authors derived mobility models by approximate solution of the Boltzmann transport equation [246-251]. Authors in [243-245, 249-250] simplified the solution by assuming elastic scattering and unique definable relaxation times (relaxation time approximation and Matthiessen's rule). Howarth and Sondheimer [246] point out that it is impossible to define a unique relaxation time for optical phonons at low temperature. Litwin-Staszewska et al. [247] wrote that optical phonon scattering must be considered non-elastic and a relaxation time can be introduced only at high temperatures (> 300 K) due to phonon energy on the order of electron energy at room temperature [241]. Pfeffer's results show the variational/successive approximation solution to the Boltzmann equation yields 20% higher mobilities over the relaxation time approximation for all considered electron concentrations. Another source of variance in these models is uncertainty in the value of the acoustic deformation potential used, between 7.2 eV and 30 eV by the various authors. Semi-classical and empirical curve fit models are derived in [252-259], scattering by un-terminated bonds for surface mobility in [253], dislocation scattering in [254], scattering in small dimensions for devices in [256], and InSb/CdTe quantum wells in [259].

**HgCdTe**

Dornhaus et al. [205] and Miles [260] give general surveys of mobility studies in HgCdTe. Boltzmann equation models using a variation technique are derived in [261-265] and relaxation approximations in [266-268]. Nimitz et al.[267] used the relaxation model derived for InSb in [244]. The main differences between n-InSb and n-HgCdTe models are the positive temperature coefficient of the HgCdTe bandgap, two phonon mode [144] scattering (essentially optical) [262-263], alloy scattering due to the valence band offset between HgTe and CdTe [266], and structural anomalies. Empirical and semi-classical models are derived in relatively defect free n-HgCdTe in [145, 269-273]. Kane band structure based mobility models are available for n-HgCdTe in [274-276] and related alloys in [5-7, 277-281]. Nag [265], using Rode's method, estimates the relaxation approximation is off 10-15% at temperatures between 30 K and 300 K where two phonon scattering dominates. At temperatures below 30 K the lower temperature phonon dominates. At temperatures above 300 K the energy dependence of the scattering times of the two phonons are similar and the model gives similar results to Mathiessen's rule. Rode [282] writes relaxation methods are useful only qualitatively. Mobilities of n-HgCdTe samples with p-

type inclusions are reported in [283-285] and modeled in [286-289]. Anomalous Hall mobilities in n-type samples with p-type cores are analyzed in [290]. Results show that the Hall coefficient, $R_H$, and mobility are as expected for the n-type regions alone for temperatures above 77 K.

Absorption is the culprit for the complexity of "C" in Eq. (11) for $\hbar\omega > k_bT$. This is the quantum regime. Measurements in the IR will come closest to the classical equation at higher temperatures and diverge increasingly at lower temperatures. The above survey shows that adequate models for absorption and mobility exist for formulating the proportionality if desired.

## E. Faraday Rotation at Long Wavelengths and Helicon Waves

Several authors [70, 169, 174, 180, 291-296] have developed the theory of Faraday rotation and ellipticity using Drude-Zener models at long wavelengths where $\omega\tau \ll 1$ in the $\omega_c\tau > 1$ and $\omega_c\tau < 1$ regions. Palik and Holm [291] give a general review on optical characterization methods including microwave Faraday rotation. Rau et al. [292] derived Faraday rotation and ellipticity, E, in the $\omega_c\tau > 1$ region as:

$$\theta = \frac{1}{2}\left(\frac{\mu_o}{\varepsilon_o}\right)^{\frac{1}{2}}\left(\sigma_o\mu\,\frac{B}{\sqrt{\varepsilon}}\right)d$$

$$E = \frac{1}{2}\left(\frac{\mu_o}{\varepsilon_o}\right)^{\frac{1}{2}}\left(\sigma_o(\mu B)\,\frac{(\omega\tau)}{\sqrt{\varepsilon}}\right)d \qquad (15)$$

where $\mu_o$ is the permeability, $\varepsilon$ is the dielectric constant at the applied frequency, and an electron velocity independent relaxation time, $\tau$, is assumed. The Faraday rotation equation is independent of frequency for $\omega\tau \ll 1$. These equations have the advantage of being able to determine mobility and relaxation time directly without knowledge of m* if either carrier concentration, N, or conductivity is known. Stephen and Lidard [169] derived general expressions for Faraday rotation in both the $\omega_c\tau > 1$ and $\omega_c\tau < 1$ regions. Faraday rotation in the $\omega_c\tau < 1$ region is proportional to $B\omega^{1/2}\mu^{3/2}N^{3/2}$. Rau's equations were derived for low absorption losses. Furdyna and Broersma [293] derived Faraday rotation and ellipticity expressions in the $\omega_c\tau > 1$ and $\omega_c\tau < 1$ regions for large losses. Bouwknegt and Volger [297], using Champlin's [295] theory, developed a method for eliminating MIR in microwave Faraday rotation measurements of n-Ge that caused significant oscillations as a function of

sample thickness for thicknesses less than twice the skin depth, $\lambda/4\pi k$. Goldey et al. [294] developed averaging methodologies for more complex magneto-optical formulations involving velocity dependent relaxation times. Baldwin et al. [298] reported Faraday rotation measurements in n-Si and n-Ge at $\omega = 2.17 \times 10^{11}$ rad/s using a 15 T magnet pulsed at 10.6 kHz. Portis [299] used microwave Faraday rotation to measure mobility in CdS and microwave Faraday rotation and ellipticity was measured in n-InSb in [296-298] to determine mobility. Zengin et al. [303] and Ogawa et al. [305] used a curve fit to microwave Faraday rotation vs. magnetic field data for $\omega_c\tau > 1$ to determine $\tau$ and N and m* (at 77K) in n-InSb. Allen [304] gives a method for measuring small angles of microwave Faraday rotation sensitive to $10^{-4}$ degrees.

For frequencies below the plasma edge, $\omega<\omega_p$, plasmas such as the free electron gas in a semiconductor have a negative permittivity and are opaque. A magnetic field induces a conditional transparency for one circular component of a linearly polarized wave for $\omega_p^2/\omega > \omega_c > \omega, 1/\tau$. These are helicon waves named for the helical path the rotating electric field vector of the radiation takes through the material [305-310]. The other polarization is severely damped and is heavily absorbed and/or reflected until the magnetic field is increased to the magneto-plasma edge where the permittivity becomes positive and transparency of the other mode rises sharply at $B = Ne/\omega\varepsilon_l$, where is $\varepsilon_l$ the dielectric constant of the lattice. The front and back surfaces of the sample set up a Fabry-Perot oscillatory transmission resonance due to multiple internal reflections in the sample. The sample transmits a series of larger and larger maxima as a function of magnetic field and at an integer number of half wavelengths, $\lambda_H = 2\pi B^{1/2}/(\omega\mu_o Ne)^{1/2}$, where $\lambda_H$ is the helicon wavelength. Larger, sharper, higher resolution (period is doubled) peaks are achieved by interference (Rayleigh scattering ) of the helicon wave with a reference signal. Helicon waves require a single charge carrier or a situation where one charge carrier has a much higher mobility than the other such as for electrons in n-InSb at room temperature [307].

Laurinavičius et al. [311-313] gives two simple straight forward equations for carrier concentration and mobility in terms of the absolute amplitude, $A_M$, $A_{M+I}$, and magnetic field value, $B_M$, $B_{M+I}$, of the Mth order and the Mth + I order transmission peaks;

$$N = \frac{\varepsilon_o \pi^2 c^2 I^2}{e\omega d^2} \frac{1}{\left[ \left(B_{M+I}\right)^{\frac{-1}{2}} + \left(B_M\right)^{\frac{-1}{2}} \right]^2}$$

$$\mu = \frac{\pi I \left[ \left(B_{M+I}\right)^{\frac{-3}{2}} - \left(B_M\right)^{\frac{-3}{2}} \right]}{2 \ln \left[ \frac{A_M}{A_{M+I}} \left( \frac{B_{M+I}}{B_M} \right)^{\frac{1}{2}} \right] \left[ \left(B_{M+I}\right)^{\frac{-1}{2}} - \left(B_M\right)^{\frac{-1}{2}} \right]} \qquad (16)$$

The difference between Hall measurements and the helicon measurements of N was smallest for the smallest ratios of $B_M/B_{M+I}$, i.e. generally the closer the peaks at $B_M$ and $B_{M+I}$ to each other, the smaller the error. The opposite was the case for mobility measurements. Helicon waves are severely damped for components not parallel to the magnetic field. Laurinavičius et al. mapped beam narrowing observed for helicon waves produced by a 35 GHz signal and proposed this mechanism for high resolution material probes. Wiley and Dexter [314] used helicons in HgCdTe for $0.135 \leq x \leq 0.203$ to measure electron concentration, effective mass, and mobility using 23 GHz and 70 GHz signal frequencies at 77 K and 1.3 K. Their effective mass measurements were close to the theoretical band edge effective mass predicted by Kane's theory (referenced in [314]). Brazis et al. [315-317] gives a comprehensive review of microwave effects including helicon waves in intrinsic and extrinsic narrow band semiconductors. In [317] Brazis and Furdyna analyzed microwave plasma effects in n-InSb. The experiments were carried out at 35 GHz between 80 and 300 K using a quarter wave plate in front of the sample. They observed a non-resonant minimum in reflectivity that varied with magnetic field. The minimum depends on two terms where m* and N occur separately and can be used to profile both by varying the frequency.

# CHAPTER II

## EXPERMENTAL METHODS AND SAMPLES

## A. Measurement of Faraday rotation at individual wavelengths: Modified High Sensitivity Infrared Polarimeter

Figure 5, taken from patent [318(9*)], shows a block diagram of the experimental apparatus used to measure Faraday rotation in samples at a single wavelength [202(6*)].

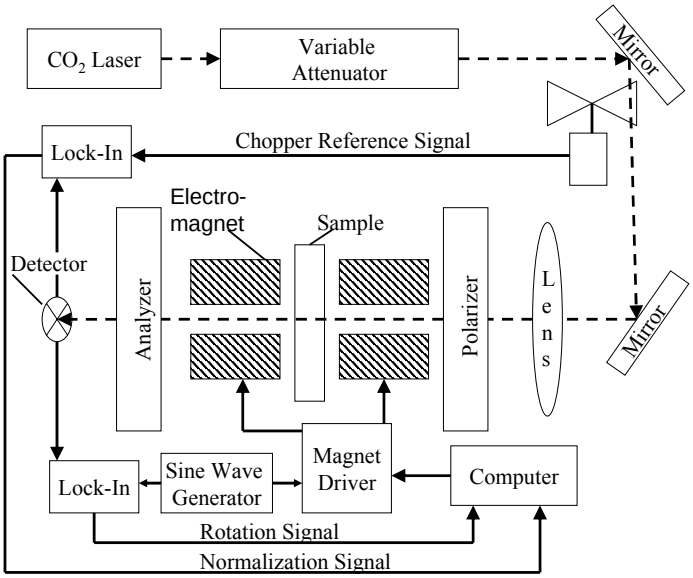


Fig. 5. Block diagram of patent "Modified High Sensitivity Infrared Polarimeter" [318(9*)].

Its operation has been described in patents [318(9*)-319] and in reference [320]. The beam of a $CO_2$ laser, tunable in this case from 9.3 microns to 10.6 microns, is passed through a variable attenuator, where the intense beam from the laser is adjusted to an intensity suitable for the other elements in the apparatus. It is reflected off a mirror through a chopper. The chopper, set at 100 Hz, provides a reference signal to the lock-in amplifier or synchronous detector for extraction of the chopped beam normalization signal from the detector. The lock-in amplifier greatly enhances the signal to noise ratio of the extracted signal. The laser beam is redirected after leaving the chopper by a second mirror through a zinc selenide lens

that focuses the beam onto a polarizer. The beam, now linearly polarized, passes through one side of a circular electromagnet with a hole in the middle for the beam, through the sample, and out the other side of the electromagnet. The electromagnet was made from two halves of a commonly available electromagnetic pipe valve and was capable of fields of 0.1-0.35 tesla, depending on magnet current, frequency, and the air gap between the halves. The beam finally passes through an analyzer, then to the detector. The magnet is pulsed with a sine wave generator. The sine wave generator is also fed as a reference to another lock-in amplifier for extraction of the Faraday rotation signal. The frequency is set high enough to provide a practically extractable signal from the lock-in amplifier and low enough to provide a usable magnetic field strength and avoid excessive heating of the magnet. In this set up 40 Hz was used with a magnetic field strength of about 1 kilogauss or 0.1 tesla.

The analyzer is set close to extinction with the polarizer for maximum sensitivity. The offset from extinction is the bias angle, $\theta_B$, nominally set at 10 degrees. The difference in polarization between the polarizer and the analyzer, $\phi$, is then,

$$\phi = \pi / 2 + \theta_B + \delta(t) \tag{17}$$

Where $\delta(t)$ is the Faraday rotation angle that is modulated at 40 Hz. According to Malus's law, the intensity of the beam incident on the detector is proportional to:

$$m^2(t) \cdot \mathrm{Cos}^2(\phi) = m^2(t) \cdot \mathrm{Sin}^2(\theta_B + \delta(t)) \tag{18}$$

Where m(t) is the on/off function of the chopper. Using the small angle approximation, the right side of Eq. (18) can be approximated as,

$$m(t) \cdot (\theta_B{}^2 + 2\theta_B.\delta(t) + \delta^2(t)) \tag{19}$$

The Faraday rotation signal extracted by the 40 Hz lock-in amplifier is proportional to

$$2[\tau_o / T] \cdot \theta_B \delta(t)_{rms} \tag{20}$$

Where $\tau_o$ is the duty cycle of the chopper, T the period, and rms denotes the root mean square voltage from the lock-in amplifier. This is the only 40 Hz component in Eq. (19). $\theta_B{}^2$ is a dc term and $\delta^2(t)$ is the square of a sinusoid and appears as a double frequency term i.e. at 80 Hz. The 100 Hz reference signal obtained with the magnet off ($\delta(t) = 0$) is,

$$m(t) \cdot \mathrm{Cos}^2(\theta_B) \tag{21}$$

The 100 Hz signal or normalization signal extracted by the lock-in amplifier is proportional to [321],

$$(\theta_B / \pi) \cdot (1 - \mathrm{Cos}^2(2\pi\tau_o / T))^{1/2} \tag{22}$$

which is the rms value obtained from the lock-in amplifier. This is the rms fundamental component of a square wave of amplitude $\theta_B^2$, period, T, and duty cycle, $\tau_o$. It can be derived by taking the rms magnitude (rms = peak value/$\sqrt{2}$ ) of the coefficients of the first sine and cosine terms in the trigonometric Fourier series formulation of a square wave of amplitude $\theta_B^2$, period, T, and duty cycle, $\tau_o$.

The Faraday rotation and normalization signals as extracted from their respective lock-in amplifiers contain the same unknown proportionality constants. Also, transmission differs from point to point on the samples due to crystal quality, and over time due to laser instability, including drift in intensity, mode hopping, and variations in beam pointing angle. A ratio of the rotation signal of equation (20) to the normalization signal in equation (22) would appear to solve both problems. The normalization signal in the denominator cancels the unknown proportionality constant in both signals and normalizes the rotation signal for transmission losses, especially those due to laser drift and erratic variations in laser intensity. The Faraday rotation can be calculated from equations (20) and (22) and the ratio of the two signals,

$$\delta_{rms} = \frac{(\theta_B / \pi)(1 - \mathrm{Cos}(2\pi\tau_o / T))}{2(\tau_o / T)} \times \frac{\text{Rotation signal}}{\text{Normalization signal}} \tag{23}$$

This works for normalization (magnet off) and Faraday rotation (magnet on) signals measured in quick succession, but long enough between measurements to allow the magnetic field strength to reach full strength once the magnet is turned on and settle to zero once the magnet is switched off. The two signals can be measured simultaneously and this is arguably the best configuration, but the 40 Hz rotation signal can interfere with the 100 Hz normalization signal. With the magnet on, the normalization signal is proportional to equation (19). The 100 Hz lock-in filters out the 40 Hz $2\theta_B\delta(t)$ term and the ac portion of the $\delta^2(t)$ term, but the square of a sinusoid contains a dc component, $\delta^2$. The dc component, $\delta^2$, couples with the other dc component, $\theta_B^2$, so that the fundamental normalization

component in equation (22) now becomes proportional to $(\theta_B^2 + \delta^2(t))$ instead of $\theta_B^2$. This can be made negligible by setting the bias angle large compared to the expected rotation.

The above procedures were used to map samples point by point to produce qualitative maps of relative rotation to measure uniformity and quality of samples [159(4*)], 197(5*), 201(3*)]. In practice, precise quantitative measurements required repeating several times and took longer. Modulation of the magnet caused heating over time and a loss of magnetic field strength and Faraday rotation signal. An alternate method was adopted to avoid this problem. Measurements were made by first establishing an intensity level for the normalization signal. Intensity is read out on the lock-in amplifier as an rms voltage. A voltage of 100 mV was used. The magnet was switched on in the dc mode (no modulation) for a few seconds. The sense of the rotation was chosen to increase intensity through the analyzer and add to the normalization signal. For a bias angle of 45 degrees, the intensity through the analyzer increases for negative rotation according to the analyzer function equation:

$$T = \mathrm{Cos}^2(\theta_r + \theta_B) / \mathrm{Cos}^2(\theta_B) \qquad (24)$$

Where T is transmission, $\theta_r$, is the rotation angle, and $\theta_B$, is the polarizer bias angle. Rotation for free electrons is positive when the beam propagates along the magnetic field lines [13] i.e. from north magnetic pole to south-pole. The rotation will be negative as desired if the beam enters the south pole of the magnet and exits the north-pole. This can be checked with a compass. The north-pointing needle of the compass points to the south-pole of the magnet. The total signal appearing on the lock-in is then the sum of two rms voltages, the normalization signal and the rotation signal. The normalization voltage of 100 mV is simply subtracted off to yield the rotation signal voltage. The magnet was then switched off and the initial normalization signal voltage of 100 mV was verified to be sure no drift or change in intensity had occurred during the measurement. The more elaborate rotation signal extraction and processing equations provided in the patent [318(9*)] and in equation (7) were not used due to the magnet heating problem and were found to be unnecessary for short single point measurements on the sample. The rotation signal voltage was converted to degrees of rotation using a calibration procedure. The bias angle on the polarizer was controlled with a stepping motor. A sample was placed in the beam and its normalization plus rotation signal measured in millivolts. The stepping motor was used to turn the bias angle on the analyzer to decrease the signal back to the normalization signal intensity level

of 100mV. The ratio of the rotation signal in millivolts to the number of steps required at 90 steps per degree gives the conversion factor in mV/degree.

The apparatus was tested by measuring the known effective mass in a nearly intrinsic sample of InSb. The sample was I1 referenced later in table VII. This sample was 1 mm thick and gave a strong Faraday rotation signal at 296 K.

## B. Measurement of Faraday rotation using an infrared spectrum

Figure 6 shows a schematic of the experimental set up and patent [322(8*)] for

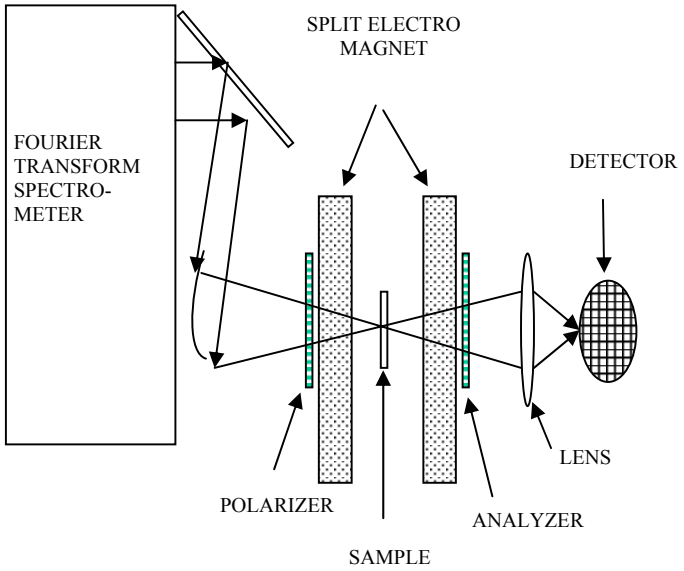


Fig. 6. Schematic of patent "Device and Method for Performing an Optical Hall Test" [322(8*)].

measuring an infrared Faraday rotation spectrum between approximately 5 and 17 microns. These are the limits of the mercury cadmium telluride detector, and the zinc selenide lenses, polarizers, and windows of the cryostat that contained the sample. The Fourier transform infrared spectrophotometer (FTIR) was a Mattson Research Series 2. The FTIR, in the figure, emits a beam that is redirected and focused by two mirrors onto the polarizer. The beam, now linearly polarized, passes through the north pole of an electromagnet, through the sample, and exits through the south pole of the magnet. It was found that choosing positive rotation, in this case, producing decreasing transmissions through the analyzer, produced more precise results. Finally, the beam passes through the analyzer, to a focusing zinc selenide lens onto the detector.

The magnet in this case was a larger 1.2 tesla magnet that is operated dc. The vacuum cryostat ( Cryo Industries, Atkinson, NH) containing the sample was specially designed with the sample mounted on a copper cold-finger enclosed by a 3/4 inch thick aluminum housing, with zinc selenide windows to allow the beam to pass through, that fit easily in the one inch gap of the magnet. It was mounted on a machining table (Palmgren Tools, Chicago, IL) that allowed fairly precise movement of the cryostat in and out, and up and down in the gap of the magnet to allow alignment with the beam and easy mounting and dismounting of the sample. Alignment of the cryostat and sample in the beam was accomplished by maximizing the transmission signal generated by the FTIR on the detector as shown on an oscilloscope connected to the detector. The detector was an external HgCdTe detector (Infrared Associates, Cranbury, NJ) that was powered with 12 V batteries to isolate them from electro-magnetic interferences from the other instrumentation. The cryostat and sample was cooled very simply by controlling the flow of liquid nitrogen through the cryostat. The cryostat was connected directly to a tank of liquid nitrogen using poly-vinyl-chloride tubing. Flow was accomplished by hand opening and closing the liquid valve on the tank to reach and maintain the desired temperature between 296 K and 77 K. Two thermocouples, equipped with separate readouts, set 1 1/2 inches apart, were mounted at the top of the cold-finger and near the sample. The temperature is taken to be stable when the two thermocouple readouts on a precision Lakeshore dual temperature readout matched within a few tenths of a degree. The measurements took a minimum of 3 minutes limited by the length of the FTIR scan. It takes a little practice, but temperatures can be maintained within ± 0.5 degrees K using this technique for as long as required.

The detector, attached to and controlled by the FTIR, produces a signal that is proportional to light intensity passing through the analyzer, and transmits this signal to the computer. Using the signal from light passing through the analyzer with the magnetic field off as a reference, the computer produces a transmission signal, T, which is the ratio of the intensity signal produced with the magnet on to the intensity of the signal produced with the magnet off. The FTIR produces beams at approximately 1500 equally spaced wavelengths between 5 and 20 microns. The values for transmission, T, at each wavelength are converted by the computer point by point to Faraday rotation using the formula:

$$\theta_r = \frac{\mathrm{ArcCos}[\sqrt{T}\mathrm{Cos}(\theta_B)] - \theta_B}{B} \qquad (25)$$

where B is the magnetic field strength in tesla and $\theta_r$ here is rotation/unit magnetic field. The converted points are plotted as total rotation verses wavelength squared, $\lambda^2$. Essentially, the device is a magnet, polarizer and analyzer, added to an FTIR used to produce a high resolution Faraday rotation spectrum.

Again, the apparatus was tested using InSb sample, I1 (referenced later in table VII), as in the $CO_2$ laser apparatus in the previous section. This sample was 1 mm thick and gave a strong Faraday rotation signal at 296 K.

Infrared absorption was measured using the normal mode of the FTIR. These measurements were used in Eq. (11) to determine the proportionality, "C", between electron mobility and the ratio of Faraday rotation to absorption.

## C. Multiple Pass Faraday Rotation Amplifier

Modern HgCdTe detectors use thin films on CdZnTe substrates. Faraday rotation is linearly dependent on thickness so thin films often yield little or no signal. Magnets currently available, even super-conducting magnets, cannot make up for the lack of signal in micron and even nanometer thick films. The following is a description of a proposed device (patent application submitted [323]) for measuring Faraday rotation in thin films and in samples with relatively low absorption and large Verdet constant. The Verdet constant is given by, $\theta = VBL$, where $\theta$, is the Faraday rotation and V is the Verdet constant of the material. The device is shown schematically in figures 7 and 8. The purpose of this device is to amplify Faraday rotation (FR) by many multiple passes through a sample using multiple internal reflection and successive mirrored chambers where the rays are repeatedly sent back through the sample. Normally, multiple internal reflection is an interfering effect that is avoided whenever possible in traditional FR measurements. Here it is used to maximum effect where it is maximally occurring, in a thin, low absorbing, film, to multiply (amplify in effect) the FR signal.

Referring to figures 7 and 8, the sample chamber, consisting of an input and an output mirror with the sample in between, is located between the poles of an electro-magnet and is illuminated by an intense light source. Light is allowed to traverse the chamber multiple times undergoing cumulative Faraday rotation (FR) with each pass back and forth through the sample. The FR is further enhanced by multiple internal reflection inside the sample.

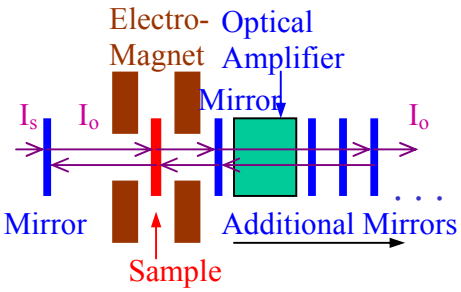


Fig. 7. Multiple Pass Faraday Rotation Amplifier.

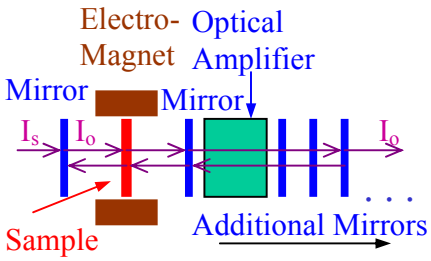


Fig. 8. Multiple Pass Rotation Amplifier, Voigt configuration.

The transparency of the input mirror is adjusted to be very low to allow sufficient light in from the intense source, but at the same time, allow virtually none of the Faraday rotated sample chamber light to escape. The sample chamber output mirror (input to the optical amplifier) is adjusted to allow a maximum number of passes through the sample, in accordance with the absorption of the sample for the light frequency used, before it is transmitted to the next chamber, the optical amplifier (OA) chamber. A maximum number of passes through the sample is implemented to mitigate as much as possible any polarization insensitivity of the optical amplifier. That is, in order to build up the rotation signal as much as possible before feeding the beam to the optical amplifier, which may have limited ability to preserve polarization. The beam passes through the sample chamber output mirror into the OA where it makes multiple passes. The purpose of the OA is to compensate for system losses, i.e. absorption of the sample, transmission losses in the mirrors, and any escape of light from the sample chamber. The gain of the OA should be adjusted to maintain operational intensity while preventing over production of light energy in the device. Amplification is adjusted via the optical gain of the chamber and transparency of the OA chamber mirrors. Amplified light is then sent back for another round of passes through the sample to accumulate further Faraday rotation. Successive chambers beyond the OA send light back through the OA and sample chambers to repeat the process and further multiply the FR of the signal. The ultimate FR amplification is determined by the number and transparency of the successive mirrored chambers.

## D. Hall Tests

Carrier concentration and mobility measurements were required as references for all the samples. The Hall test invented in 1879 [324] and improved by Van Der Pauw in 1958

[325] is commonly used to measure carrier concentration and mobility in semiconductors. It usually requires four electrical contacts to be soldered to the surface of each corner of a chemically cleaned square cut from the material. The test is time consuming and subject to significant error due to contamination from the soldered contacts. Depending on skill level, this can take 30 minutes to an hour. It is especially critical in high mobility materials like InSb and HgCdTe to use a very pure indium solder, because indium and its impurities diffuse quickly into the sample at its melting temperature. These impurities effectively "dope" the sample adding electrically active carriers and decreasing mobility. Manufacturers of these materials use personnel highly skilled in fabricating delicate contacts quickly to the material. This is even more critical in thin films. In n-type silicon wafers soldering with 99.9999% pure indium solder typically results in a 10% increase in carrier concentration and a consequent 10% reduction in mobility [199(1*), 200(2*), 201(3*)]. In high mobility HgCdTe and InSb samples, soldering can result in a much larger increase in carriers and decrease in mobility, severely corrupting the results. It is important to note, that to determine the effective mass in HgCdTe, it was essential to develop a consistent dependable method of fabricating non-contaminating contacts to get accurate values of carrier concentration and mobility. Heated contacts were too unreliable and too risky to use on very hard to get samples. Figures 9 and 10 show mobility and carrier concentration plots for an Sb doped n-type germanium sample, oriented <100>, using normal indium soldered contacts and a cold indium contact technique described in the next paragraph. Figure 9 shows more than a 10% decrease and shift in mobility versus temperature and figure 10 shows a 10-23% increase in carriers depending on temperature. The peak mobility of 2400 $cm^2$/V-s is typical for n-Ge doped in this range [326].

To avoid contamination, a method of burnishing indium onto the sample to construct contacts without heat was developed [199(1*), 200(2*), 201(3*)]. Indium is a very soft and malleable metal. It can be easily cut into small pieces with a sharp knife and rolled or spread onto the surface of the four corners of a square semiconductor sample. Using a dental pick and a small piece of indium about the size of the point on the pick, the indium is flattened out and gently scraped onto the surface with the side of the point of the pick. It takes practice to avoid excessively scratching or breaking very delicate HgCdTe or InSb samples. The contacts were kept as small as possible to avoid anomalous effects due to large area contacts. Contacts generally ranged between 1-2 mm in diameter on the corners of square samples that ranged from 7 mm to 11 mm on a side. Sample thicknesses ranged

from 0.3 mm to 1 mm. Once the corner is entirely coated with a thin layer of indium, larger pieces can be rolled onto the corners to build up the thickness. A small loop is made in the

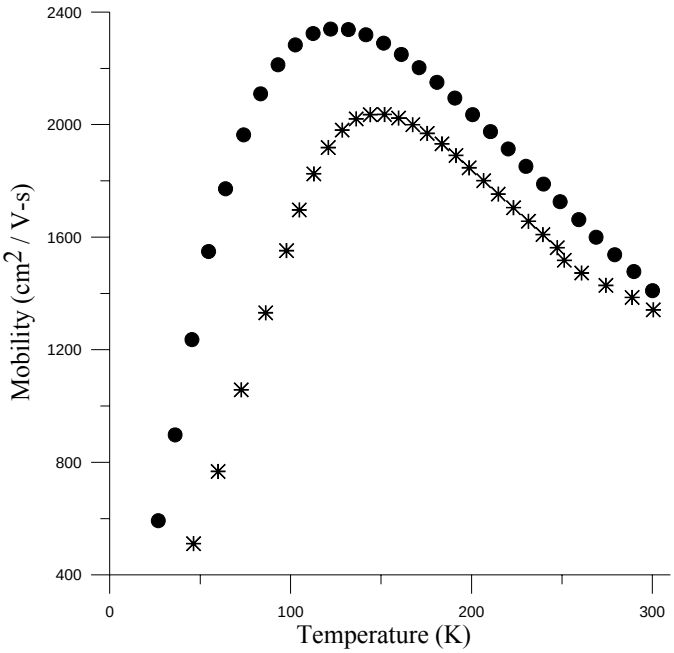


Fig. 9. Mobility versus temperature in n-type germanium, $N_H = 26.94 \times 10^{16}$ cm$^{-3}$ at 296 K. The upper plot was obtained using indium cold contacts. The lower plot was obtained using normal indium soldered contacts.

end of a thin wire (0.25 mm in diameter) and dipped into a small dish of molten indium. Once cooled, the droplet of indium coating the loop is laid onto the built up corner and rolled into the indium. This makes a very good ohmic contact, which is stable down to 10 K for n-type HgCdTe, InSb, Si, and Ge.

The technique of fabricating these "cold contacts" was developed by Charles Sisk of the NASA Space Sciences Laboratory (SSL), Marshall Space Flight Center from an idea of another researcher at the SSL. The contacts were physically strong for the most part, but some samples required testing many times and contacts sometimes broke off at the corners, wires were pulled out in the course of testing, or contacts sometimes flaked off. The contacts were replaced with no noticeable difference in carrier concentration or mobility measurements, indicating that no contamination occurred with these cold contacts. In n-type

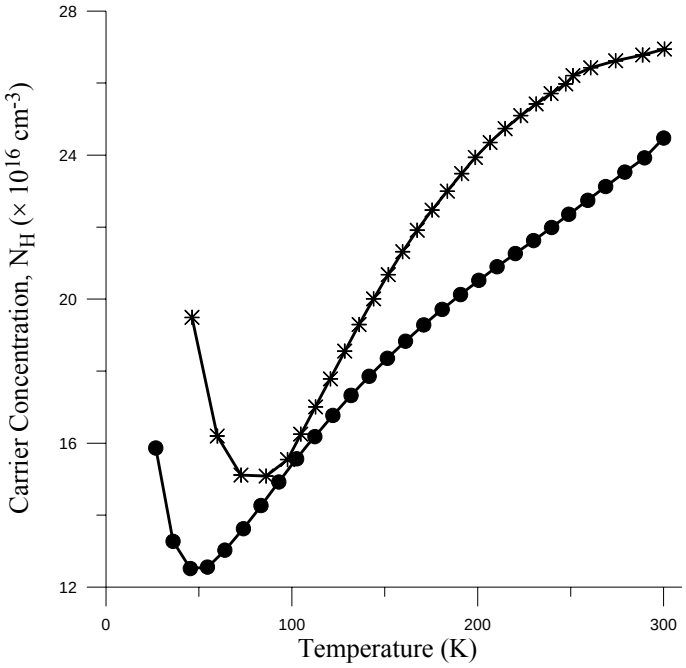


Fig. 10. Carrier Concentration versus temperature in n-type germanium, $N_H = 24.5 \times 10^{16}$ cm$^{-3}$ at 296 K. The lower plot was obtained using indium cold contacts. The upper plot was obtained using normal indium soldered contacts.

GaAs, however, these contacts were only good down to about 230 K at best. These tests were repeated several times but Hall measurements became erratic and unusable below 230 K. Figures 11 and 12 show mobility and carrier concentration in three GaAs samples using the manufacturer's Hall test samples with the contacts and wires intact. The contacts were scorched on, probably due to the difficulty in establishing an ohmic contact on n-type GaAs at lower temperatures. The manufacturer provided Hall data at room temperature and at 77 K in general agreement with the results of figures 11 and 12. The scorched on contacts tended to provide erratic results as can be seen in the mobility results for sample G29 in figure 11. One thing they do show is carrier concentration and mobility change little with temperature in n-GaAs. The plots in figures 11 and 12 show variation in mobility with temperature of about 5-10% and variation in carrier concentration of less than 2%. Figures 13 and 14 show Hall results for two samples of G20 ($N = 142 \times 10^{16}$ cm$^{-3}$) using cold

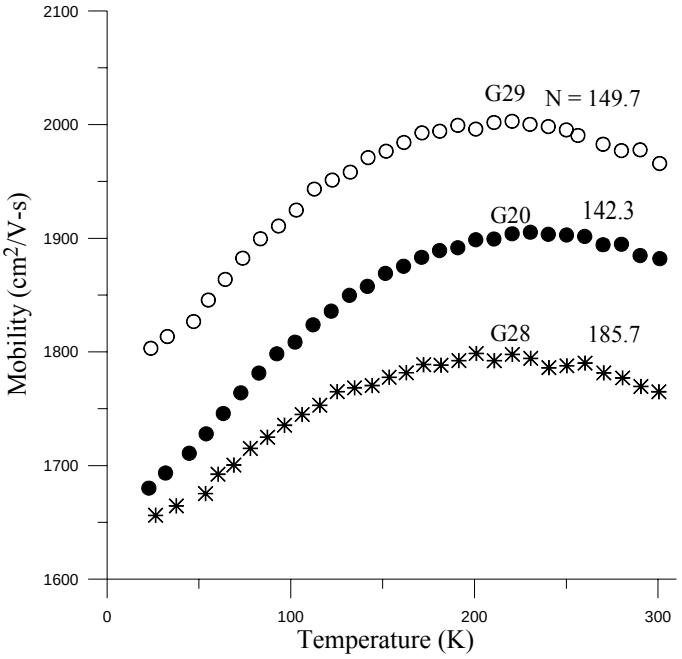


Fig. 11. Mobility versus temperature in n-type GaAs. Sample numbers and concentrations, $N_H \times 10^{16}$ cm$^{-3}$, at 296 K are labeled in the figure.

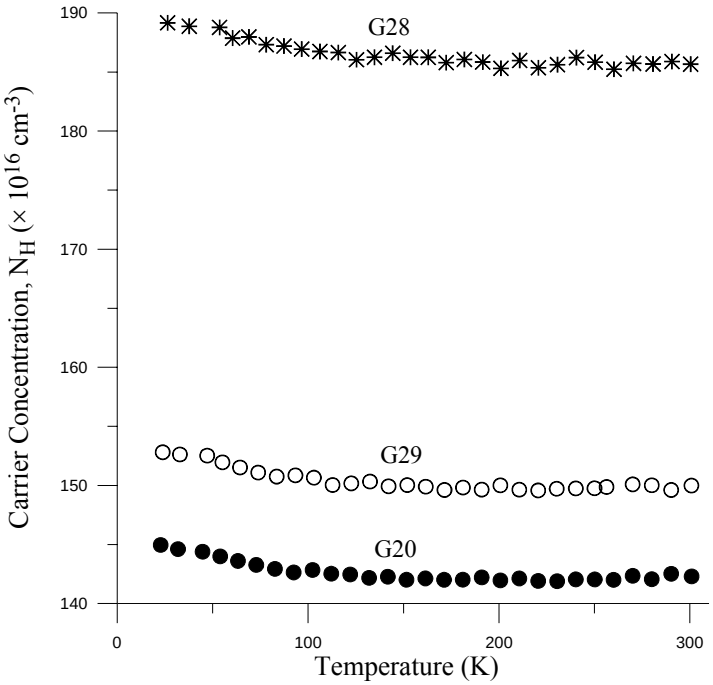


Fig. 12. Carrier concentration in n-type GaAs samples. Sample numbers are labeled in the figure.

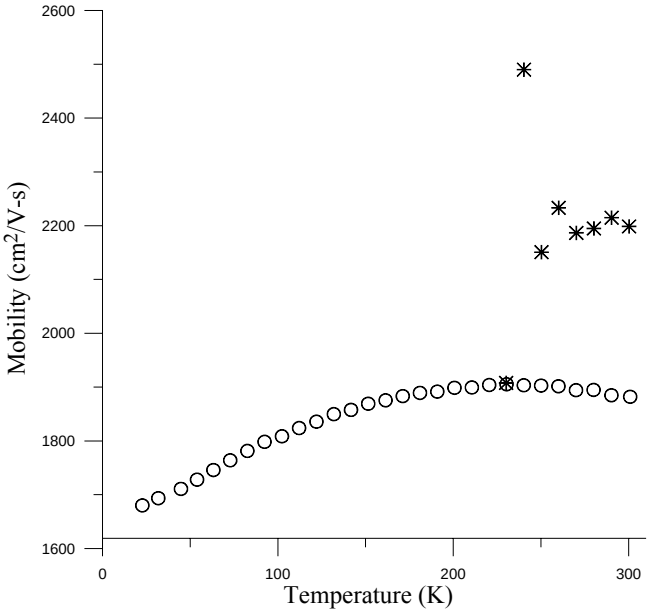


Fig. 13. Mobility versus temperature in GaAs sample, G20. The lower plot shows results obtained using normal indium soldered contacts. The upper plot shows results using indium cold contacts. The last two points on the left at 240 K and 230 K gave "inhomogeneous sample" warnings. The run was ended at 230 K.

contacts on a fresh sample and the manufacturer's sample. The plots show an increase of about 11% in carriers and about a 14% decrease in mobility comparing cold contacts to the soldered contacts, but the cold contacts are suspect since they are unstable in this case below 250 K. They do tend to verify concentration and mobility are fairly constant with temperature in n-GaAs and that this is not due to a contamination effect. This property was used to measure temperature dependant effective masses in n-GaAs using room temperature carrier concentration results.

The Hall test apparatus shown schematically in figure 15 was set up using a Keithly high precision nano-volt digital voltmeter and current source. The sample current was kept constant in all samples at 50 mA. Sample resistivities generally ranged between 0.11 Ω/cm (n-Si at 296 K) to 0.001 Ω/cm (n-HgCdTe, x = 0.199 at 20 K) giving maximum voltages between 8 mV and 70 μV across the diagonal of a 1 cm wide sample. This is well below the maximum, 1V, recommended by the American Society for Testing Materials (ASTM) standard for Hall measurement of carrier concentration, resistivity, and mobility in samples in the van der Pauw configuration (square with contacts on the corners. See figure 16.) [327]. The magnet was a DC electro-magnet set at 5 kilogauss that was driven by a precision Keithly current source. The drive current was reversed to reverse the polarity of

the magnet. Residual flux with the current off was negligible. Temperature was maintained within 0.1-0.3 K with a liquid helium cooled cryostat. The wires from the sample contacts were soldered to electrical contact posts on the cold finger of the cryostat. The sample itself

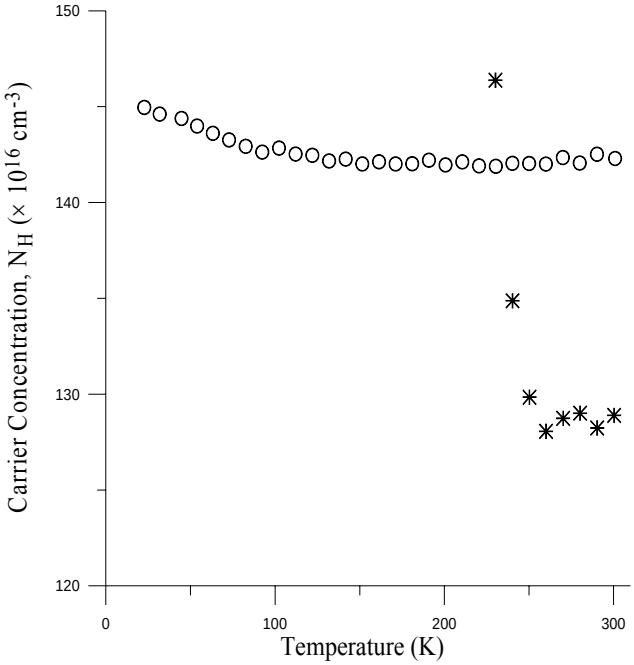


Fig. 14. Carrier concentration versus temperature in GaAs sample, G20. The upper plot shows results obtained using the manufacturers lead soldered contacts. The lower plot shows results using indium cold contacts. The last two points on the left at 240 K and 230 K gave "inhomogeneous sample" warnings. The run was ended at 230 K.

was fixed to the cold finger using a thermal grease to maintain good thermal contact. The contact posts of the cold finger were connected to the Keithly digital voltmeter and current source mentioned above. Resistivity measurements were made with the magnet off, by measuring the voltage induced between the contacts on each side of the square sample, while sample current was passed through the contacts on the opposite side, first in one direction, then with the current reversed. The Hall coefficient, $R_H$, was measured by measuring the Hall voltage induced between the contacts of one diagonal with the magnet on, while sample current was passed in one direction then reversed through the other diagonal. Effectively, the Hall voltages of eight possible configurations were averaged together to calculate $R_H$. All instrumentation, including the magnet current source and temperature controller to the cryostat, was computer controlled through the Keithly

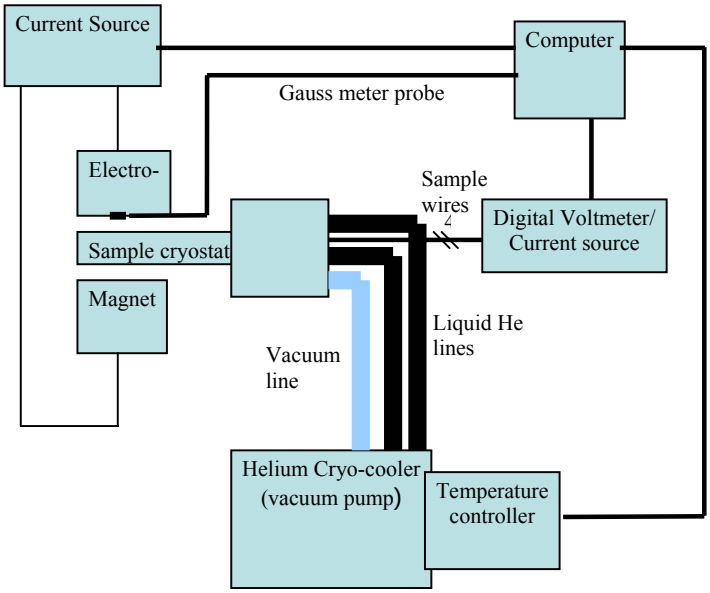


Fig. 15. Hall test apparatus. The system was computer controlled to establish temperature at 10 K intervals, operate/measure the electro-magnet, switch sample current and induced voltage measurements between sample contacts, and record results.

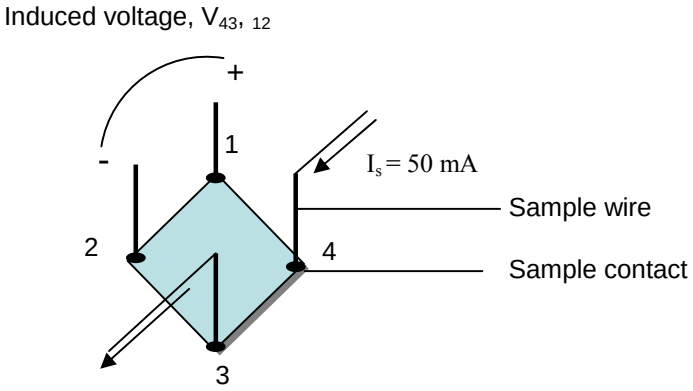


Fig. 16. Square sample wired in the van der Pauw configuration. Resistivity is measured using a 50 mA sample current, $I_s$, passed through the wires on one side of the square and measuring the voltage induced on the other side. Eight configurations are averaged in the ASTM standard. $V_{43,\ 12}$ is the voltage between terminals 1 and 2 with sample current flowing between 4 and 3 with the current direction and polarity shown.

instrumentation. Switching needed to measure voltages and pass sample current between different contacts was accomplished under computer control internally to the Keithly digital voltmeter and current source. Inconsistencies between sets of Hall voltages or resistivity

voltages of over ± 10%, were taken to indicate an inhomogeneous sample according to the ASTM standard. If this occurred, the computer was programmed to issue an "inhomogeneous sample" warning message. If a warning was issued, the apparatus, especially the sample and soldered contacts, were carefully checked and/or renewed. If the message continued, the sample was discarded.

The standard recommended a default Hall factor, r = 1, where r is the proportionality between the Hall coefficient and carrier concentration, $R_H = r/Ne$, for most semiconductors, and $r = 3\pi/8$ specifically for silicon, based on the dominant impurity scattering in n-Si. This was followed for InSb, HgCdTe, and GaAs. A Hall factor of $3\pi/8$ was used for Ge because of its close similarity to Si. Beyond mounting the sample, initializing the computer, and starting the apparatus, the system was completely automated to cool the sample and take measurements about every 10 degrees down to 20 K maintaining temperature at each step within ± 0.1 degree C. After construction, the apparatus was extensively tested and the results carefully compared to known manufacturer's data of several samples: HgCdTe from Loral (now BAE Systems), Texas Instruments, and Johnson-Matthey (formerly Cominco); InSb from Johnson-Matthey; n-GaAs from AKZO-Crystal Specialties International and Sumitomo; and n-Si from Silicon Quest International.

## E. Samples

### HgCdTe

Table III shows sample data on six HgCdTe samples from three sources, Loral (BAE Systems), Johnson Matthey (formerly Cominco), and Texas Instruments. The x values were determined using transmission spectra by the manufactures, who claim accuracy to ± 2%. Two simple methods have been in general use for many years [328]. The first is described in Micklethwaite [329]; a tangent is drawn along the straight line cut-on transmission rise at the fundamental absorption edge at the point where the transmission is 1/e (natural log e = 2.718) times the maximum transmission of the sample. The intersection of this line with the zero transmission axis is the cut-on wavelength, $\lambda_{co}$. The band-gap, Eg, in eV is calculated from $\lambda_{co}$ in wave numbers, $cm^{-1}$, using $Eg = \lambda_{co} \times 1.24 \times 10^{-4}$. The bandgap is then used to determine x using the empirical formula in [330-331], where Higgins et al. [331] compiles and standardizes a number of the more successful empirical

**Table III. HgCdTe Sample Data.**

| Sample # | x | T (K) | $N_H$† ($\times 10^{16}$ cm$^{-3}$) | $N_H$* ($\times 10^{16}$ cm$^{-3}$) | $\mu_H$† ($\times$ 1000 cm$^2$/V-s) | $\mu_H$* ($\times$ 1000 cm$^2$/V-s) | % Difference | |
|---|---|---|---|---|---|---|---|---|
| | | | | | | | $N_H$ | $\mu_H$ |
| M010 (n-type) | 0.199 | 77K<br>296K | 1.19 | 1.20<br>4.86 | 164 | 154<br>12.1 | -0.6 | +6.8 |
| M160 | 0.202 | 77K<br>296K | 0.16<br>3.10 | 0.168<br>3.16 | 193<br>12 | 168<br>11.9 | -3<br>-1.9 | +14.9<br>0 |
| M61 (n-type) | 0.217 | 77K<br>296K | 1.11 | 1.12<br>3.60 | 109 | 98<br>10.5 | -0.7 | +11.6 |
| M26 | 0.248 | 77K<br>296K | 0.12<br>1.81 | 0.136<br>1.91 | 71<br>7.9 | 79<br>7.7 | -11.8<br>-5.2 | -10.3<br>+3.0 |
| M18 | 0.28 | 77K<br>296K | 0.0015<br>0.40 | 0.533 | 59.8<br>65.7 | | -25.0 | |
| M20 | 0.30 | 77K<br>296K | 0.0069<br>0.28 | 0.0069<br>0.332 | 46.2<br>42.7 | 46.2<br>43.7 | 0<br>-15.6 | 0<br>-2.3 |

* Hall tests using "cold" indium contact technique [199(1*), 200(2*), 201(3*)]. † Data provided by the manufacturer.

formulations for HgCdTe properties. The second, in standard use at Loral (now BAE Systems), a major manufacturer of HgCdTe bulk material and detectors, probably gives results more consistent with the standard empirical formulas. The cut-on wavelength is given as the 1% transmission point along the transmission rise, usually occurring in the "tail" of the fundamental absorption edge [328, 332]. The table shows the manufacturer's Hall tests and Hall tests performed using the technique of the last section using "cold" indium contacts. The manufacturers of these high mobility materials employ skilled personnel to perform Hall tests using very pure solder and delicate contacts to the very edges of the sample. In the case of M010, M160, M61 and M26, careful Hall tests were performed on the actual samples. Samples M18 and M20 were estimated from tests conducted from other wafers close by in the boule. This could explain their higher variability compared to the other samples. The table shows the manufacturers' Hall tests are generally within ± 15% in both carrier concentration and mobility of the cold contact technique. Many other HgCdTe samples not listed in table III were tested and used in various figures that follow. The variability of Hall test results of table III are fairly typical of these samples as well. All the samples in table III except M26 were made by a melt-grown bulk material method that results in wafers cut from the boule that are Hg deficient and, therefore, initially p-type [328, 332]. These wafers are annealed in ampoules in Hg vapor for weeks to allow Hg to soak into the surfaces of the wafer. This process results in wafers with an n-p-n structure, where the surfaces to some thickness are slightly n-type and a small thickness p-type core still remains. This type of bulk wafer is very common. Detectors are normally made on the n-type surfaces [332] with no consequence from the p-type core or the n-p-n structure since photo conduction occurs parallel to the n-p-n layers. Hall test anomalies of wafers of this

configuration were analyzed by Basson et al. in [333]. Basson presents a model and analysis showing anomalies in Hall mobilities and Hall coefficients, $R_H$, that occur in these samples between 20 K and 300 K. The three regions, each of the n-p-n layers, are modeled as three parallel resistors. The two outside n-layers are further combined into a single resistor to give two parallel resistors, one p-type and one n-type. For samples that have relatively thin n-type layers, the model shows a significant collapse of the mobility and the Hall coefficient between 20 K and 300 K relative to a solid n-type bulk sample. That is, the solid sample shows a smooth well behaved curve, and the thin, low conductivity n-layered samples show significant dips in mobility and Hall coefficient between 20 K and 300 K. The thinner the outside layers and/or the thicker the p-type core, the deeper the collapse in mobility and $R_H$. At 200 K-300 K the n-p-n curves merge into the solid bulk sample curve and appear to follow the solid n-type bulk sample curve through to higher temperatures. Hall tests on five of the samples in table III using the cold contact technique are shown in figures 17, 18, and 19 for mobility, carrier concentration and Hall coefficient, $R_H$, respectively, where $N = 1/eR_H$, and e is the electron charge. The mobility and $R_H$ curves follow the profile of an n-type bulk sample in the model. No anomalies are apparent in the figures. The curves for mobility, Hall coefficient, and carrier concentration are smooth and well behaved over the full range of the curve from below 77 K to 296 K. The electrical parameters of the p-type cores of these samples are largely unknown or unpublished, but these curves indicate the conductivity of the n-layers dominates the resistivity of the p-type cores so that their effect is negligible on the sample's electrical properties.

Mobilities of these samples shown in figure 17 generally compare well with empirical mobilities reported in Scott [270] Lou et al. [334] and Reine et al. [332]. The x = 0.199 (n-type) sample mobility is a bit low at 77 K at $1.6 \times 10^5$ $cm^2/V\text{-}s$ compared to $3.3\times 10^5$ $cm^2/V\text{-}s$ reported by Lou, $2\times 10^5$ $cm^2/V\text{-}s$ reported by Scott, and 3-5 $\times 10^5$ $cm^2/V\text{-}s$ reported by Reine. This could be due to the $N = 1.2 \times 10^{16}$ $cm^{-3}$ residual carrier concentration and possibly some normal variability in the tests. M26, x = 0.248 was made using the solid state recrystallization (SSR) method described in [335]. The mobility of this sample is also shown in the figure. It compares well with empirical data presented by Reine [332] for SSR

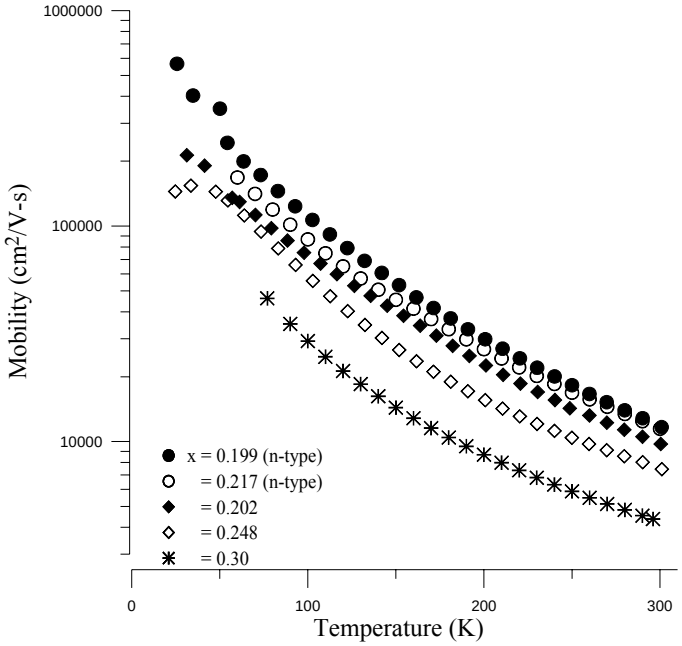


Fig. 17. Mobility versus temperature for $Hg_{1-x}Cd_xTe$ samples in Table III. Cadmium mole fraction, x, for each sample is labeled in the figure.

wafers. This sample was a solid n-type bulk sample with no p-type core. Figure 18 shows carrier concentrations for the samples in table III. The solid lines are empirically calculated carrier concentrations using standard formulas for intrinsic carrier concentration vs. x found in [331, 336]. The residual carrier concentrations measured at 70 K in these samples were added to the empirical formula in the n-type samples labeled in the figure. The empirical formulas (plus residual concentration) match the measured concentrations very well, except for M26 (x = 0.248). Transmission spectra between 301 K and 77 K using the 1% transmission point, give x for this sample as 0.241 to 0.252. This could explain some of the extra carriers but not all. The excess carriers begin to appear at about 77 K up through room temperature in this sample. The growth methods used to grow these wafers, both the bulk and the n-p-n samples, yield variable and mixed crystal orientations and, as a result, the crystal orientations of all these samples are unknown.

Figure 20 shows a plot of Hall coefficient vs. magnetic field, B, for four of the samples in table III. This type of sample characterization is explained by Reine in [332]. The tests in figure 20 were actually performed by Reine's group at Loral. For a consistent sample of a single carrier type the Hall coefficient should be independent of magnetic field. This

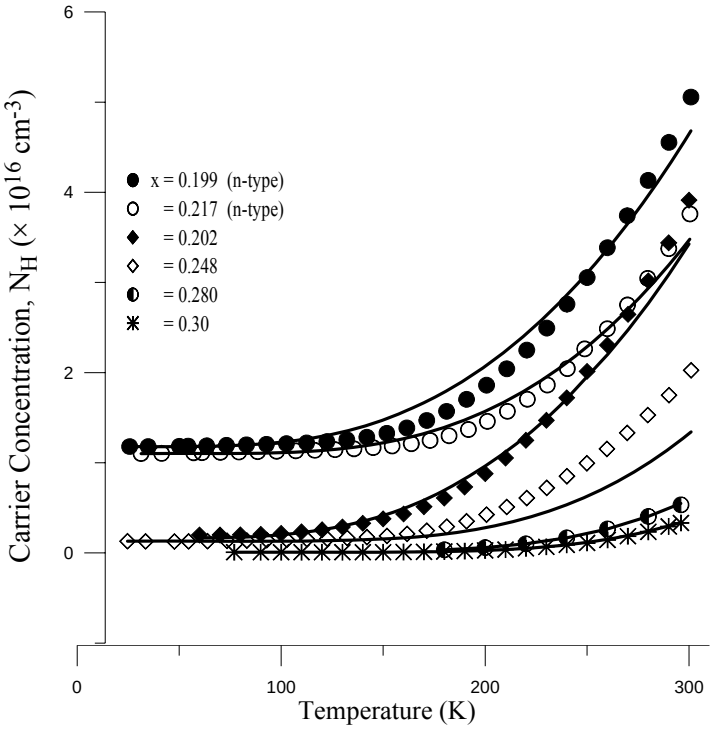


Fig. 18. Carrier concentration versus Temperature in $Hg_{1-x}Cd_xTe$. The cadmium mole fraction, x, is labeled for each sample in the figure. Symbols are Hall test data. The solid lines are empirical calculations of Hansen and Schmit.

appears to be case for three of the samples, M160, M61, and M010. The M26 sample, which gave anomalous results in figure 18, appears to have at least two carrier types.

According to Reine, the relationship between the field dependence of the curve at lower fields in figure 20 and the sample's carrier concentrations is not a simple one. Presumably, other factors are involved, but it does possibly indicate the presence of another carrier.

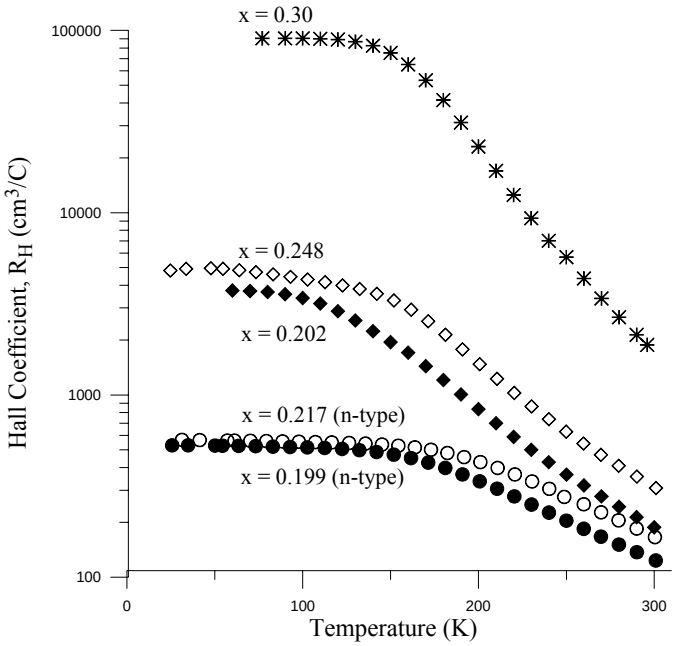


Fig. 19. Hall coefficient versus temperature in $Hg_{1-x}Cd_xTe$. Symbols are Hall test data. The curves appear normal for n-type HgCdTe with no apparent anomolies due to the n-p-n structures of the x = 0.199, 0.202, 0.217, and 0.30 samples. The x = 0.248 sample has no p-type core.

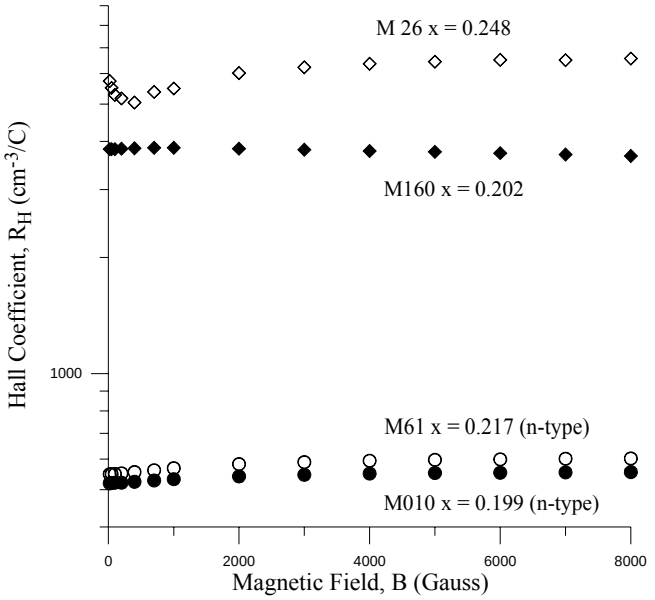


Fig. 20. Hall coefficient vs. magnetic field for four samples in Table III at 77 K. The plots for M160, M61, and M010 are relatively flat, indicating a consistent sample with a single dominate (n-type) carrier. The dip in the low field portion of the M26 plot indicates the possible presence another carrier with higher mobility.

**InSb**

Table IV gives manufacturer's Hall test data compared to cold contact Hall data for nine n-type Te doped InSb samples (oriented <111>). The average variability in carrier concentration is ± 10.8 % and in mobility is ± 20.54 %. The extreme differences are -19.9% to + 56.8%. The ranges given in the manufacturer's data suggest these are results performed on samples of the same lot rather than on the samples themselves. This could explain the high variability. Full Hall test results for the nine samples in table IV are shown in figures 21 and 22. Cold contact mobilities for the nine samples in table IV are equal to the mobilities in [336-337] at 77 K and 296 K where n-type InSb mobility vs. N data is compiled from several sources.

**Table IV. InSb Sample Data.**

| Sample # | T (K) | $N_H$† ($\times 10^{16}$ cm$^{-3}$) | $N_H$* ($\times 10^{16}$ cm$^{-3}$) | $\mu_H$† ($\times$ 1000 cm$^2$/V-s) | $\mu_H$* ($\times$ 1000 cm$^2$/V-s) | % Difference | |
|---|---|---|---|---|---|---|---|
| | | | | | | $N_H$ | $\mu_H$ |
| I 1 | 77K<br>296K | 0.036<br>1.95 | 0.039<br>2.11 | 512<br>69 | 475<br>63.4 | -7.0<br>-7.6 | + 7.9<br>+8.8 |
| I 3 | 77K<br>296K | 2.2-2.3<br>3.06 | 2.55<br>3.76 | 100-110<br>78 | 89.62<br>54.81 | -11.8<br>-18.9 | +17.2<br>+42.3 |
| I 6 | 77K<br>296K | 10-15 | 10.81<br>11.93 | 52-53<br>45-52 | 57.8<br>41.99 | +15.6<br>+4.8 | -9.2<br>+11.9 |
| I 8 | 77K<br>296K | 21.6-23.6 | 21.9<br>22.94 | 51-52<br>41 | 44.84<br>35.07 | +3.2<br>-1.5 | +14.9<br>+16.9 |
| I 9 | 77K<br>296K | 25.6-27.6 | 23.67<br>25.74 | 48-49<br>44 | 41.75<br>31.63 | +12.4<br>+3.3 | +16.2<br>+39.1 |
| I 10 | 77K<br>296K | 31.6-36.6 | 32.59<br>34.31 | 44-46<br>42 | 38.43<br>30.07 | +4.6<br>-0.6 | +17.1<br>+39.7 |
| I 11 | 77K<br>296K | 47.6-50.6 | 48.34<br>49.28 | 35-37<br>42 | 33.20<br>26.91 | +1.6<br>-0.4 | +8.4<br>+56.8 |
| I 12 | 77K<br>296K | 62.6-86.6 | 69.45<br>74.43 | 27-32<br>27 | 27.90<br>21.98 | +7.4<br>+0.2 | -5.7<br>+22.8 |
| I 14 | 77K<br>296K | 110-190 | 100.25<br>105.13-108.64 | 18-25<br>17 | 24.96<br>20.24 | +49.6<br>+42.7 | -13.9<br>-16.0 |

* Hall tests using "cold" indium contact technique [199(1*), 200(2*), 201(3*)]. † Data provided by the manufacturer.

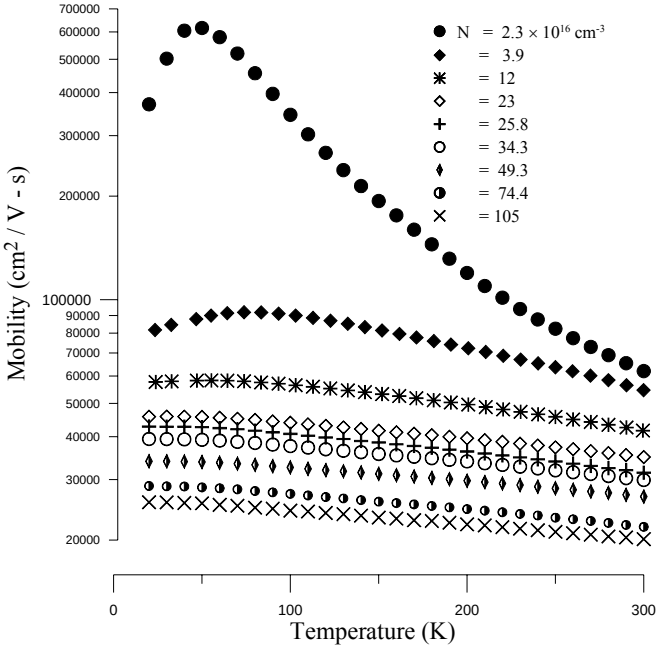


Fig. 21. Mobility versus temperature in nine n-type InSb samples contained in Table IV. Carrier concentrations, $N_H \times 10^{16}$ cm$^{-3}$, at 296 K are labeled in the figure.

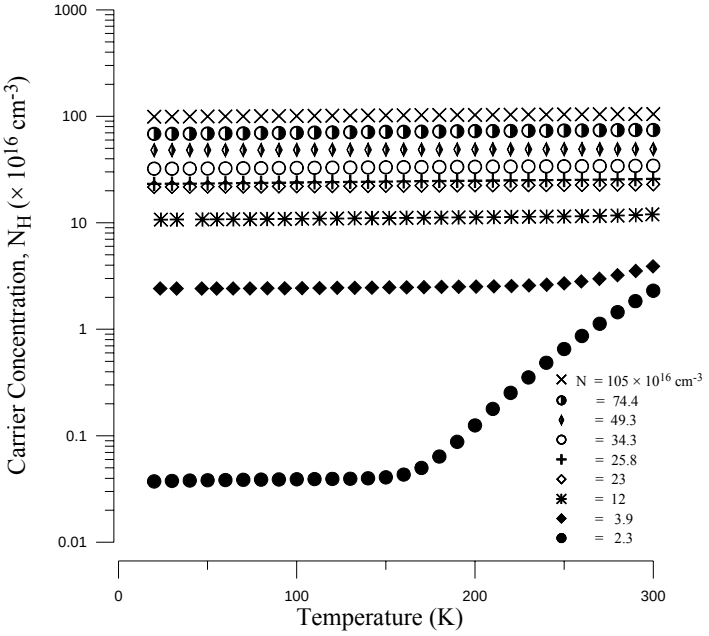


Fig. 22. Carrier concentration $N_H \times 10^{16}$ cm$^{-3}$ versus temperature in the n-type InSb samples of Table IV.

**GaAs:**

**Table V. n -GaAs Sample Data at 296 K.**

| Sample # | $N_H$† ($\times 10^{17}$ cm$^{-3}$) | $\mu_H$† ($\times$ 1000 cm$^2$/V-s) |
|---|---|---|
| G4 | 2.9-3.2 | 3.5-3.6 |
| G14 | 5.73 | 2.5-2.6 |
| G25* | 8.62 | 2.358 |
| G20* | 13.37 | 2.050 |
| G21* | 20.3 | 1.700 |

† Data provided by the manufacturer.
*Retested by the manufacturer.

The mobility values in table V are lower than mobilities for n-GaAs for these carrier concentrations reported in Sze et al. [98]. The lowest concentration sample, G4, is lower by at least 10% increasing to over 30% for the highest concentration sample, G21. The variability seen in G20 between the initial test and the retest, i.e. between figures 13 and 14 and table V is 6% in $N_H$ and 8 % in mobility but the variability is probably at least 10%. This is hinted at in figure 11 where the mobility of G29, $N_H$ = 149.7, appears with 5% higher mobility than the lower concentration sample, G20. All samples were Si doped with a <100> orientation.

**Si**

The silicon samples were n-type, phosphorous doped, with <100> orientation. Hall test data is summarized in table VI. Hall test results showing mobility and carrier concentration for six n-type silicon samples are shown in figures 23 and 24. Figure 25 shows a reference curve for silicon mobility versus concentration taken from reference [338]. The reference curve was calculated using

$$\mu_{ref} = \mu_{min} + \frac{\mu_{max} - \mu_{min}}{1 + \left(\frac{N}{N_{ref}}\right)^{0.711}} \tag{26}$$

Where $\mu_{ref}$ is in cm$^2$/V-s, and the parameters from [338] for phosphorous doped samples are, $\mu_{min}$ = 68.5, $\mu_{max}$ = 1414, and $N_{ref}$ = 9.2 x $10^{16}$ cm$^{-3}$. The reference curve is a fit to data (300 K) published by the National Bureau of Standards (NBS) in 1980 referenced in [338]. The

**Table VI. Silicon Sample Data at 296 K.**

| Sample # | $N_H$† ($\times 10^{16}$ cm$^{-3}$) | $N_H$* ($\times 10^{16}$ cm$^{-3}$) | $\mu_H$†† (cm$^2$/V-s) | $\mu_H$* (cm$^2$/V-s) | % Difference | |
|---|---|---|---|---|---|---|
| | | | | | $N_H$ | $\mu_H$ |
| S 1A | 8 | 8.26 | 727 | 799 | - 3.1 | - 9.1 |
| S 5 | 8.5 | 8.44 | 730 | 791 | + 0.7 | - 7.6 |
| S 7 | 9 | 9.18 | 714 | 745 | - 2.0 | - 4.2 |
| S 8 | 11 | 12.00 | 661 | 694 | - 8.1 | - 4.8 |
| S 13 | 13 | 13.54 | 619 | 677 | - 4.0 | - 8.6 |
| S 14 | 40 | 34.98 | 411 | 513 | +14.4 | -20.0 |
| S 16 | 40 | 37.19 | 413 | 499 | + 7.6 | -17.3 |
| S 24 | 45 | 40.58 | 395 | 482 | +10.9 | -18.0 |
| S 25A | 45 | 40.78 | 402 | 505 | +10.4 | -20.4 |
| S 38 | 95 | 72.00 | 268 | 391 | +29.8 | -30.5 |
| S 26A | 85 | 74.71 | 284 | 387 | +13.7 | -26.7 |
| S 36 | 95 | 75.12 | 266 | 383 | +26.5 | -30.6 |
| S 33 | 95 | 77.27 | 265 | 383 | +22.9 | -30.8 |
| S 28 | 90 | 78.84 | 275 | 385 | +14.1 | -23.6 |

† Data provided by the manufacturer. †† Mobilities calculated from manufacturer's resistivity data.
* Hall tests using "cold" indium contact technique [199(1*), 200(2*), 201(3*)].

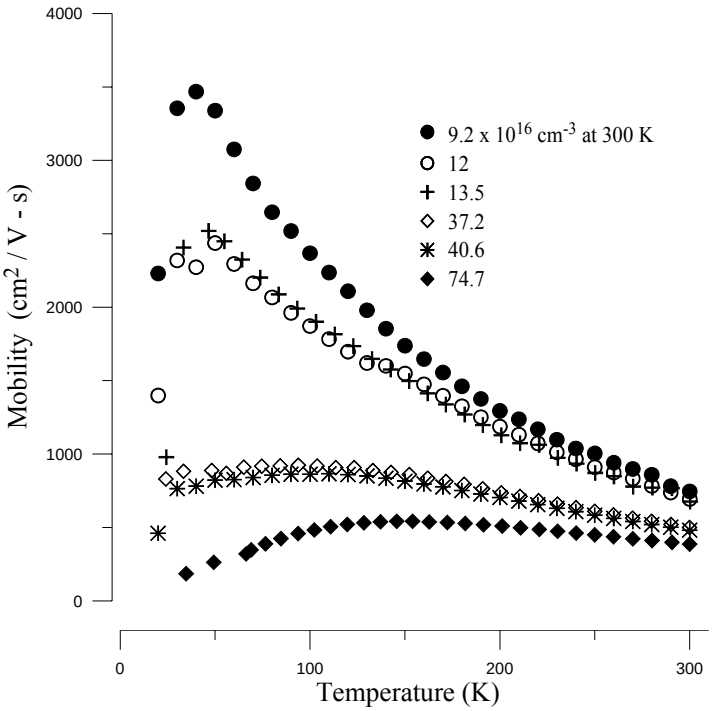


Fig. 23. Mobility versus temperature in n-type silicon samples in table VI.

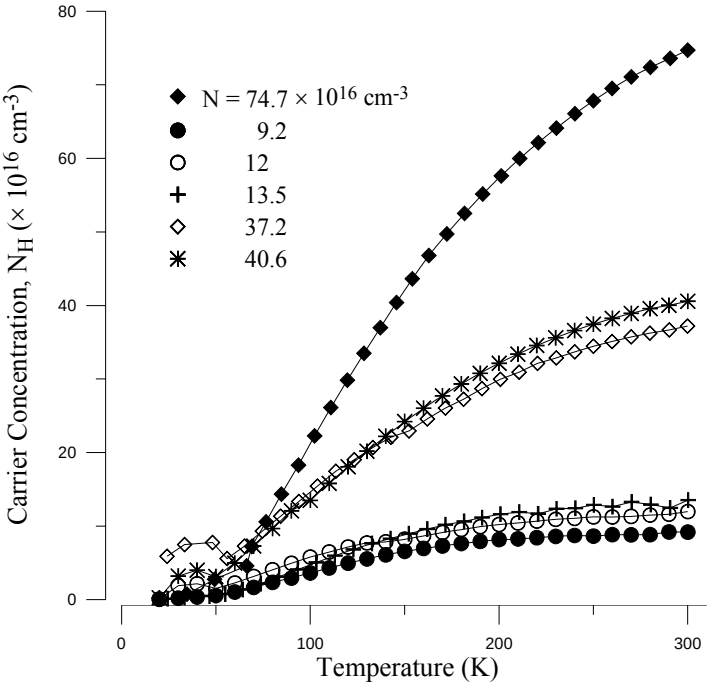


Fig. 24. Carrier concentration, $N_H \times 10^{16}$ cm$^{-3}$, versus temperature in n-type silicon samples from table VI.

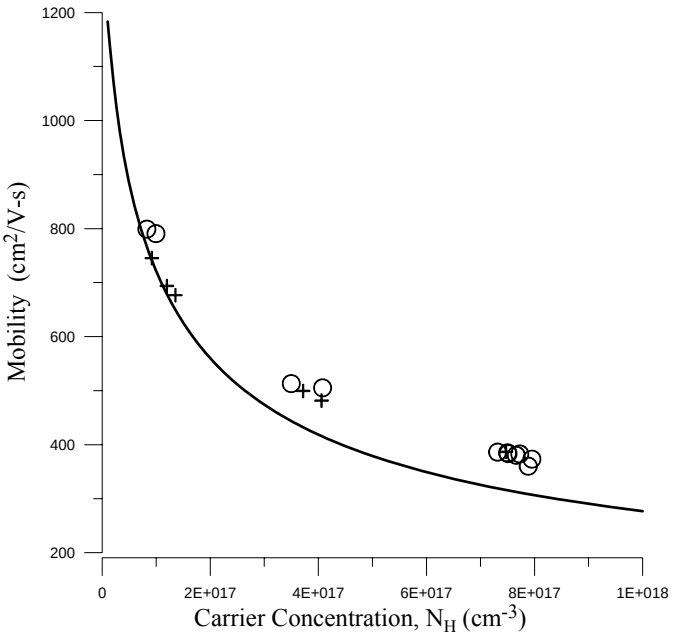


Fig. 25. Mobility versus carrier concentration in n-type silicon at 296 K. The solid line is an NBS reference mobility for silicon (ref. in the text). The symbols are Hall results obtained using cold indium contacts. The crosses represent the six silicon samples from table VI shown in figures 23 and 24. The open circles represent other silicon samples from table VI.

silicon sample results show consistently higher mobilities, as much as 21% higher for the heaver doped samples. Also shown in figure 25 are ten other samples taken from seven other wafers that show the same results. The standard curve is at 300 K and the sample data are at 296 K. This could account for some of the higher mobilities of these samples but not all. The data appears to be within limits of experimental variability in the literature [326, 339-340, 341-342]. Jacobi et al. [342] show results from three referenced sources which vary with the NBS results by -11% to +21% in the $10^{17}$ - $10^{18}$ $cm^{-3}$ range.

# CHAPTER III

# EXPERIMENTAL RESULTS

## A. HgCdTe

### Determination of effective mass and mobility

Faraday rotation measurements were made at room temperature on several $Hg_{1-x}Cd_xTe$ samples in the range $0.20 \leq x \leq 0.30$ using the Infrared Polarimeter at $CO_2$ laser wavelengths as described in Experimental Methods section (A) and shown schematically in figure 5 [202(6*), 318(9*)]. The laser was tunable between 9.2 and 10.8 μm and stable enough for consistent measurements at 9.3, 9.6, 10.3 and 10.6 μm. The interband and free carrier components were separated using a linear model:

$$\theta / LB = a\lambda^{-2} + b\lambda^{2} = m\lambda + b \qquad (27)$$

where the interband component, $a\lambda^{-2}$, is approximated with a $\lambda^{-2}$ dependence. m and b here are the slope and intercept of a plot of rotation, θ/LB, vs. λ. The coefficients, a and b, are solved for in terms of the slope and intercept of the plot at the four wavelengths. The spin flip component, a potentially very large component at low temperatures, is thought to have a $1/\lambda$ dependence, but it is not a factor at room temperature and $CO_2$ wavelengths. The constants, a and b, were determined using a linear regression plot. The constant, b, is the free carrier rotation component, equal to the right side of Eq. (13) at a particular wavelength. At 10.6 μm the constant is equal to:

$$\frac{\theta}{LB} = 1.69 \times 10^{-19} \frac{N}{m^{*2} n} \qquad (28)$$

in degrees/KG-mm. The only material dependent factors are the effective mass, m*, and the refractive index, n. A plot of carrier concentration vs. free carrier Faraday rotation normalized to the effective mass and refractive index would allow comparison on HgCdTe materials across the range of x. This plot is shown in figure 26 [202(6*), [318(9*)] across the range $0.20 \leq x \leq 0.30$ at 296 K. Interestingly, the plot is linear with carrier concentration for nearly intrinsic HgCdTe, at least, across the entire range. The carrier concentrations were determined by manufacturer's Hall tests. Variability of these "one-shot" Hall tests can

be as high as 20 to 40% [343]. Table III shows variability between manufacturer's tests and tests using the cold contact technique at ± 15%. This helps to explain the scatter in the plot. The effective mass ratio, m*, used to normalize the rotation in the plot is the band edge effective mass, $m^*_{be}$, at the bottom of the conduction band as formulated by Weiler [9]:

$$\frac{1}{m^*_{be}} = -0.6 + \left(\frac{19}{E_g}\right)\left(\frac{0.667 + E_g}{1 + E_g}\right) \tag{29}$$

The bandgap, Eg, is x dependent and was calculated using the empirical formula [330-331];

$$E_g = -0.302 + 1.93x + 5.35 \times 10^{-4} T(1 - 2x) - 0.810x^2 + 0.832x^3 \tag{30}$$

where the bandgap energy is in eV. The refractive index, n, at 300 K is given by the empirical formula [130]:

$$n_{300K} = \left(A + \frac{B}{1 - (C/\lambda)^2} + D\lambda^2 + E\lambda^4\right)^{1/2} \tag{31}$$

where A through E are empirical constants nearly linear in x given by:

$$A = -16.71x + 15.75, \quad B = 1.49x - 0.0896, \quad C = -33.13x + 13.36,$$

$$D = 157.8 \times 10^{-5} x - 142.4 \times 10^{-5}, \quad E = 337.6 \times 10^{-8} x - 99.9 \times 10^{-8}$$

for $0.20 \le x \le 0.30$

From Eq. (29) the theoretical slope of the plot in figure 26 is $1.69 \times 10^{-19}$ deg./KG-mm. The actual slope is $0.368 \times 10^{-19}$ deg./KG-mm, i.e. the theoretical slope is depressed by a factor of 4.59. This gives the effective mass ratio as $\sqrt{(4.59)} = 2.14$ times the $m^*_{be}$ value as calculated from Eq. (29) at 296 K. Ahrenkiel et al. [11] obtained a factor of 1.96 for an x = 0.37 n-type sample at room temperature. Elizarov et al. [12] estimated this factor, call it m**, as approximately 2 for several samples measured at room temperature for $0.20 \le x \le 0.26$.

Figure 27 shows absorption of several HgCdTe samples [202(6*)] including M26 (x = 0.248), M18 (x = 0.28) and M20 (x = 0.30) in table III. M26 appears on the bottom line with other samples grown by the SSR method from a single manufacturer, having no p-type cores. M18 and M20 and other samples grown by the melt-grown bulk material method

appear on the top curve. The 5 $cm^{-1}$ absorption offset between the two curves is absorption due to the p-type core, which appears to be fairly uniform among these samples from a single manufacturer. M010 (x = 0.199 n-type) is also a melt-grown bulk sample from another manufacturer. Its absorption indicates it also has a p-type core with a 5 $cm^{-1}$ offset. Because it is n-type, it has noticeably lower absorption than the samples on the top curve because electrons absorb less than holes in HgCdTe. The two solid lines are least squares regression plots fitted to the data. The slopes of these lines are identical at 4.65 $\times 10^{-16}$ $cm^2$. This is the combined cross section of holes and electrons in HgCdTe [129]. McOczkowski et al. [129] give the free electron cross section, $\sigma_n$, as $3 \times 10^{-19} \lambda^{2.4}$ $cm^2$. This works out to 0.87 $\times 10^{-16}$ $cm^2$ at 10.6 μm. Using transmission data for moderately doped n and p-type Hg1-xCdxTe for x = 0.20 in [129], the hole cross section, $\sigma_p$, at 10.6 μm is approximately $3.56 \times 10^{-16}$ $cm^2$. This gives a combined free carrier cross section of $4.43 \times 10^{-16}$ $cm^2$, which is within 5% of the slopes in figure 27. Although the data given in [129] is for x = 0.20, figure 27 indicates that the calculated cross sections hold across the entire range for $0.20 \leq x \leq 0.30$. Figure 28 shows a plot of electron mobility vs. x in several HgCdTe samples [202(6*)]. The solid curve is an empirically derived formula for electron mobility in $cm^2$/V-s used as a reference given by [272]:

$$\mu_e = (8.754 \times 10^{-4} x - 1.044 \times 10^{-4})^{-1} \tag{32}$$

The formula is applicable to undoped HgCdTe at 300 K. The crosses and starred symbols are actual hall tests from the manufacturer. Crosses represent samples made using the melt grown/Hg anneal bulk method (p-core). The stars represent samples made by the SSR method. The open symbols, circles and triangles, represent mobilities for these samples determined using a ratio of Faraday rotation to free carrier absorption according to Eq. (11). HgCdTe contains a large number of intrinsic carriers due to its small bandgap. Large numbers of both holes and electrons are present. There is no known method of separating hole and electron absorptions to be able to apply Eq. (11). In this case the free electron absorption was calculated using the absorption cross sections for holes and electrons introduced above. An empirical formula for the x dependent intrinsic carrier concentration in $cm^{-3}$ is given by [331, 334];

$$n_i = 5.585 - 3.820\,x + 1.753 \times 10^{-3} T - 1.364\,x \times 10^{-3} T \times [10^{14} E_g{}^{3/4} T^{3/2} \exp(-E_g / 2k_b T)] \tag{33}$$

Using $N_H = n_e$, the electron concentration, and $n_h = n_i^2/N_H$, the hole concentration, the free carrier absorption, α, can be calculated using $\alpha = n_e\sigma_n + n_h\sigma_p$, and the free electron absorption is $N_H\sigma_n$. For figure 28 the proportionality "C" in Eq. (11) was arbitrarily assigned a value of one. The dashed line is a simple calculation of the ratio of Faraday rotation (FR)/absorption (α). The FR was calculated using $m^* = m^{**}m^*_{be}$ from Eq. (34), $N_H$ from the cold contact Hall tests, and n, the refractive index, from Eq. (31) in Eq. (28). Absorption was calculated from $\alpha = N_H\sigma_n$. Mobility was then calculated using FR and α in Eq. (11) with C = 1. As can be seen in the figure, this ratio gives fairly good results, with mobilities falling between the reference curve and the Hall test mobilities. Note that all the mobilities lie more or less along the reference curve with no apparent trend of deviations distinguishable due to method of manufacture or the presence or absence of a p-core. Presumably, the n-p-n structure of the melt grown samples does not effect their mobility.

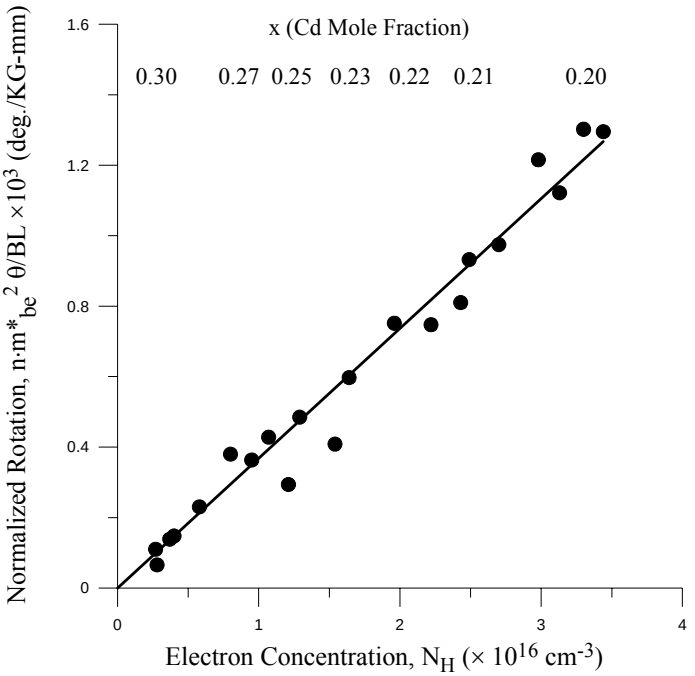


Fig. 26. Normalized rotation in $Hg_{1-x}Cd_xTe$ for B = 0.1 T at 10.6 microns vs. carrier concentration for $0.20 \le x \le 0.30$ at 296 K. The symbols are sample data. The solid line is a least-squares fit to the data.

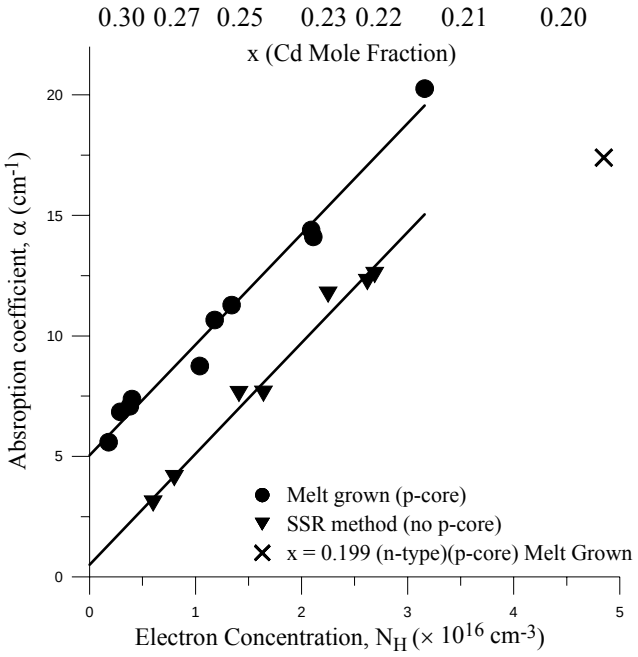


Fig. 27. Free Carrier absorption at 10.6 μm at 296 K in $Hg_{1-x}Cd_xTe$ for $0.20 \le x \le 0.30$. The solid lines are least squares fits to the data. The top line is absorption are bulk melt grown/Hg annealed samples. The absorption offset is due to the remnant p-type core. The samples on the bottom line are SSR samples with no p-type core.

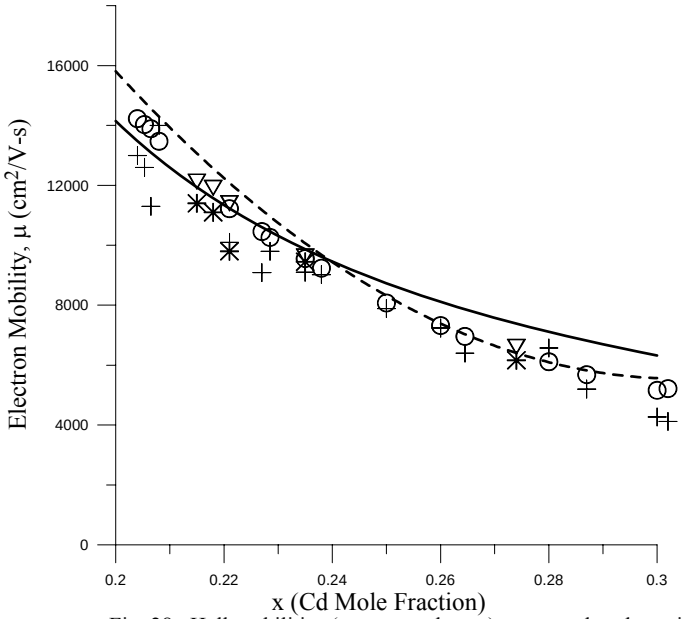


Fig. 28. Hall mobilities (crosses and stars) compared to the ratio; $\theta_p$(measured)/($\alpha = n_i\sigma_n$) (Open circles and triangles) at 10.6 μm. The solid curve is an empirical reference for intrinsic HgCdTe at 300 K [272]. The dotted curve is the ratio of calculated Faraday rotation (using m** in Eq. (13)) to calculated absorption in Eq. (11) with C = 1.

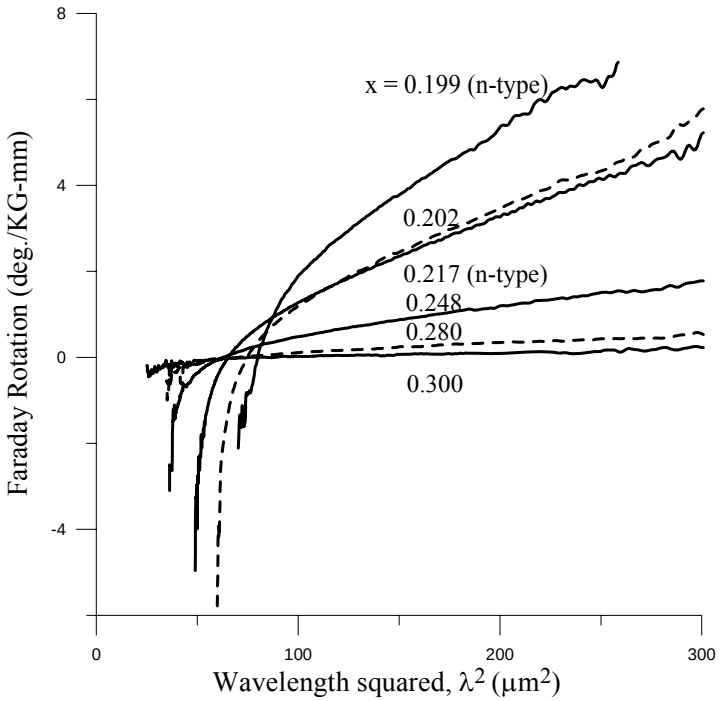


Fig. 29. Faraday rotation spectra of $Hg_{1-x}Cd_xTe$ for $0.20 \leq x \leq 0.30$ at 296 K.

Faraday rotation in narrow band semiconductors such as InSb and HgCdTe used in infrared detector materials consists of two main components. These are components due to; intraband movement and energy transitions of free carriers in the conduction band, called the free carrier or plasma component; and interband components, rotation due to free carriers transitioning band to band across the forbidden gap, and rotation due to electrons changing their spin state due to the magnetic field, or the spin-flip component. Figure 29 shows Faraday rotation versus $\lambda^2$ for six HgCdTe samples [199(1*), 200(2*), 210(3*), 322(8*)]. Four of the samples are nearly intrinsic, that is, they contain very little doping. In HgCdTe non-stoichiometric Hg is thought to cause n and p-type doping, i.e. excess interstitial Hg causes n-type and Hg vacancies in the lattice cause p-type doping. Two of the samples in the figure are slightly n-type. The six $Hg_{1-x}Cd_xTe$ samples range in cadmium mole fraction, x, between 0.20 and 0.30. These spectra were obtained at room temperature (296 K).

At smaller wavelengths on the left side of figure 29, higher light energies are more likely to promote light assisted transitions of free carriers across the forbidden gap. In this region the interband component is favored. The interband component has an approximate

$1/\lambda^2$ dependence and is negative for HgCdTe, InSb, and GaAs. The $1/\lambda^2$ dependence causes the Faraday rotation plot to curve steeply when plotted against $\lambda^2$. This can be seen at the extreme left of the figure. At lower light energies toward the right in the figure, light assisted interband transitions are less favored. The free carrier component of the Faraday rotation is proportional to $\lambda^2$ according to the equation [13]:

$$\theta_P = \frac{e^3 BL}{8\pi^2 c^3 \varepsilon_o n m_o^2} \frac{N\lambda^2}{m^{*2}} \tag{13}$$

$\theta_p$ is the free carrier rotation or the rotation due to the electron plasma, in this case, due to electrons. Rotation due to holes is insignificant due to the large effective mass of holes compared to electrons in HgCdTe and InSb. The free carrier or linear region of the HgCdTe rotation plots in figure 29 are clearly visible above 10 microns or so. Here the linear region dominates and the slope of the line floats above the total rotation. The actual rotation values read along the y axis are the sum of the two components but the linear slope of the free carrier region is uncorrupted (except for noise) and can be used to determine the effective mass according to Eq. (13). Figure 30 shows effective masses measured in HgCdTe between 77 K and 296 K for samples between $0.20 \leq x \leq 0.30$ using slopes of Faraday rotation vs. $\lambda^2$ spectra [199(1*), 200(2*)] as shown in figure 29. The symbols are experimental measurements and the lines are band edge effective masses, $m^*_{be}$, calculated according to Eq. (29). As can be seen in the figure, the measured effective masses diverge significantly from the band edge effective masses with temperature. The measured plots are larger in both magnitude and rate of increase (slope) than the $m^*_{be}$ plots. All effective masses measured or calculated in the figure are practically linear with temperature. This suggests a linear compensation factor, m**, where $m^{**} = m^*/m^*_{be}$. Figure 31 shows a plot of m** for the six samples in table III and figures 29-30. The compensation factor for the four nearly intrinsic samples falls on the same line, indicating a unique compensation factor applicable to the $0.20 \leq x \leq 0.30$ range. A regression plot gives the equation of the line and the empirical formulation of m** (unitless) as:

$$m^{**} = 4.52 \times 10^{-3} T + 0.78 \qquad \text{for } 77\text{ K} \leq T \leq 296\text{ K}, \quad 0.20 \leq x \leq 0.30 \tag{34}$$

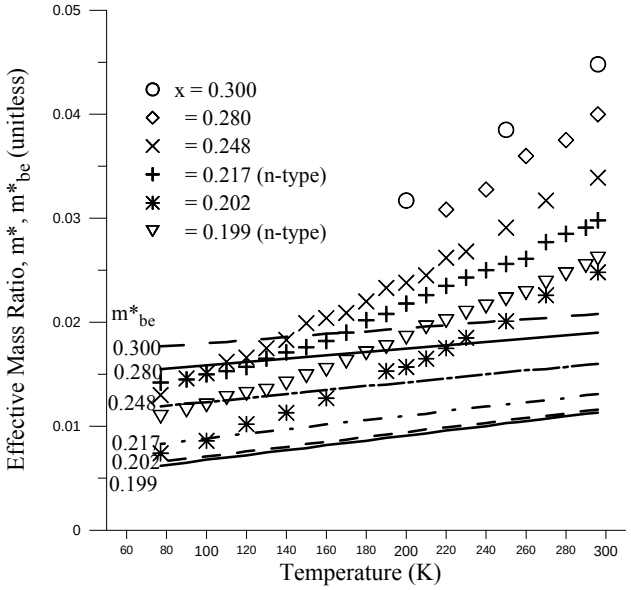


Fig. 30. Effective mass ratios for $Hg_{1-x}Cd_xTe$ for $0.20 \le x \le 0.30$ for four nearly intrinsic samples and two n-type samples with residual carrier concentrations of approximately $1.2 \times 10^{16}$ $cm^{-3}$ above the intrinsic level. Measured m* values are shown as symbols. The lines are plots of band edge effective mass, $m^*_{be}$, using Weiler's formula [9].

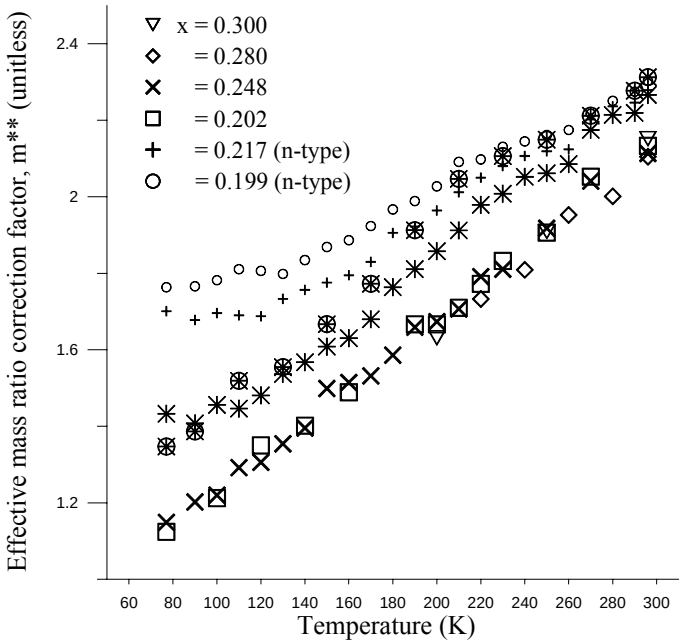


Fig. 31. Effective mass ratio correction factor, m**, where $m^* = m^{**}\ m^*_{be}$, for $Hg_{1-x}Cd_xTe$ and $0.20 \le x \le 0.30$ samples of Fig. 30. The star symbol plots are the correction factor for the two n-type samples corrected for the enlarged band gap due to the Moss-Burstein effect.

Figure 30 also shows that effective masses rise faster in n-type samples. This can be seen by comparing the lines and symbols for the nearly intrinsic x = 0.20 sample and the x = 0.199 n-type sample. The rise in effective masses with temperature and carrier concentration is a consequence of the non-parabolic band as predicted by Balkanski et al. [186]. At 296 K, m** according to Eq. (34) is 2.12. This is within 1% of the value obtained (2.14) with the infrared polarimeter method using the linear separation method at $CO_2$ wavelengths. The two methods are completely different using two completely different apparatus. The m** values for the two n-type samples shown as ○ and + symbols in figure 31 are larger. The plots appear linear with smaller slopes down to a temperature between 140 K and 110 K where they bend. Figure 32 shows Fermi energy, $E_f$, and bandgap energy, Eg, plotted in $k_bT$ units, where $k_b$ is the Boltzmann constant, for the two samples. The plot shows that the x = 0.199 sample is degenerate ($E_f > Eg$) at approximately 296 K and below and the x = 0.217 sample is degenerate at approximately 165 K and below. The degeneracy points and the knees in the curves of figure 31 do not correspond, so this effect does not seem to explain them. $E_f$ was calculated using carrier concentrations and the following expressions [280];

$$N = \frac{1}{2\pi}\left(\frac{3E_g k_b T}{2P^2}\right)^{\frac{3}{2}} \frac{E_g}{k_b T} \int_{\frac{E_g}{k_b T}}^{\infty} \frac{\lambda_c(y)}{\exp\left(y - \frac{E_f}{k_b T}\right) + 1} dy \qquad (35)$$

where,

$$\lambda_c(y) =$$

$$3\left[2\left(\frac{E_g}{\Delta}\right)^2 \frac{k_b T}{E_g} y + \frac{E_g}{\Delta}\left(3 - \frac{E_g}{\Delta}\right)\left(\frac{k_b T}{E_g} y\right)^2 + \frac{4}{3}\left(1 - \frac{E_g}{\Delta}\right)\frac{k_b T}{E_g} y - \frac{2}{3}\right]$$

$$\times \left[\frac{k_b T}{E_g} y\left(\frac{k_b T}{E_g} y - 1\right)\left(\frac{k_b T}{\Delta} y + 1\right)\right]^{\frac{1}{2}} \Bigg/ 2\left(\frac{3}{2}\frac{k_b T}{\Delta} y - 1\right)^{\frac{5}{2}}$$

The Δ term is the spin orbit splitting = -0.18 x + 1.08 eV. P is the momentum matrix element, $P = 8.55 \times 10^{-8}$ eV -cm [344-345]. $E_f$ appears in the exponent of the natural base e term in the denominator of the integrand. It is determined by assigning $E_f$ an initial value and successively iterating Eq. (35) until the equation yields back the assigned electron concentration to the desired accuracy.

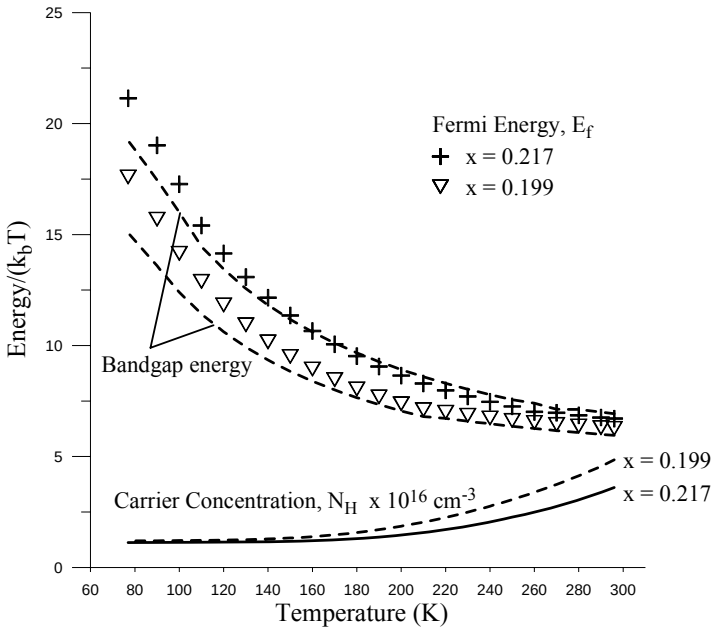


Fig. 32. Measured band gap energy, $E_g$, (dotted lines) and Fermi energy, $E_f$, (symbols) calculated according to Eq. (35), plotted in $k_bT$ units vs. temperature for two n-type $Hg_{1-x}Cd_xTe$ samples. The plot shows the x = 0.199 sample is degenerate ($E_f > E_g$) at 296 K and below. The x = 0.217 sample is degenerate at approximately 165 K and below. Carrier concentrations for the two samples are also plotted.

In narrow gap semiconductors like InSb and HgCdTe, the addition of donor electrons causes the bandgap to become effectively larger as lower energy states with their lower density of states fill up. With the lower energy states filled, electrons from the valance band are required to traverse a larger effective bandgap to enter the conduction band according to the Moss-Burstein effect [148]. This effect becomes more pronounced at lower temperatures because the density of states decreases with temperature and in HgCdTe the bandgap decreases with temperature. The bandgap formula, Eq. (30), does not apply to moderately or heavily doped HgCdTe because it does not take this effect into account. The bandgap of the two n-type samples was measured every 10 or 20 K using their infrared transmission spectra according to the 1% transmission cut-on method described previously. The band edge effective mass, $m^*_{be}$, was then recalculated according to Eq. (29). The curves plotted with star symbols in figure 31 show m** for the n-type samples with the corrected bandgap. The knees in the curves have all but disappeared. The slopes of the two corrected plots are similar. The average slope of the two plots is $4.31 \times 10^{-3}$ which is within 5% of the slope of the intrinsic plot. The average m** offset of the x = 0.199 plot with

residual carrier concentration of $1.2 \times 10^{16}$ $cm^{-3}$ (at 77 K) is 0.23 and for the x =0.217 sample with residual carrier concentration of $1.12 \times 10^{16}$ $cm^{-3}$ is 0.166. The effective mass of these two samples can be obtained by adding the offset to m** as formulated in Eq. (34). There now appears to be three parallel plots, intrinsic and two n-type, with a constant gap in between (the offsets), resulting in a larger compensation factor for the n-type materials. This appears to show that electrons in the n-type materials have higher energies and, therefore, larger effective masses on the average than electrons in the intrinsic samples.

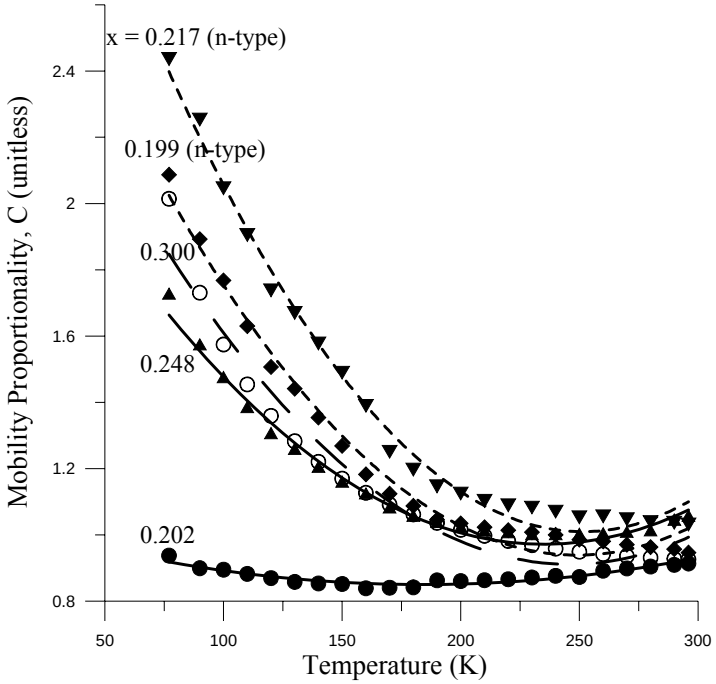


Fig. 33. Proportionality between electron mobility and the ratio of Faraday rotation and electron absorption in Eq. (11) in $Hg_{1-x}Cd_xTe$ for $0.20 \leq x \leq 0.30$ vs. temperature for three nearly intrinsic and two n-type samples calculated at 15 μm.

$Hg_{1-x}Cd_xTe$ for $0.20 \leq x \leq 0.30$ has intrinsic carrier concentrations on the order of $10^{16}$ $cm^{-3}$. The ratio of hole to electron absorption is about 4 to 1. The proportionality, "C", in Eq. (11) was calculated versus temperature for HgCdTe in the x = 0.20 to 0.30 range. It was necessary to, again, use an absorption cross section for the free electron absorption. The cross section used previously, $\sigma_n = 3.0 \times 10^{-19} \lambda^{2.4}$ [129] was used at 15 μm to allow for the small bandgaps at low temperatures. The cross section is apparently only weakly dependent on temperature, dropping about 20% at 77 K [142]. The cross section was considered constant with temperature calculating the proportionality plotted in figure 33 [200(2*),

201(3*)]. The wavelength dependence of holes in HgCdTe is $\lambda^2$ and $\lambda^{2.4}$ for electrons. It is tempting to try a plot of absorption vs. $\lambda^{2.4}$ to extract the electron component as the slope, but the wavelength dependencies are probably too close for conventional curve fit techniques. So this remains the problem using Eq. (11) to determine mobility in small bandgap materials with large intrinsic carrier concentrations.

**Interband and Spin Flip Faraday Rotation in HgCdTe and InSb**

Faraday rotation in semiconductors consists of three main components. The plasma component discussed in previous sections has been well established. Measurements of interband rotation in InSb, InAs, and GaAs are given in [222, 346] and discussed in detail in [230, 347]. The least characterized component is the spin-flip component. This is rotation due spin flip transitions of free conduction band electrons in the magnetic field. Jiménez-González et al. [348] describes it as due to virtual transitions of electrons from occupied states in the conduction band to intermediate energy states in the valence band. The effect saturates at higher magnetic fields as the spins of all the available free electrons align with the field. The theory was advanced by Romestain et al. [349] using a connection between spin Faraday rotation and spin-flip Raman scattering in [350-351]. Spin induced Faraday rotation was measured in HgCdTe at 2 K by Yuen et al. [203], who further advanced the theory based on Raman scattering spin-flip scattering cross-section. Aggarwal et al. [206] measured Faraday rotation in InSb at 6 K. They formulated the spin-flip Faraday rotation, $\theta_s$, explicitly in terms of the bandgap resonance condition and, $g_c$*, the conduction electron g factor. The spin-flip expression was refined just a bit further by Syllaios et al. [204(7*)] by explicitly formulating the average spin alignment factor $<\sigma_z>$, in terms of the Brillouin function. Aggarwal et al. [206] used theoretical expressions for the three components to explain their experimental results as did Syllaios et al. [204(7*)]. The purpose of this section is to examine the theoretical model they presented.

**Theory of Faraday rotation components**

The free carrier plasma component in cgs units is given by [164]:

$$\theta_p = \frac{2\pi e^3 NBL}{c^2 n m_o^2 \omega^2 m^{*2}} \frac{180}{\pi} \tag{36}$$

$\theta_p$ is in deg/KG-cm. Here e is the electron charge, 4.803 x $10^{10}$, in electrostatic units. B is magnetic field in KG, N is the free carrier concentration per cubic cm, m* is the effective mass ratio, n is the refractive index, $\omega$ is the angular frequency of light, and L is the sample thickness. The theoretical band edge effective mass in $Hg_{1-x}Cd_xTe$ is given by several expressions in the literature. The expression below is used in the Syllaios model and gives $m^*_{be}$ values close to the expression given in Eq. (29) in the previous section [352];

$$m^*_{be} = \frac{1}{1 + 2F + \frac{1}{3}E_p\left(\frac{2}{E_g} + \frac{1}{E_g + \Delta}\right)} \tag{37}$$

F and $E_p$ are band parameters with values of F = -0.8 eV and $E_p$ = 19 eV. $\Delta$ is the valence band spin-orbit splitting energy equal to 1 eV for HgCdTe. The bandgap, Eg, is dependant on Cd mole fraction, x, and temperature, T, and is given by the empirical formula [352];

$$E_g = -0.302 + 1.93x + \left[5.35(1 - 2x) \times 10^{-4}\left(\frac{1882 + T^3}{255.2 + T^2}\right)\right] - 0.810x^2 + 0.832x^3 \tag{38}$$

The intrinsic carrier concentration in $Hg_{1-x}Cd_xTe$ is also dependant on x and T and is given by [352];

$$n_i = (5.24256 - 3.5729x - 4.74019 \times 10^{-4}T + 0.0125942xT - 5.77046x^2 - 4.24123 \times 10^{-6}T^2)$$

$$\times 10^{14}\left[E_g(x, T)^{\frac{3}{4}} T^{\frac{3}{2}} \exp\left(\frac{-E_g(x, T)}{2k_bT}\right)\right] \tag{39}$$

The interband component, $\theta_i$, was taken from Roth [347];

$$\theta_i = KF(\chi)BL \tag{40}$$

$$K = \frac{5.17f}{n\sqrt{E_g}}\left[\left(\frac{\mu_h}{m_o}\right)^{\frac{3}{2}} + \left(\frac{\mu_l}{m_o}\right)^{\frac{3}{2}}\right]g_{eff} \tag{41}$$

K is in deg/KG-cm. $f = 3(2 - g^*)(E_g + \Delta)/2\Delta$ [10]. $\mu_h$ and $\mu_l$ are the reduced effective masses for interactive transitions between the conduction band and the heavy hole and the light hole bands respectively. Expressions for them are given below [230, 347];

$$\mu_h = \frac{m_c m_o m_{vh} m_o}{m_c m_o + m_{vh} m_o} \quad ; \quad \mu_l = \frac{m_c m_o m_{vl} m_o}{m_c m_o + m_{vl} m_o} \tag{42}$$

where $m_c = 1/a_c$,

$$a_c = 1 + f\frac{(3E_g + 2\Delta)}{3(E_g + \Delta)} \tag{43}$$

$m_{vh}$ and $m_{vl}$ are the effective mass ratios for the heavy and light holes, respectively, in the valence band and are given by [347];

$$m_{vh} = \frac{1}{\gamma_1 - 2\bar{\gamma}} \quad ; \quad m_{vl} = \frac{1}{\gamma_1 + 2\bar{\gamma}} \tag{44}$$

$g_{eff}$ is given by [347];

$$g_{eff} = -g^* - 10\kappa + 10\bar{\gamma}\frac{r^3 - 1}{r^3 + 1} - \frac{4(\gamma 1 - \bar{\gamma} - \kappa)(r^3 - 1)(r - 1)}{(r^3 + 1)(r + 1)} \tag{45}$$

where $r = (\mu_h/\mu_l)^{1/2}$. The quantities, $\kappa$, $\bar{\gamma}$, and $\gamma_1$, are the Luttinger band parameters and are given for HgCdTe by [9];

$$\gamma_1 = 3.3 + 6.333 / E_g \qquad \bar{\gamma} = 0.6 + 3.167 / E_g$$
$$\kappa = -0.8 + 3.167 / E_g \tag{46}$$

g*, the conduction electron g factor is given by [204(7*)];

$$g^* = 2 - \frac{2}{3}E_p\left(\frac{1}{E_g} - \frac{1}{E_g + \Delta}\right) \tag{47}$$

Finally, the function F(χ) is given by [347];

$$F(\chi) = \frac{1}{\chi}\left(\frac{1}{\sqrt{1-\chi}} - \frac{1}{\sqrt{1+\chi}}\right) - \frac{4}{\chi^2}\left(2 - \sqrt{1-\chi} - \sqrt{1+\chi}\right) \tag{48}$$

where $\chi = \hbar\omega / E_g$, and $\hbar = h/2\pi$, where h is Plank's constant.

The spin-flip component, $\theta_s$, in deg/KG-cm is given by [204(7*),206];

$$\theta_s = g^* \frac{\pi\hbar e^2}{m_o c} \frac{NL}{nE_g} \frac{\frac{180}{\pi}}{1-\left(\frac{\hbar\omega}{E_g}\right)^2} \langle\sigma_z\rangle \tag{49}$$

where the average spin alignment, $<\sigma_z>$, is given by [204(7*)];

$$\langle\sigma_z\rangle = \mathrm{Tanh}\left[\left|g^*\right|\mu_B \frac{B}{2k_b T}\right] \tag{50}$$

Where $\mu_B$ is the Bohr magnetron, $\mu_B = e\hbar/2m_o c = 9.274 \times 10^{-18}$ erg/KG, and $k_b$ is the Boltzmann constant in ergs/K.

Figure 34 shows a theoretical plot of the three components versus temperature in $Hg_{1-x}Cd_xTe$ at 10 KG, and 10.6 microns, for x = 0.225. They match Syllaios et al.'s [204(7*)] results fairly closely. The plasma component dominates at higher temperatures where free carriers are more numerous, the bandgap is larger, and the spin and interband components are further from resonance. At lower temperatures, the plasma component drops with the number of thermally generated carriers. It levels off a bit at lower temperature because of the drop in effective mass with temperature. Figure 34 shows large interband and spin components as the 10.6 micron light approaches the bandgap energy as the bandgap decreases with temperature. These components get much larger as resonance is approached further.

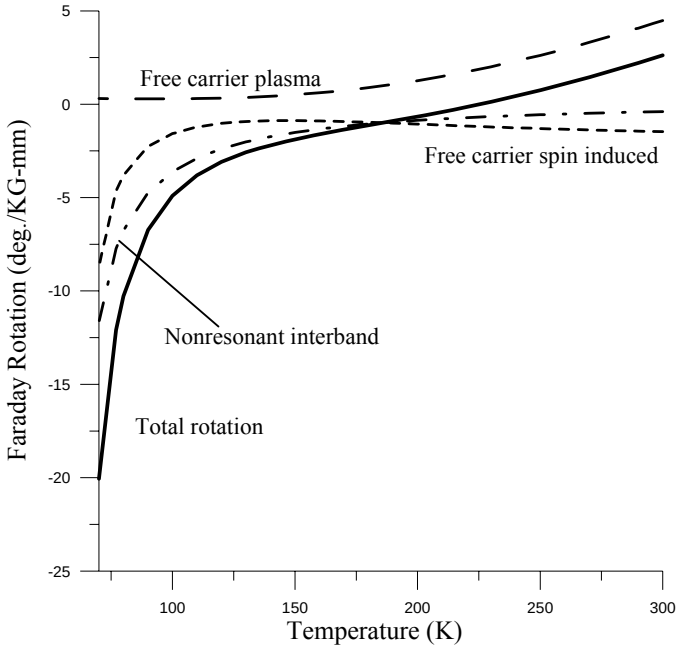


Fig. 34. Theoretical calculation of Faraday rotation components in $Hg_{1-x}Cd_xTe$ vs. temperature for x = 0.225 at 10.6 μm, after Syllaios et al. [204(7*)].

**Comparison of experimental results to Faraday rotation theory**

Figure 35 shows the calculated components versus temperature compared to experimental results in $Hg_{1-x}Cd_xTe$ for x = 0.202 and 0.119 eV < Eg < 0.156 eV between 180 K and 296 K. The energy of the 10.6 micron light is 0.117 eV. The experimental values differ considerably from the calculated total rotation. The spin component is the largest component and is almost equal to the net total rotation. The experimental results follow the combined interband and plasma curve fairly closely at 240 K and above but diverge as the interband component rapidly increases as the sample approaches resonance at lower temperatures. The band edge effective mass, $m^*_{be}$, was used in the theoretical curves of figure 34 to compare these curves to Syllaios et al.'s [204(7*)] results. In all the figures after figure 34 the effective mass, $m^*_{be}$, has been adjusted with the compensation factor, m**, in Eq. (34). Figure 36 shows the same plot for $Hg_{1-x}Cd_xTe$ with x = 0.248 and 0.160 eV < Eg < 0.219 eV between 77 K and 296 K. The experimental values, again, follow the combined interband and plasma curve fairly closely above 160 K or so and come closer to the total rotation curve below 160 K. This is a general trend that increases as the measurements get further from resonance and the spin and interband components start to rapidly decrease.

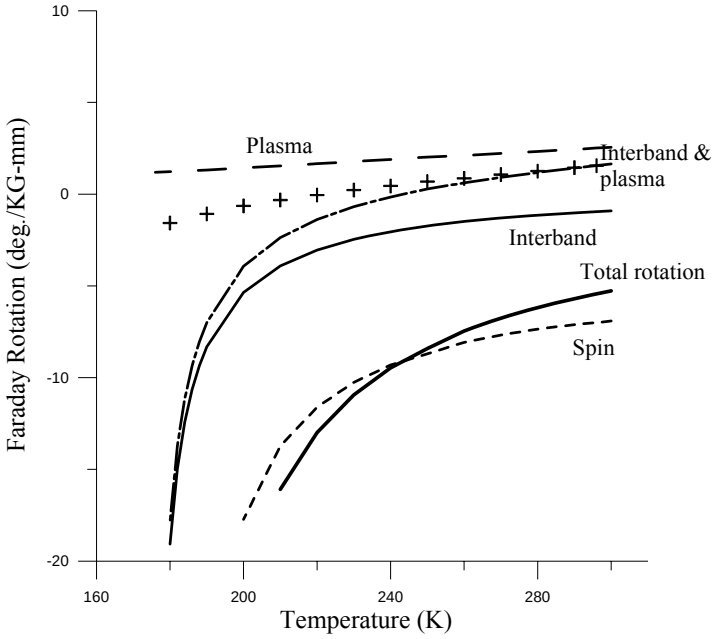


Fig. 35. Theoretical calculation of Faraday rotation components in $Hg_{1-x}Cd_xTe$, x = 0.202, vs. temperature at 10.6 μm. Symbols represent experimental values.

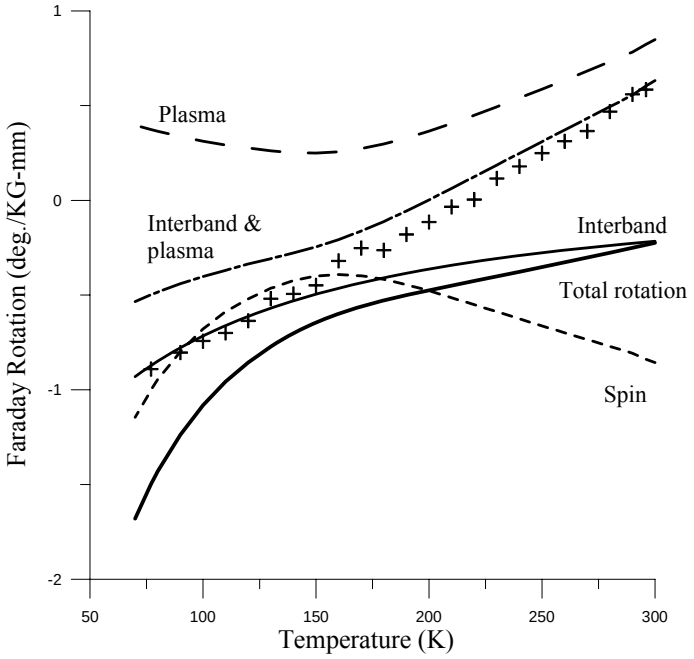


Fig. 36. Theoretical calculation of Faraday rotation components in $Hg_{1-x}Cd_xTe$, x = 0.248, vs. temperature at 10.6 μm. Symbols represent experimental values.

In figure 37 the experimental values come closest to the combined interband/plasma curve. Here x = 0.280 and 0.211 eV $\leq$ Eg $\leq$ 0.263 eV for 77 K $\leq$ T $\leq$ 296.

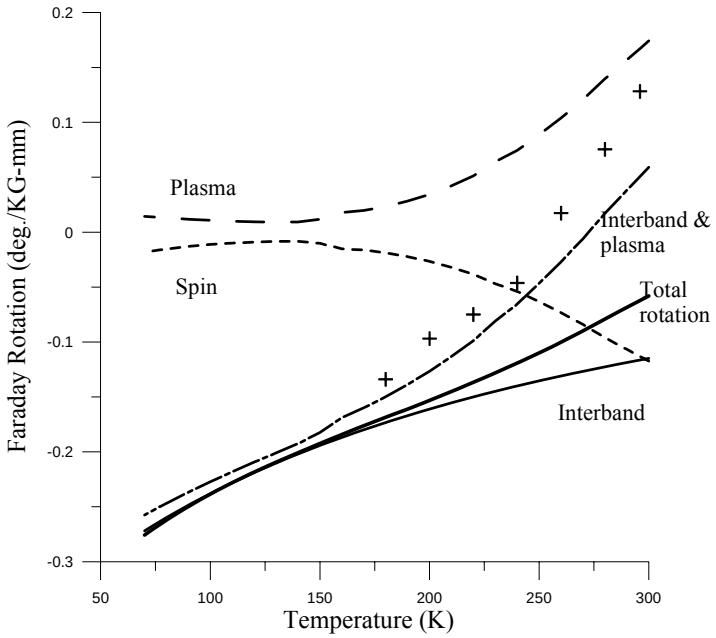


Fig. 37. Theoretical calculation of Faraday rotation components in $Hg_{1-x}Cd_xTe$, x = 0.280, vs. temperature at 10.6 μm. Symbols represent experimental values.

Finally, figure 38 shows a nearly intrinsic sample of InSb where 0.222 eV ≤ Eg ≤ 0.18 eV for 77 K ≤ T ≤ 296 K. The experimental values fit the total rotation curve fairly well and diverge a bit above about 220 K coming closer to the combined interband/plasma curve as the temperature increases and bandgap decreases. In InSb the bandgap decreases with increasing temperature, the opposite of HgCdTe.

As mentioned in the previous section, in narrow gap semiconductors like HgCdTe, the bandgap effectively increases as donors are added to the material resulting in the Moss-Burstein effect [148]. Since the model is very sensitive to bandgap, this is an important effect and must be accounted for in the two slightly n-type HgCdTe samples. The cut-on wavelength, $\lambda_{co}$, was measured as described in the previous section in the two samples at temperatures between 77 K and 296 K and plotted in figure 39. The solid lines are calculated values of Eg for intrinsic HgCdTe according to Eq. (30). Note in the figure, the bandgap enlargement effect increases with decreasing temperature as the intrinsic bandgap

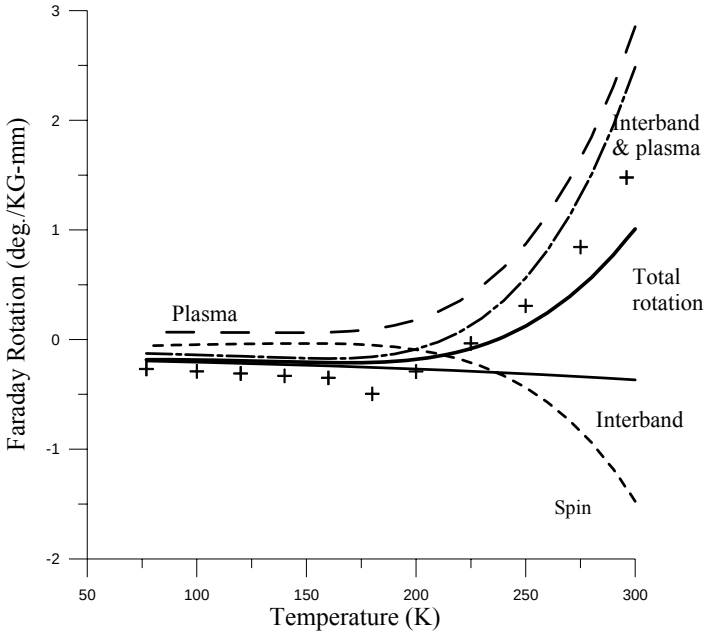


Fig. 38. Theoretical calculation of Faraday rotation components in nearly intrinsic InSb at 10.6 μm. $N_H$ at 296 K = $1.8 \times 10^{16}$ $cm^{-3}$. The symbols represent experimental values.

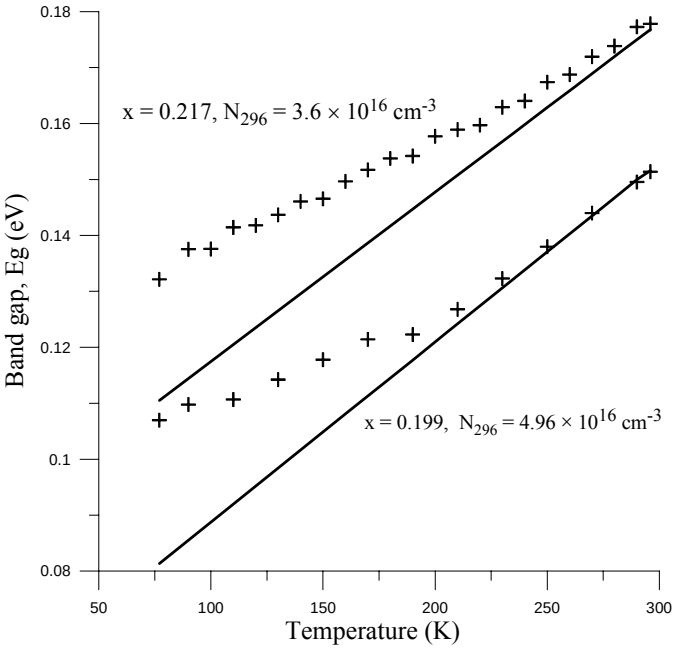


Fig. 39. Moss-Burstein effect in slightly n-type $Hg_{1-x}Cd_xTe$. The symbols are measured Eg values for two n-type samples (x = 0.199 & 0.217) at 296 K with residual carrier concentrations ~$1.1 \times 10^{16}$ $cm^{-3}$. The solid lines are calculated intrinsic values of Eg from Eq.(30).

decreases. The effect is arguably non-existent at room temperature, at least for this level of doping ( ~ 1.1-1.2 × $10^{16}$ $cm^{-3}$).

Figures 40 and 41 show experimental versus calculated Faraday rotation for the two slightly n-type samples adjusted for their larger bandgaps. They are also adjusted for larger effective masses with an added offset in m** of 0.23, determined from the data of figure 31, for the x = 0.199 sample with residual concentration of 1.19 × $10^{16}$ $cm^{-3}$, and 0.166 for the x = 0.217 sample with residual concentration of 1.1 × $10^{16}$ $cm^{-3}$. In figure 40, x = 0.199, $N_H$ at 296 K = 4.96 x $10^{16}$ and 0.104 eV ≤ Eg ≤ 0.149 eV between 77 K and 296 K and in figure 41, x = 0.217, $N_H$ at 296 K = 3.6 x $10^{16}$ and 0.129 eV ≤ Eg ≤ 0.175 eV between 77 K and 296 K. The two plots follow the combined interband/plasma curves fairly closely. The larger bandgap sample in figure 41 trends slightly toward the total rotation curve below 200 K. Notice the upward arc of the theoretical plasma component at lower temperatures as the plasma rotation increases with the decreasing effective mass of the large residual donor concentration.

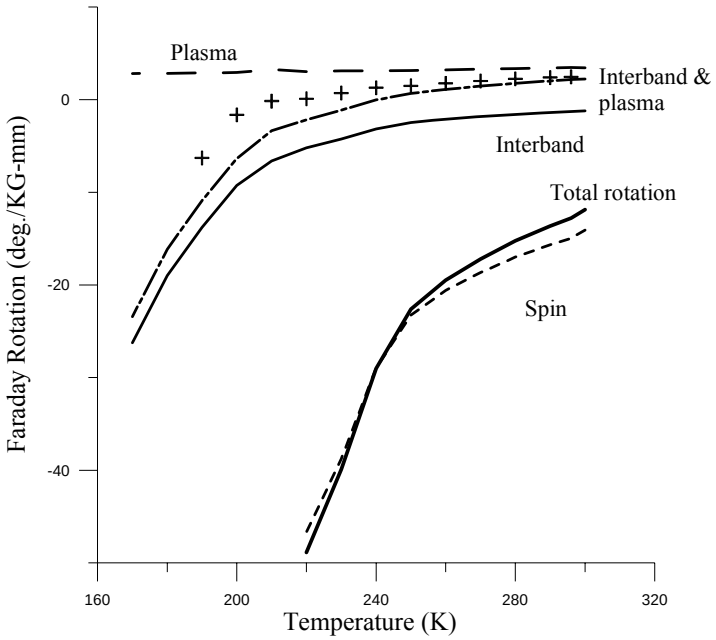


Fig. 40. Theoretical calculation of Faraday rotation components in a slightly n-type $Hg_{1-x}Cd_xTe$ sample, x = 0.199, at 10.6 μm. The symbols represent experimental values. The theoretical calculations used measured values of carrier concentration, $N_H$, and bandgap, Eg, at 20 K intervals so show a little scatter.

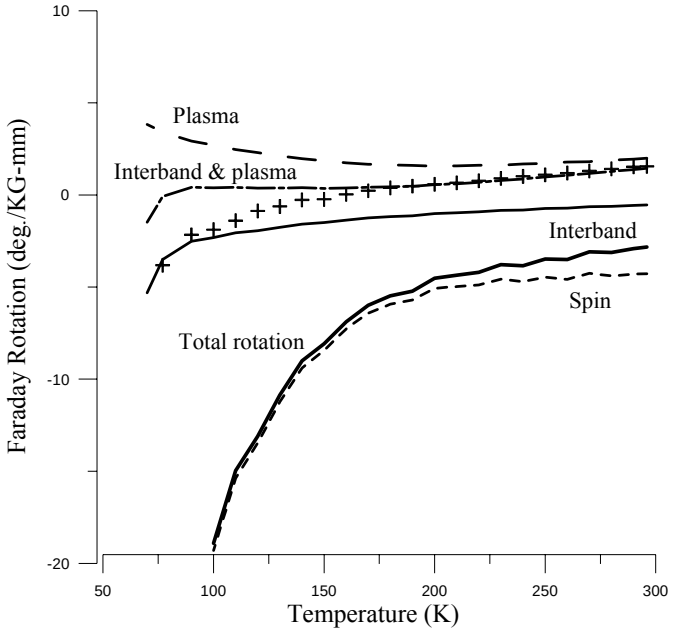


Fig. 41. Theoretical calculation of Faraday rotation components in a slightly n-type $Hg_{1-x}Cd_xTe$ sample, x = 0.217, at 10.6 μm. The symbols represent experimental values. The theoretical calculations used measured values of $N_H$, and Eg at 10 K intervals, so show a little wavyness and scatter.

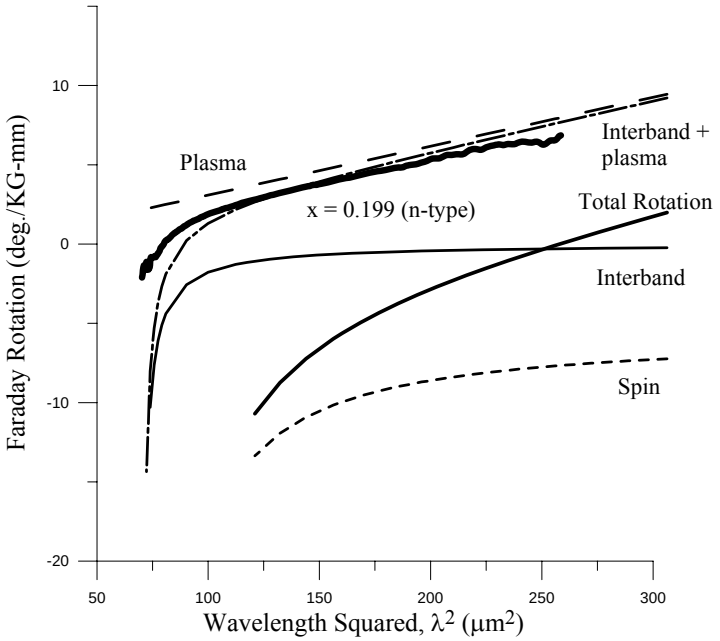


Fig. 42. Theoretical calculation of Faraday rotation components vs. wavelength squared in an n-type sample of $Hg_{1-x}Cd_xTe$, for x = 0.199 at 296 K. The bold line is the experimental result.

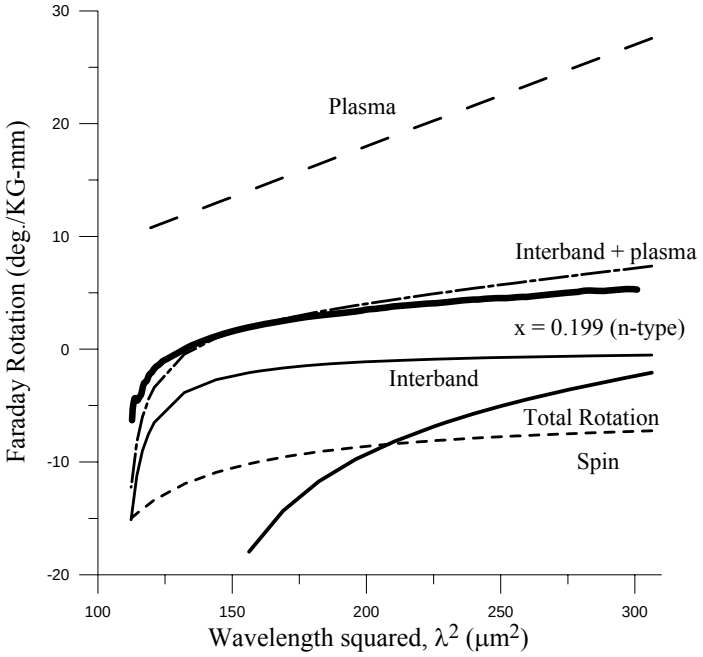


Fig. 43. Theoretical calculation of Faraday rotation components in the n-type, x = 0.199 sample at 190 K. The bold line is the experimental result.

Figures 42 and 43 show Faraday rotation components for an $Hg_{1-x}Cd_xTe$ sample with x = 0.199 at 296 K and at 190 K plotted against wavelength squared. With the decrease in bandgap with temperature, 190 K is the lowest temperature where rotation measurements with the FTIR can be made for this sample. The experimental results for the two temperatures look similar. The experimental curve follows the combined interband/plasma curve more than the total rotation curve. Figures 44-46 show the same general trend seen in the Faraday rotation versus temperature plots. As the bandgap gets larger for higher x samples and the InSb sample in figure 47, the FTIR wavelengths move further from resonance and the total, interband, and combined interband/plasma curves more closely match the experimental results but not entirely. The spin component seems always inconsistent with observed results. In figure 47 the experimental results show a decrease in slope and the curve crosses and drops below the calculated total rotation curve. This is due to distortion of the polarizer at higher rotations that will be discussed further in the InSb section.

Figures 48 and 49 are plots of Faraday rotation versus Cd mole fraction, x, at 10.6 microns at 296 K and 190 K. The two plots, again, show experimental results following the combined interband/plasma curves fairly closely.

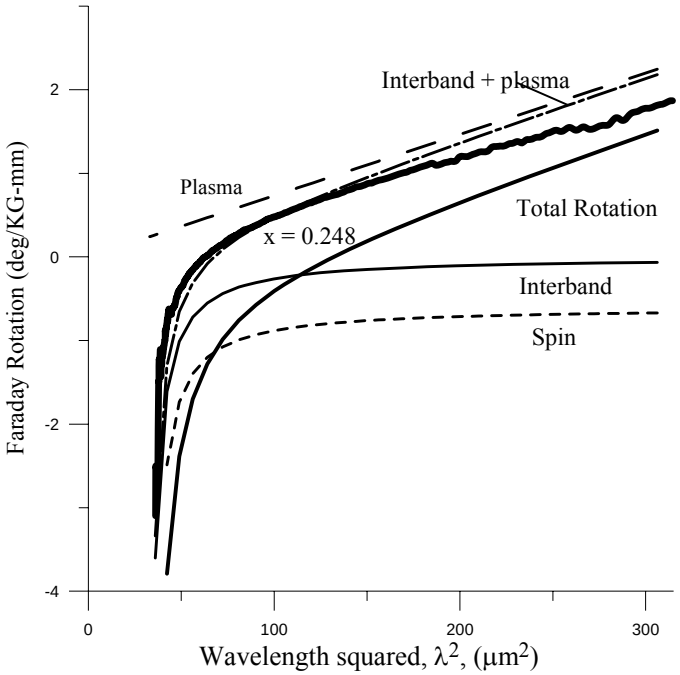


Fig. 44. Theoretical calculation of Faraday rotation components vs. wavelength squared in $Hg_{1-x}Cd_xTe$, x = 0.248, at 296 K. The bold line is the experimental result.

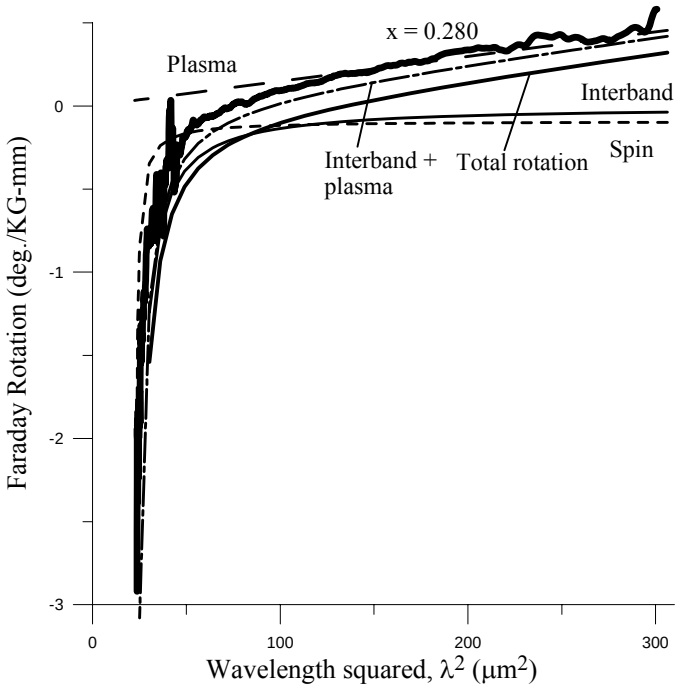


Fig. 45. Theoretical calculation of Faraday rotation components vs. wavelength squared in $Hg_{1-x}Cd_xTe$, x = 0.280, at 296 K. The bold line is the experimental result.

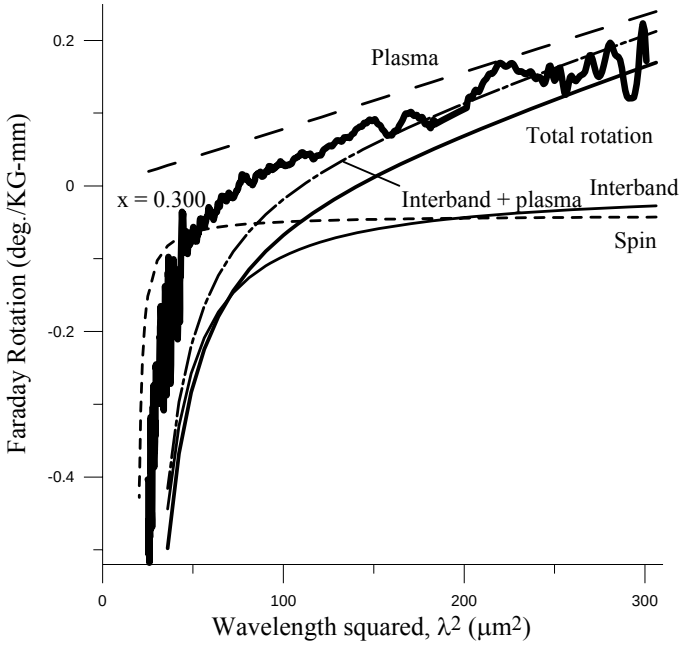


Fig. 46. Theoretical calculation of Faraday rotation components vs. wavelength in $Hg_{1-x}Cd_xTe$, x = 0.300, at 296 K. The bold solid curve is the experimental result.

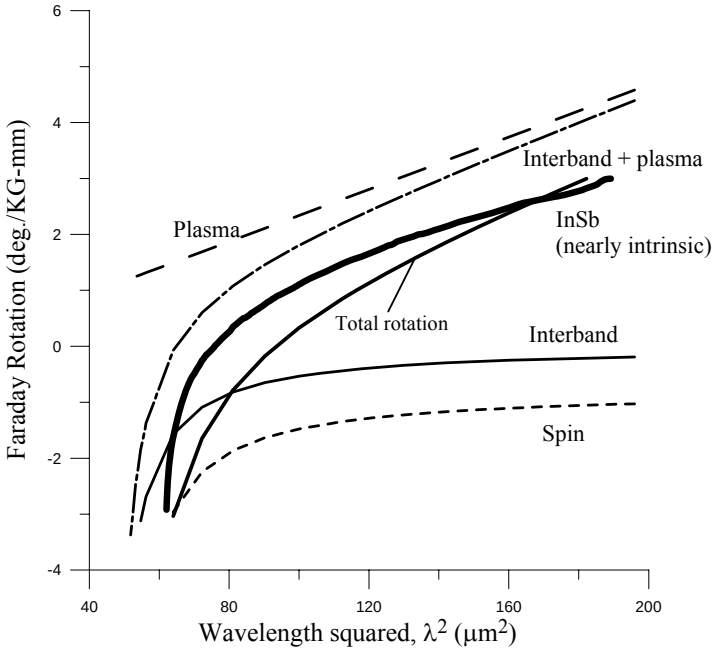


Fig. 47. Theoretical calculation of Faraday rotation components vs. wavelength in InSb at 296 K. The bold solid curve is the experimental result.

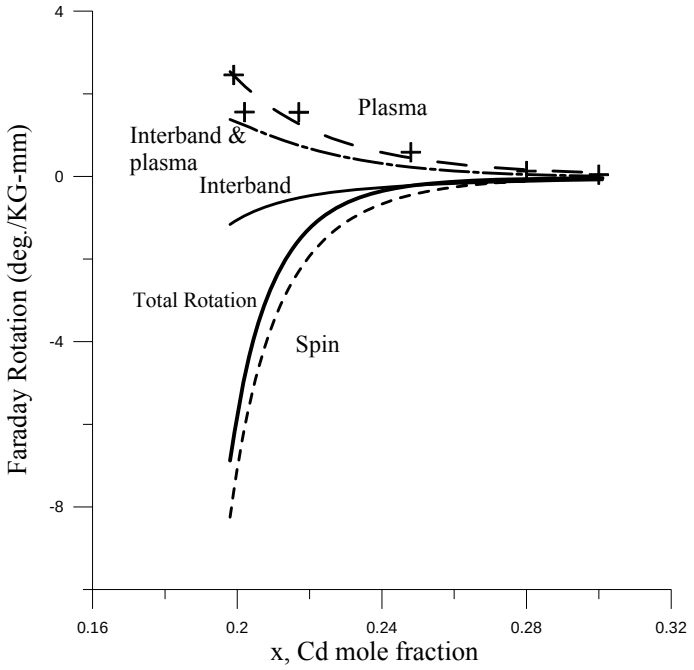


Fig. 48. Theoretical calculation of Faraday rotation components in $Hg_{1-x}Cd_xTe$, at 296 K and 10.6 μm. Symbols represent experimental values.

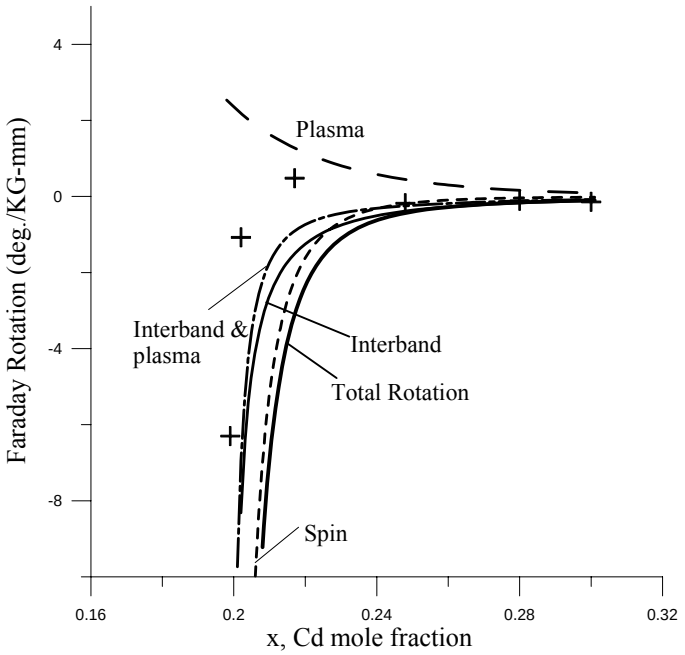


Fig. 49. Theoretical calculation of Faraday rotation components in $Hg_{1-x}Cd_xTe$, at 190 K and 10.6 μm. Symbols represent experimental values. The experimental value at x = 0.217 shows an exaggerated plasma component because it is slightly n-type.

## Conclusions

Aggarwal et al's [206] theory correctly predicts their experimental results. This includes the spin, interband, and plasma components. The model is less successful in predicting Yuen's [203] results. The model predicts an interband component a little larger than the spin component with a relatively insignificant plasma component at 2K. The interband component is linear with magnetic field, B, and gives the total rotation curves their tilt. This component is unavoidable in the model and totally absent in Yuen's results. His experimental rotation vs. B curves are flat. At higher temperatures and further from resonance, the spin component of the model is not consistent with the experimental results. In figures 36-38 the spin component increases with temperature, according to the model, where it should be decreasing, especially in figure 38, where the bandgap of InSb increases with temperature. This is because the carrier concentration, N, is increasing with temperature. Obviously, the model needs reformulation, at least, with regard to the spin component at higher temperatures.

As seen from the figures and in Eq (48) and Eq (49) the shapes of the curves and the resonance dependencies of the interband and spin components are very similar. There is no practical method to separate them i.e. by wavelength dependence. The original interest in this model [204(7*)] was to predict the behavior of the spin component to, perhaps, use this huge effect to screen carrier concentration in HgCdTe wafers at more convenient temperatures such as 296 K. There is another possibility to, perhaps, use this effect. In terms of the model, it amounts to the same thing to approach resonance at a particular wavelength by lowering the temperature and decreasing the bandgap to match the energy of the light, or to decrease the wavelength, to approach resonance at any particular temperature. Very close to resonance the spin component far surpasses the interband component according to the model. So it would appear that separation of these two components may not be necessary where say 95% or better of the observed rotation is spin component. Since spin is linearly dependant on carrier concentration, N, it might appear this could be an easy method for measuring carrier concentration. However, for x = 0.200 and Eg =0.153 eV, the wavelength range over which this occurs is $\Delta\lambda < 14$ nm. To use this, x and Eg would have to be known very precisely to less than $\Delta x = \pm 0.00019$ to be able to use the spin component equation, Eq. (49), to determine N. Eg and x are measured using cut-on wavelength, $\lambda_{co}$. The empirical equations such as, Eq. (30) relating bandgap energy to x, are not that accurate. Also, this very narrow wavelength range would require very accurate tuning of the light source which is probably not practical. In the case of x = 0.200, the spin component ranges

from -1.66 x $10^6$ deg/KG-mm to -850 deg/KG-mm over $\Delta\lambda$ = 14 nm according to the model. The interband component ranges from -2.50 x $10^3$ deg/KG-mm to -51 deg/KG-mm over the same range, so is relatively insignificant. The point is, that the spin component drops or rises so fast (that of an infinite singularity) with wavelength (or uncertainty in x determination) that the carrier concentration, only a linear factor, is lost in the magnitude of this change and cannot be determined with any accuracy, i.e. the spin component could change four orders of magnitude in these small changes of x or wavelength. The wavelength range or allowed uncertainty in x narrows with increasing bandgap, so the x = 0.200 case is the best case in the $0.200 < x < 0.300$ range. The upshot is, that this huge effect that is linear with carrier concentration is probably impractical to use to measure carrier concentration. A quantum mechanical model of the three components is presented in [348]. The authors show accurate theoretical prediction of their experimental results at 9 K. This model appears much more advanced than the model in [206, 204(7*)] but it needs testing at higher temperatures.

The best method for measuring carrier concentration using Faraday rotation is at room temperature where the plasma component is maximized, the interband and spin components are minimized, and the Moss-Burstein effect in n-type samples is minimized or not a factor.

## B. InSb

Figure 50 [202(6*), 318(9*)] shows a plot of free carrier rotation normalized to thickness, magnetic field, and effective mass ratios [15], and refractive indexes, n, [13, 156, 353] taken from the literature and contained in table VII. The main purpose of this plot was to compare experimental rotation measurements with the literature. The rotation measurements were obtained using the infrared polarimeter in figure 5 and the linear plot method at $CO_2$ wavelengths described in Section (A) of Experimental Methods and Samples. The refractive indexes for the more heavily doped samples were calculated using Eq. (3) with k = 0. Carrier concentrations were determined using the cold contact Hall technique for those samples contained in table IV and manufacturer's Hall tests for the others. The solid line in the figure is a regression plot fitted to the data. The slope is $1.25 \times 10^{-19}$ which is within 2% of the theoretical $1.22 \times 10^{-19}$ predicted by Eq. (13) for 9 μm light. In heavily doped samples, the plasma rotation was very large. The interband rotation was small in comparison and was considered negligible in heavily doped samples. Free carrier

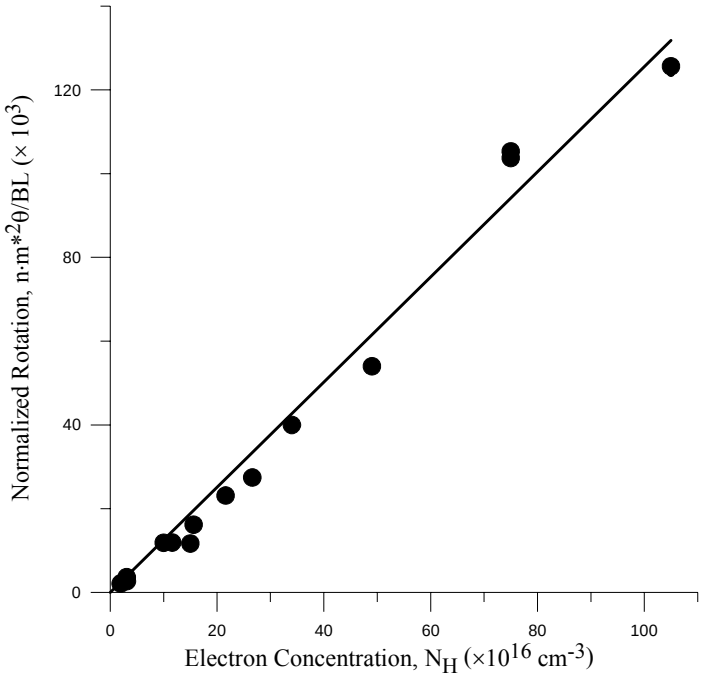


Fig. 50. Normalized electron Faraday rotation in n-InSb in deg/mm for B = 0.1 T at 9 μm, using literature values for refractive index, n, and effective mass ratio, m*, vs. electron concentration. The solid line is a least-squares fit to the data.

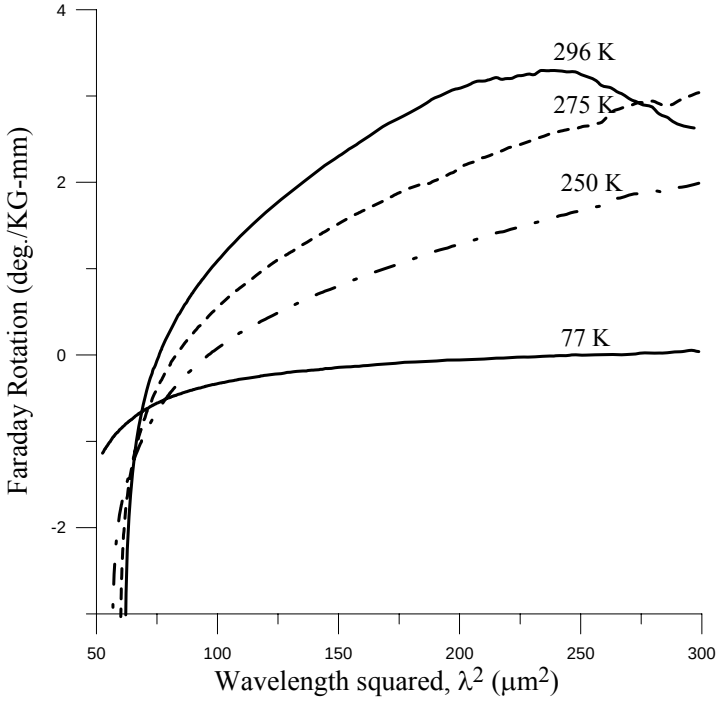


Fig. 51. Faraday rotation spectra of nearly intrinsic InSb at various temperatures.

rotation in samples doped above $30 \times 10^{16}$ $cm^{-3}$ was determined at a single wavelength, 10.6 μm, skipping the separation of components using the linear plot. The rotation at 9 μm was calculated using the relationship, $\theta = b\lambda^2$ in Eq. (27).

Figure 51 shows rotation spectra of a lightly doped InSb sample at several temperatures [200(2*), 201(3*), 322(8*)]. The drop in the 296 K curve on the right side of the figure is due to the polarizer and the analyzer. The drop off occurs as the sum of the rotation and the bias angle approaches extinction at 90 degrees. The rotation in the figure is normalized to a magnetic field strength of one kilogauss (KG) but the actual field strength used was 12.4 KG. The distortion is well established at 3 deg/KG-mm in the figure. This corresponds to an actual rotation of 3 deg/KG-mm ×12.4 KG-mm = 37.2 degrees. The bias angle was 40 degrees, yielding a sum of 77.2 degrees. As the rotation angle continues to increase beyond this point, so does the distortion. The distortion can also be seen in figure 29 for HgCdTe above 6 degrees in the x = 0.199 n-type sample. The bias angle was the same as in figure 51 but the HgCdTe samples were about half the thickness of the InSb sample so figure 29, showing rotation normalized to thickness, shows drop off due to the analyzer at 6 deg. rather than at 3 deg. The slopes were taken in the linear undistorted portions of the figure. In figure 51 the slope was taken between 125-180 $\lambda^2$. The FTIR resolution was 4 $cm^{-1}$, which results in about 37 points over this portion of the spectrum. This technique solves the problem of separating rotation components. The accuracy is limited by the strength of the magnetic field, the light source intensity, distortion due to the polarizer and analyzer, spectrum noise, resolution of the spectrum, and the length of the linear portion of the spectrum. Generally, the slopes can be determined using a computer with an accuracy of about ± 5%, which results in a ± 5% accuracy in determination of carrier concentration or, alternatively, an effective mass determination accuracy of ± 2%-3%.

Figure 52 shows a plot of absorption at 9 μm versus dopant concentration ($N_A$ - $N_D$), [202(6*)] where $N_A$ is the accepter and $N_D$ is the donor concentration, in n and p-type InSb. Absorption was calculated from transmission measurements which were compensated for multiple internal reflections due to the near parallel surfaces of the samples using the following equations [354] and Eq. (5);

$$T = \frac{(1 - R)^2 e^{-\alpha L}}{1 - R^2 e^{-2\alpha L}} \quad ,$$

$$K = \frac{1}{L} \ln \left[ \frac{2TR^2}{\left[ (1-R)^4 + 4T^2R^2 \right]^{\frac{1}{2}} - (1-R)^2} \right] \tag{51}$$

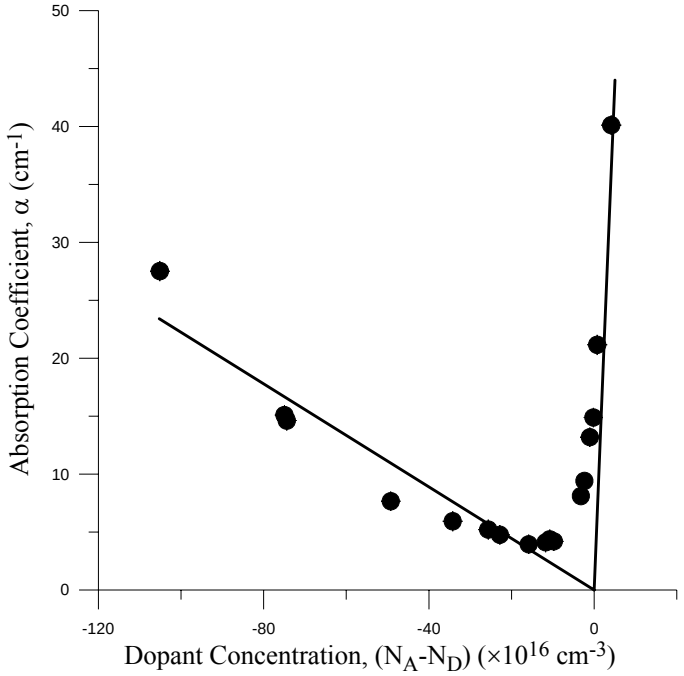


Fig. 52. Free carrier absorption vs. dopant concentration in n-type (negative $N_A$-$N_D$ values) and p-type (positive $N_A$-$N_D$) InSb at 9 μm and 296 K. The straight lines are regression plots through the n-type points and the p-type points and the origin. The slopes give the cross sections of the electrons and holes, respectively.

where T is the transmission and R is the reflectivity, and the second equation is the inversion of the first equation. Measurements were made at 9 μm to be able to compare results directly with the literature [118]. Tangents to the sample curves drawn through the origin on the left (n-type) and the right (p-type) sides of the plot have slopes of $0.22 \times 10^{-16}$ cm$^2$ and $8.8 \times 10^{-16}$ cm$^2$. These are the free electron ($\sigma_n$) and hole ($\sigma_p$) cross sections respectively. They are in good agreement with Kurnick and Powell's [118] $\sigma_n = 0.23 \times 10^{-16}$ cm$^2$ and $\sigma_p = 8.9 \times 10^{-16}$ cm$^2$.

Mobilities for samples in table VII as measured by Hall tests and using a ratio of Faraday rotation/absorption are shown in figure 53. The crosses in the figure represent manufacturer's Hall tests. The circles are experimentally measured Faraday rotation/

absorption measurements except for $N_H \leq 20 \times 10^{16}$ cm$^{-3}$ where the electron cross section was used to calculate absorption. $N_H \leq 20 \times 10^{16}$ cm$^{-3}$ was chosen as the break point between calculated and measured absorption based on the fit achieved between experimental and Hall test data. The open triangles represent Hall tests using the cold contact technique. The solid curve is a mobility calculated from the ratio of free electron Faraday rotation (θ)/free electron absorption (α) in Eq. (11). Faraday rotation at 9 μm was calculated using $N_H$ from the cold contact technique (tables IV and VII), m*, from figure 54, and refractive index, n, from table VII. Electron absorption at 9μm was calculated using $\alpha = N_H\sigma_n$, where $\sigma_n$ is $0.22 \times 10^{-16}$ cm$^2$. The proportionality, "C", was set to C = 1. The manufacturer's Hall tests more closely match the θ/α experimental measurements. The cold contact technique mobilities are a bit lower. The calculated curve naturally follows the measured θ/α more closely, but overall, the match of Hall to θ/α mobilities measured or calculated is fairly good. The percentage difference between θ/α measurements and manufacturer's Hall tests

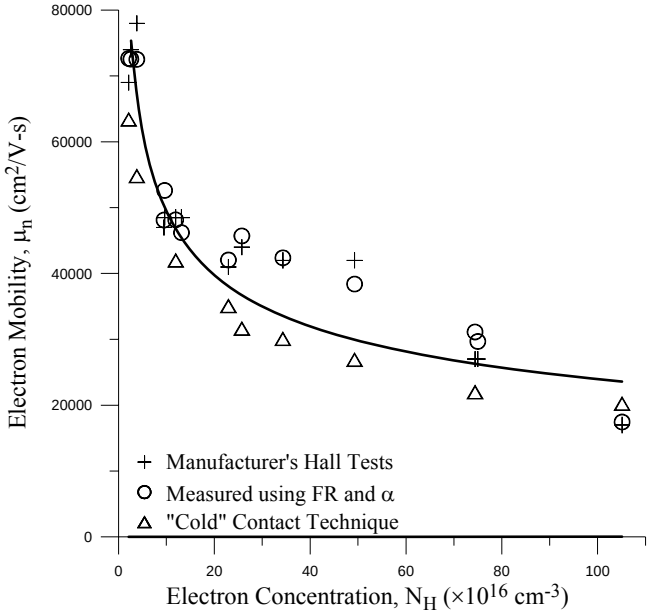


Fig. 53. Elecrton mobility in n-InSb. The circles are experimental θ/α data, except for $N_H \leq 20 \times 10^{16}$ cm$^{-3}$ where α was calculated using an absorption cross section. The crosses are Hall tests. The solid curve is mobility from Eq. (11) using Faraday rotation calculated from effective masses in fig. 54, absorption calculated using $\alpha = N\sigma_n$, and C = 1.

ranges from -15 to +7% averaging -2% and the differences between θ/α measurements and cold contact Hall tests range from +25 to +2% averaging +14%.

InSb has an intrinsic carrier concentration of $1.6 \times 10^{16}$ cm$^{-3}$ at 296 K [13]. The ratio of hole absorption to electron absorption is on the order of 40 to 1 at 296 K and 200 to 1 at 77 K [118]. So for lightly doped InSb, an absorption cross section must be used to calculate free carrier absorption. For samples with $N_H$ below $20 \times 10^{16}$ cm$^{-3}$ the electron absorption cross section was used to calculate absorption used in the $\theta/\alpha$ ratio. Actual experimentally measured absorptions were used for $N_H \geq 20 \times 10^{16}$ cm$^{-3}$. These samples are shown as open

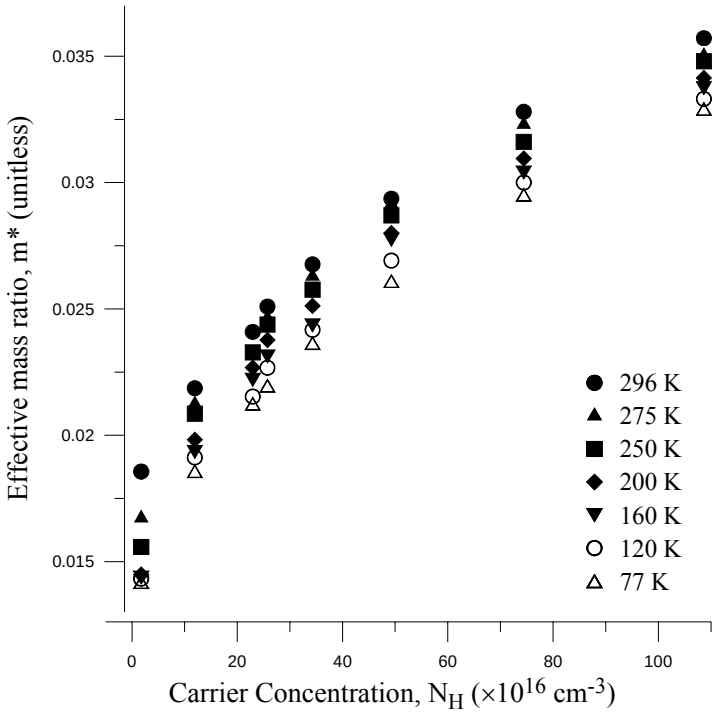


Fig. 54. Effective mass ratio, m*, in n-InSb at several temperatures.

circles in figure 53. Hall tests are shown as crosses in the figure. Figure 54 shows effective mass ratios , m*, as determined from the slopes of Faraday rotation spectra using the FTIR method described previously and in section (B) of Experimental Methods and Samples [200(2*), 201(3*), 322(8*)]. Effective mass ratios of semiconductors as a function of carrier concentration and temperature are rare in the literature. Those shown in figure 54 agree fairly well with effective masses at 296 K reported in [156] and those compiled from many sources in [15] and contained in table VII. Figure 55 shows the mobility proportionality, "C", from Eq. (11) at 9 μm plotted for various dopant concentrations versus temperature. The Hall electron concentration using the cold contact technique of each

sample at room temperature are labeled in the figure. "C" is normalized to B and L and was calculated using:

$$C = \mu_n \alpha / \theta_n \tag{52}$$

Where the electron mobility, $\mu_n$, was determined using the cold contact technique. The free electron absorption, $\alpha$, was calculated using the electron absorption cross section in the $N_H$ = 2 and 4 $\times 10^{16}$ $cm^{-3}$ at all temperatures. According to Kurnick and Powell [118], the electron cross section at 77 K is 0.114 $\times$ $10^{-16}$ $cm^2$ at 9 μm. In calculating absorption for these samples for temperatures between 77 K and 296 K, the cross section was assumed to increase linearly with temperature to 0.22 $\times 10^{-16}$ $cm^2$ at 296 K. The cross sections were also used in the $N_H = 12 \times 10^{16}$ $cm^{-3}$ sample for temperatures above 160 K. From Hall data on the nearly intrinsic sample, the intrinsic carrier concentration drops two orders of magnitude at 160 K and below and was considered insignificant compared to the dopant concentration. The Faraday rotation in Eq. (52) was calculated using $N_H$ from the cold contact technique Hall tests, and m* from the data of figure 54. The refractive index, n, was calculated using $n_o$ = 3.96 [13] in Eq. (3). Eq. (3) does not explicitly account for temperature dependence of the refractive index, except through the temperature dependence of N and m*. Figure 55 appears a bit strange. As seen in the figure, "C" at 296 K is close to 1 for all samples. It is a bit low due to lower mobilities for the cold contact technique compared in figure 53. The values for "C" initially drop significantly in the figure from "C" for the nearly intrinsic sample to the $N_H = 4 \times 10^{16}$ $cm^{-3}$ sample down to the $N_H = 12 \times 10^{16}$ $cm^{-3}$ and $N_H = 23 \times 10^{16}$ $cm^{-3}$ samples. This is due to the large initial decrease in mobility of these samples as carriers are added. As more carriers are added, the drop in mobility decelerates and begins to level off at $N_H \approx$ 20-30 $\times 10^{16}$ $cm^{-3}$ as seen in figure 55. At $N_H = 34 \times 10^{16}$ $cm^{-3}$, the absorption begins to dominate Eq. (52) and "C" rises. This continues up to the $N_H$ = 109 $\times 10^{16}$ $cm^{-3}$ sample.

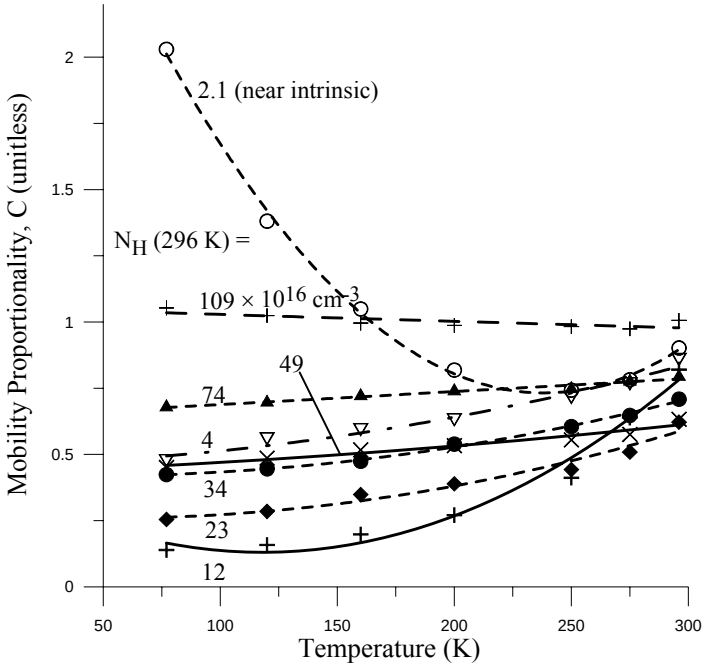


Fig. 55. Mobility proportionality "C" normalized to magnetic field and sample thickness in Eq. (11) in n-InSb at 9 μm. The free electron absorption was calculated for lightly doped samples where hole absorption dominates. The lines are for clarity to bring out the set of points for each sample.

## Table VII. InSb Sample Data at 296 K.

| Sample # | $N_H$† ($\times 10^{16}$ cm$^{-3}$) | $N_H$* ($\times 10^{16}$ cm$^{-3}$) | $\mu_H$† (× 1000 cm$^2$/V-s) | $\mu_H$* (× 1000 cm$^2$/V-s) | α ( cm$^{-1}$ at 9 μm) | m*[a] | n[b] |
|---|---|---|---|---|---|---|---|
| I 1 | 1.95 | 2.11 | 69 | 63.4 | 13.19 | 0.021 | 3.953 |
| I 2 | 3.1 | ----- | 74 | ----- | 9.41 | 0.021 | 3.949 |
| I 3 | 3.06 | 3.76 | 78 | 54.8 | 8.11 | 0.021 | 3.949 |
| I 4 | 10 | ----- | 45-52 | ----- | 4.2 | 0.035 | 3.949 |
| I 5 | 15 | ----- | 47 | ----- | 4.37 | 0.035 | 3.949 |
| I 6 | 10-15 | 11.93 | 41 | 35.07 | 4.1 | 0.035 | 3.949 |
| I 7 | 10 | ----- | 45-52 | ----- | 3.94 | 0.035 | 3.925 |
| I 8 | 21.6-23.6 | 22.94 | 41 | 35.07 | 4.76 | 0.035 | 3.892 |
| I 9 | 25.6-27.6 | 25.74 | 44 | 31.63 | 5.21 | 0.035 | 3.884 |
| I 10 | 31.6-36.6 | 34.31 | 42 | 30.07 | 5.93 | 0.035 | 3.856 |
| I 11 | 47.6-50.6 | 49.28 | 42 | 26.91 | 7.66 | 0.035 | 3.811 |
| I 12 | 62.6-86.6 | 74.43 | 27 | 21.98 | 14.62 | 0.035 | 3.734 |
| I 13 | 62.6-86.6 | ----- | 27 | ----- | 15.1 | 0.035 | 3.734 |
| I 14 | 110-190 | 105.13-108.64 | 17 | 20.24 | 27.52 | 0.035 | 3.637 |
| I 15 (p-type) | 0.57-0.77 (holes) | ----- | ----- | ----- | 14.89 | ----- | 3.96 |
| I 16 (p-type) | 1.8-1.9 (holes) | ----- | ----- | ----- | 21.16 | ----- | 3.96 |
| I 17 (p-type) | 4.2-4.6 (holes) | ----- | ----- | ----- | 40.12 | ----- | 3.949 |

† Data provided by the manufacturer. * Hall tests using "cold" indium contact technique [199(1*), 200(2*), 201(3*)].
a. Taken from ref [15]. b. Refractive index at 9 μm taken from ref [13, 156, 353] and calculated from Eq. (3).

## C. GaAs

The bandgap in GaAs is 1.42 eV. Interband rotation at $CO_2$ laser wavelengths is insignificant and separation of components is not necessary. Free electron rotation measurements were made with the $CO_2$ laser apparatus directly at a single wavelength, 10.6 μm, and calculated at 9 μm. A plot of the normalized rotation at 9 μm verses Hall concentration is shown in figure 56 [202(6*), 318(9*)]. The refractive index in the dopant range 3-20 × $10^{17}$ $cm^{-3}$ was taken from [13] as 3.317. The effective mass ratios were taken from Constantinescu et al. [228]. The plot shows some scatter due to the variability of the manufacturer's Hall tests described previously. The solid line is a regression plot fitted to the data. The slope is 1.19 × $10^{-19}$ which is about 2% off from the theoretical 1.22 × $10^{-19}$ predicted by Eq. (13) for 9 μm light.

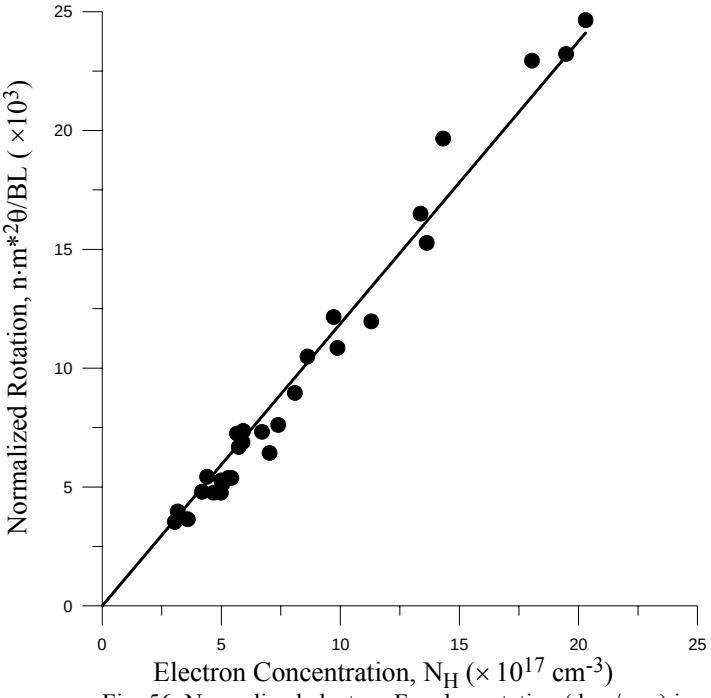


Fig. 56. Normalized electron Faraday rotation (deg./mm) in n-GaAs for B = 0.1 T at 9 μm and 296 K. The solid line is a least squares plot to the data.

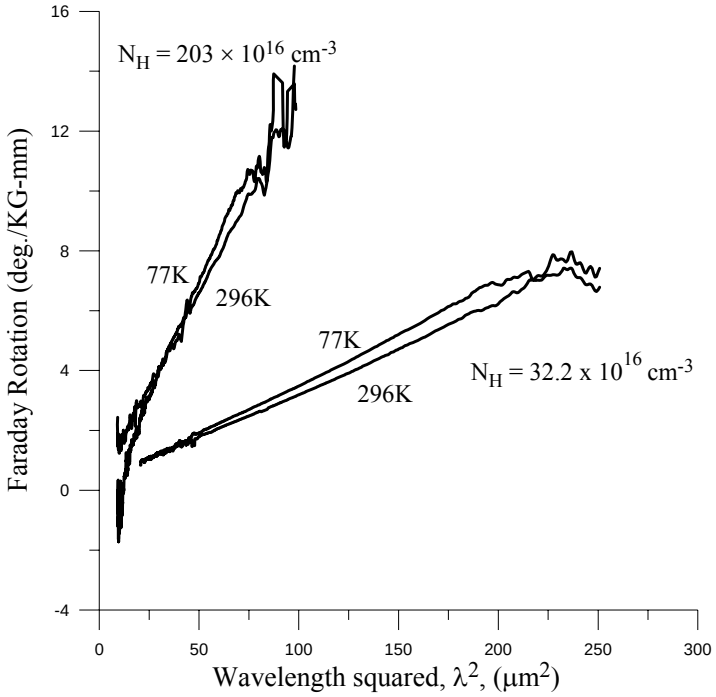


Fig. 57. Faraday rotation spectra of n-type GaAs at 296 K and 77 K.

Figure 57 shows Faraday rotation spectra [200(2*), 201(3*), 322(8*)] for two n-GaAs samples, G4 and G21, in table V. The spectra are flat throughout the wavelength range of the plot as expected for the comparatively large bandgap. Alfano and Baird [224] showed that the positive offset that can be seen by extrapolating the spectra to zero in the figure is due to multiple internal reflection (MIR). Since only the slope of the spectra is used, the determination of N or m* using this method would appear to be unaffected. MIR is examined and discussed later. Figure 58 shows effective mass ratios measured using the FTIR Faraday rotation spectra slope method [200(2*), 201(3*), 322(8*)]. The solid curve represents room temperature effective masses from ref [228]. Again the ± 2-3% scatter between the measurements and the reference curve is due to the estimated ± 10% variability in the Hall tests.

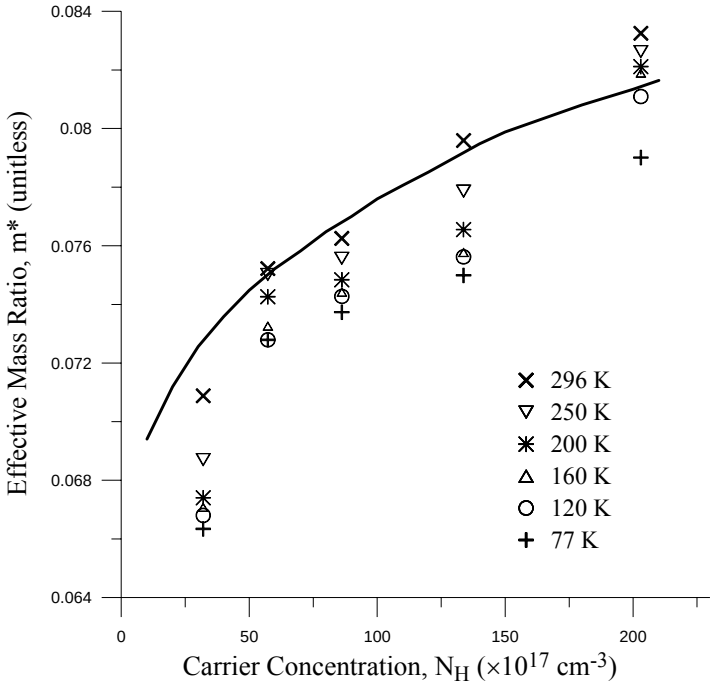


Fig. 58. Effective mass ratio, m*, in n-GaAs vs. carrier concentration at several temperatures. The solid curve is a reference curve taken from ref. [228] for m* at 296 K. The approximate 2-3% scatter is partially due to the ± 10% variation in the Hall tests.

Figure 59 shows absorption measured in these n-GaAs samples at 9 μm [202(6*)]. Also plotted in figure 59 are some points plotted from references [18, 99]. The lower absorption of the samples in the figure is presumed to be due to better quality of modern GaAs. Measured absorptions and rotations were used in figure 60 [202(6*)] to calculate mobilities according to Eq. (11) using C = 1. The crosses represent manufacturer's Hall tests and the open circles are θ/α measurements. The solid curve is a simple calculation of the ratio of Faraday rotation to absorption with C =1 in Eq. (11). Faraday rotation was calculated using the reference effective masses in [228], the refractive index above, and $N_H$ from the manufacturer's Hall tests in Eq. (13). Absorption for the curve was calculated using an average cross section estimated at three points along the polynomial in figure 59, and $\alpha = N_H\sigma_n$. The simple calculation and θ/α measurements are reasonable approximations to the Hall tests. The scatter in the figure is unavoidable due to the variability of the Hall tests. The mobility proportionality, "C", was calculated from Eq. (52) at 9 μm and 296 K for the five samples in table V. As shown in figure 61, the mobility proportionality appears linear with carrier concentration and close to one.

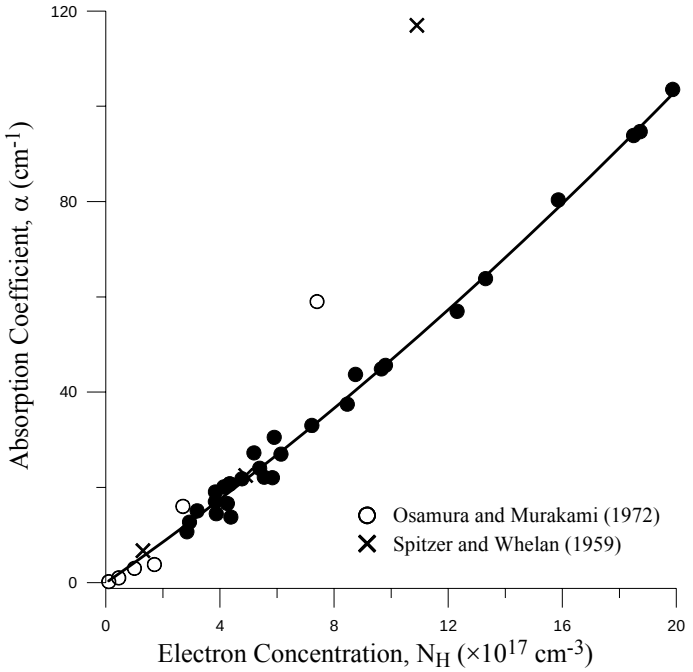


Fig. 59. Free electron absorption vs. electron concentration in n-GaAs at 9 μm and 296 K. Additional points are included from Spitzer et al. [18] and Osamura et al. [99] for comparison.

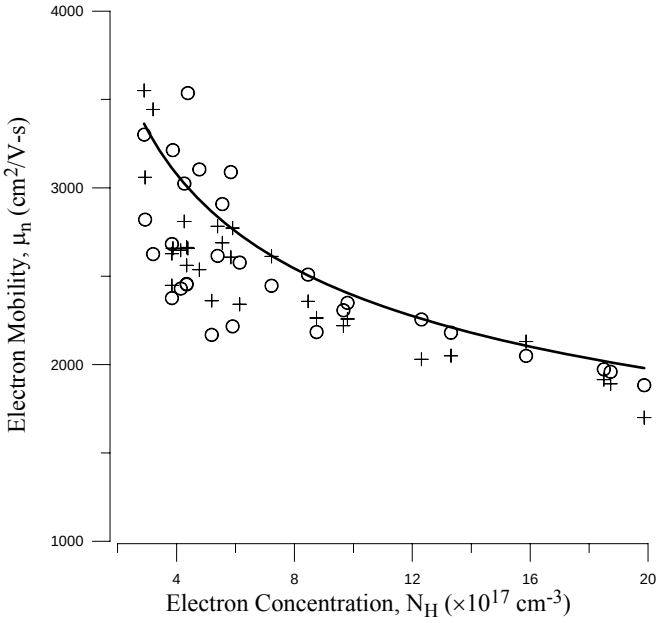


Fig. 60. Electron mobility in n-GaAs. The circles are experimental θ/α data. The crosses are Hall tests. The solid curve is mobility calculated using Eq. (11) with C = 1, using Faraday rotation calculated from effective mass ratios in [228] (fig. 58), and absorption calculated using $\alpha = N\sigma_n$, where $\sigma_n$ was estimated as ~ 4, 4.9, and 5.1 $\times 10^{-17}$ cm$^2$ along the polynomial absorption curve in fig. 59.

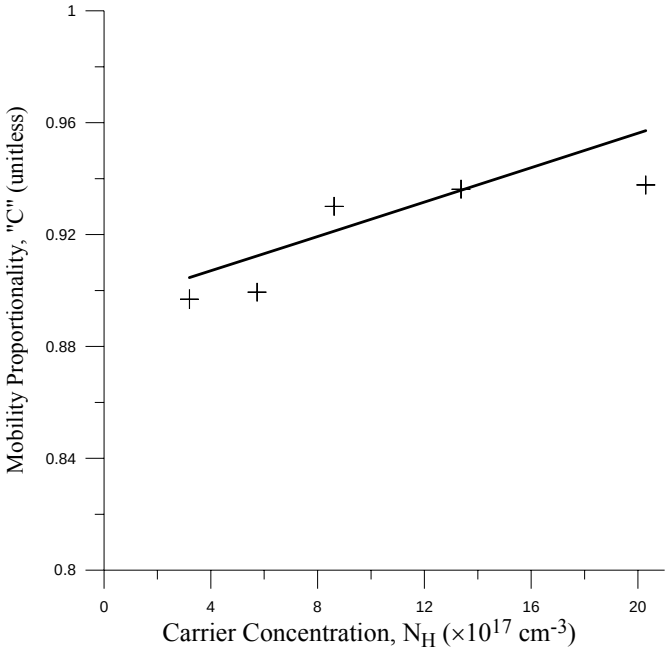


Fig. 61. Mobility Proportionality to ratio of free carrier Faraday rotation and absorption in Eq. (11), plotted against carrier concentration at 296 K and 9 μm.

## D. Si, Ge

Figure 62 shows free carrier absorption at 10.6 μm in n-type silicon at 296 K and 77 K. The carrier concentrations along the x-axis are those measured using the cold contact technique at room temperature. Spitzer and Fan's measurements [156] in three n-Si samples are plotted as a reference. Absorption in the samples (several representative samples are contained in table VI) at 77 K is close to that at room temperature, but carrier concentrations in these samples drop a factor of two to more than four according to the Hall test results in figure 24. This indicates that the free electron absorption cross sections increase significantly as temperature decreases. Figure 63 shows absorption at 10.6 μm versus temperature in an n-type Ge sample with $N_{296K} = 24.5 \times 10^{16}$ $cm^{-3}$. Absorption initially drops as temperature decreases from room temperature to 250 K then appears to essentially level out between 250 K and 77 K. Hall tests for this sample are shown in figures 9 and 10. In figure 10, carrier concentration drops by a factor of two between 296 K and 77 K indicating that free carrier absorption cross sections also increase significantly in Ge as temperature decreases. Figure 64 shows effective mass ratios in n-Si for six samples contained in table VI at various temperatures. The measurements were made using rotation

data from the FTIR method but the data was too noisy to use the slopes of the rotation spectra. The effective mass ratios in silicon and germanium are too large to obtain a strong rotation signal with the magnetic fields used. Consequently, the data shows a lot of scatter. Effective masses were calculated, summed and averaged, point by point using rotations in

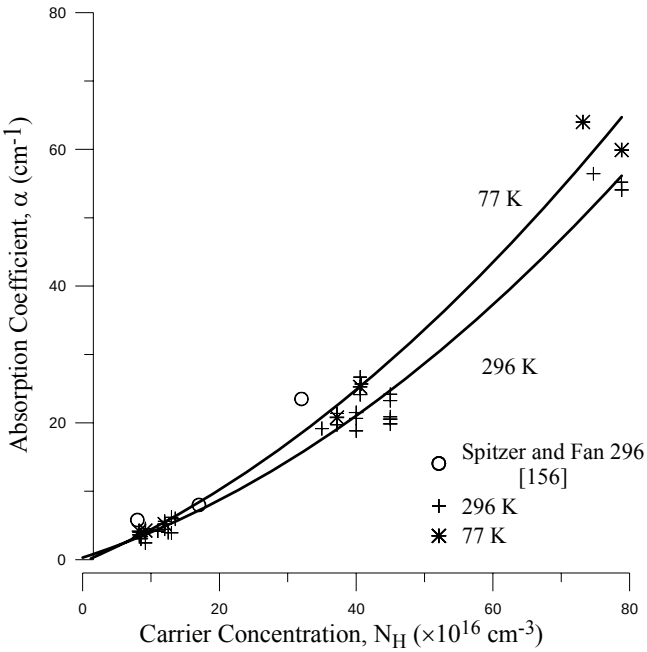


Fig. 62. Absorption in n-type silicon vs. room temperature carrier concentration at 10.6 microns. From figure 24, carrier concentrations drop a factor of 2 to more than 4 for these samples from 296 K to 77 K. The slight increase in the absorption curve at 77 K indicates the absorption cross-section increases significantly at 77 K.

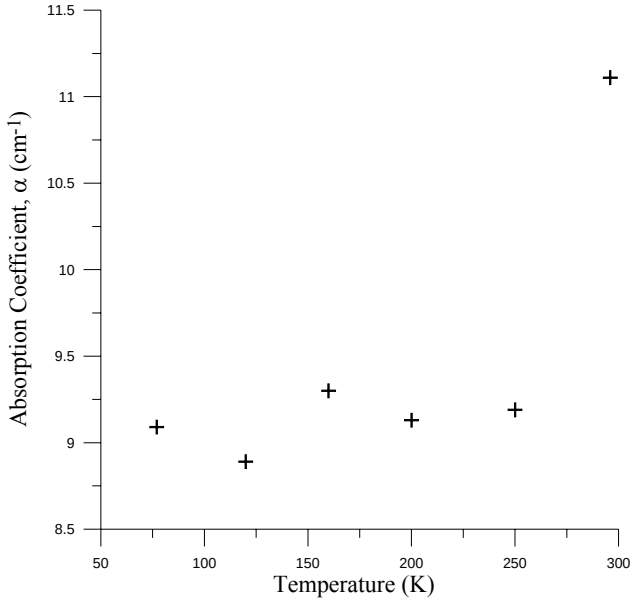


Fig. 63. Absorption in an n-type germanium ( $N_{296K} = 24.5 \times 10^{16}$ cm$^{-3}$) sample vs. temperature. The absorption drops initially and then virtually flattens out from 250 K to 77 K. From figure 12, carrier concentration drops to half between 296 K and 77 K. This indicates the absorption cross-section is increasing with decreasing temperature.

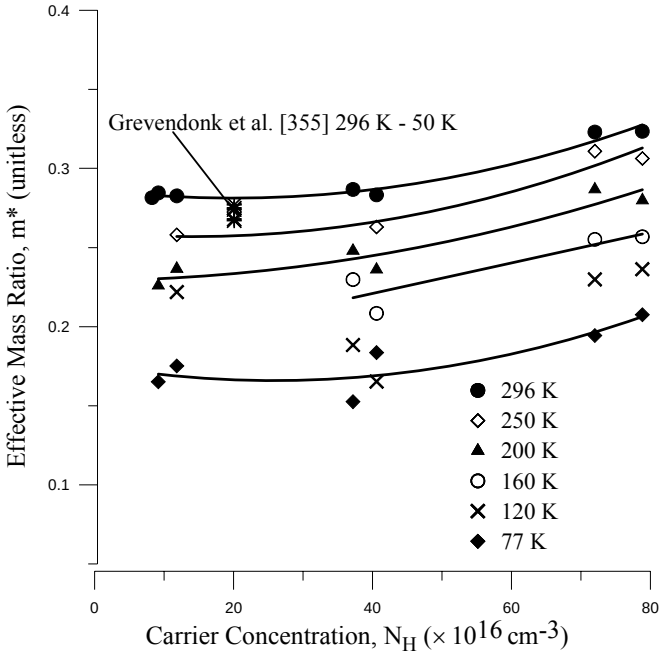


Fig. 64. Effective mass ratio in n-type silicon. N is the room temperature carrier concentration. The starred symbols in the upper left of the figure are effective mass ratios of a $N_{296K} = 20.1 \times 10^{16}$ cm$^{-3}$ sample between 296 K and 50 K from ref. [355].

relatively smooth, flat regions of the spectra, roughly between 10 and 15 μm. Grevendonk et al. [355] measured Faraday rotation in an n-Si sample, $N = 20.1 \times 10^{16}$ $cm^{-3}$ using an incoherent light source between 3-5μm at temperatures between 9-300 K. They used the linear plot model of Eq. (27). Using their determinations of "a", for interband, and "b", for free carrier rotations in Eq. (27), interband rotation in the sample is estimated to be about 2 % at 10.6 μm. Interband rotation in Si is positive [347] or of the same sign of the free carrier rotation, so effective mass calculations using raw rotations (no correction or separation of the interband components) would be expected to be slightly smaller by about $\sqrt{2}$ % or less in the 10 to 15 μm range. The square root appears because m* is squared in relation to rotation. The effective masses obtained by Grevendonk et al. between (296 K and 77 K) are plotted in the upper left part of figure 64. Their data shows very little change in effective mass in n-Si with temperature in contrast to results obtained here.

The bandgap in Si is reported as 1.143 eV [356-357]. In Ge it is 0.67 eV [356-357]. According to Roth [347], and using the Faraday rotation model presented earlier, specifically the interband rotation equation, Eq. (40), the interband rotation in Ge is estimated to be 3% at 10.6 μm. This is using light and heavy hole masses for Ge reported in [356], and measured values of, "f", and "$g_{eff}$" reported in Roth in the expression for "K" in Eq. (41). Interband rotation in Ge is negative [222, 347] or of opposite sign to free carrier rotation so, effective mass ratios calculated from raw rotation data between 10 and 15 μm would be expected to be slightly larger by $\sqrt{3}$ % or less. Effective mass ratios as a function of temperature for the Ge sample are shown in figure 65. The solid line is a linear fit to the data. The effective mass ratios in figures 64 and 65 have been corrected for multiple internal reflection (MIR) in the Si and Ge samples. This is covered in the next section. Figure 66 shows the proportionality, "C", from Eq. (11) between the ratio of free carrier Faraday rotation and absorption versus the room temperature carrier concentration at several temperatures. The proportionality was calculated using Eq. (52) using carrier concentration vs. temperature data in figure 24, absorption data in figure 62, mobility data in figure 23, and effective mass data in figure 64. Absorption at temperatures between 296 K and 77 K was assumed to be virtually constant ( see figure 62). The proportionality, "C", for the Ge sample is plotted in figure 67 using carrier concentration from figure 10, mobility from figure 9, absorption from figure 63, and effective masses from figure 65.

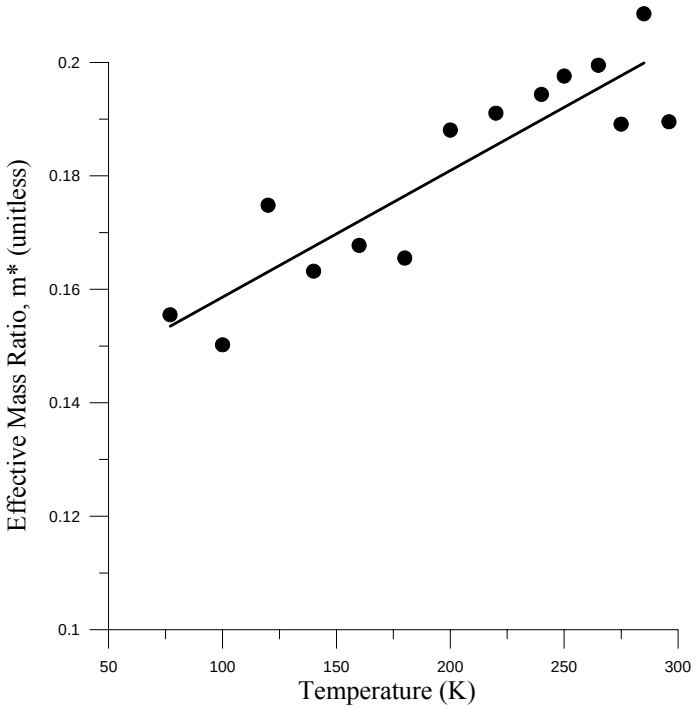


Fig. 65. Effective mass ratio in an n-type Ge sample, $N_{296K}$ = $24.5 \times 10^{16}$ $cm^{-3}$ vs. temperature. The solid line is a least squares plot to the data.

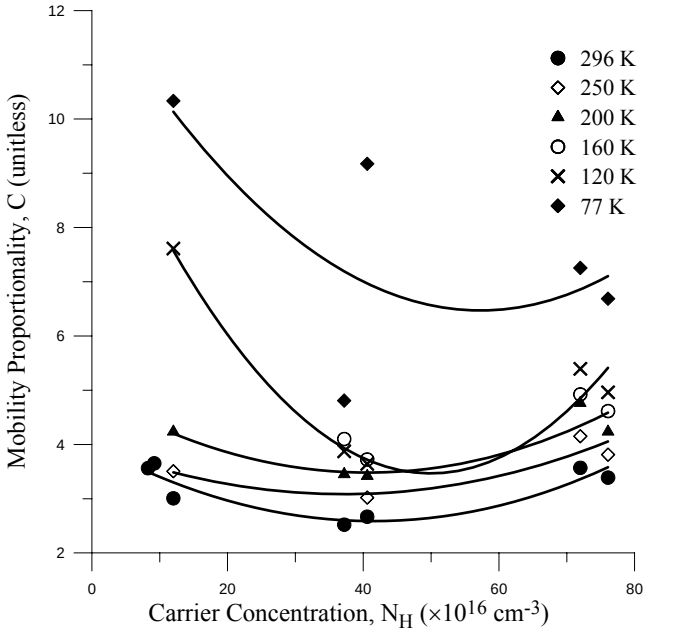


Fig. 66. Proportionality constant, C, between mobility and the ratio of free electron Faraday rotation and absorption in n-type silicon at 10.6 μm according to Eq. (11).

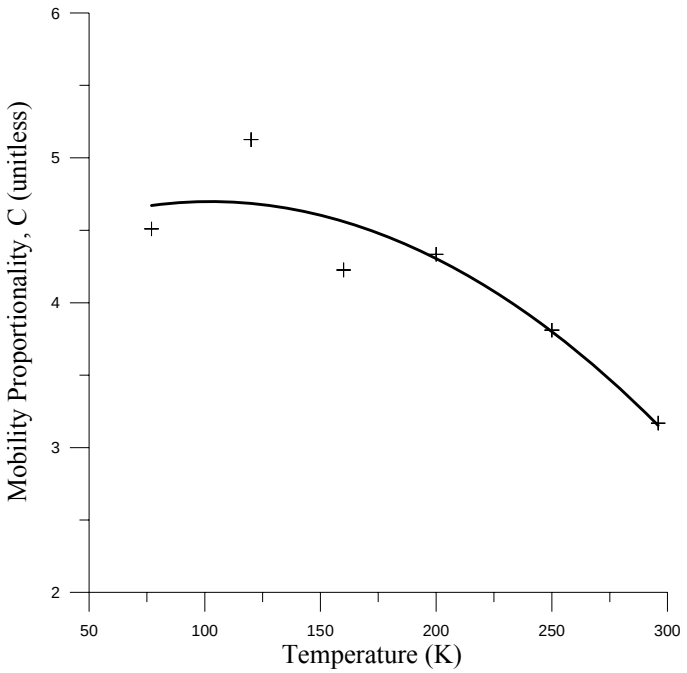


Fig. 67. Proportionality constant between mobility and the ratio of free electron Faraday rotation and absorption in n-type Ge according to Eq. (11). Carrier concentrations are measured at various temperatures (figure 10).

## E. Correction for MIR in Effective Mass Ratios

Correction for multiple internal reflection (MIR) in semiconductor Faraday rotation data was discussed in [217, 224-225]. The three references give simple correction formulas relating actual measurement angle, $\theta_m$, to true angle, $\theta$, as a function of absorption and reflection of the sample. The expressions in [217] and [224] give similar corrections. There appears to be an error in the expression given in [225]. Application of MIR corrections to Faraday rotation spectra for n-GaAs in [224-225] yield corrected spectra a few percent lower in rotation that closely follow the shape of the original spectra. In the linear portion of the spectra above about 5 microns the slopes of the corrected and uncorrected spectra appear virtually identical. The MIR correction given in [217] is:

$$\theta = \theta_m \frac{1 - R^2 e^{-2\alpha L}}{1 + R^2 e^{-2\alpha L}} \tag{53}$$

Samples with the lowest absorption and largest rotation require the largest percentage correction. Figures 68-70 show Eq. (53) applied to Faraday rotation spectra of two HgCdTe samples plotted earlier in figure 29. They are extreme examples among the HgCdTe samples. The x = 0.199 sample has relatively large rotation but has low absorption because it is n-type and consequently has fewer holes. Holes absorb roughly 4 to 1 over electrons in HgCdTe. Absorption versus wavelength was calculated for the two samples using the wavelength dependent absorption cross sections for holes, $\sigma_p$, and electrons $\sigma_n$, given earlier from [129] as $\sigma_p = 3.17 \times 10^{-18} \lambda^2$ cm$^2$ and = $\sigma_n = 3.17 \times 10^{-19} \lambda^{2.4}$ cm$^2$. Figure 69 shows a close up view of the linear portion of the x = 0.199 Faraday rotation spectrum. The corrected spectrum is lower by 9% with a slope that is lower by about 1%. Figure 70 shows a close up view of the linear portion of the x = 0.280 sample plot. This sample has low absorption due to a low intrinsic carrier concentration for x = 0.280 and low rotation. The corrected curve is lower in rotation by 7% and lower in slope by about 4%. The variability of these MIR corrected slopes for these extreme examples is within the experimental variability of 5% normally encountered in determining these slopes.

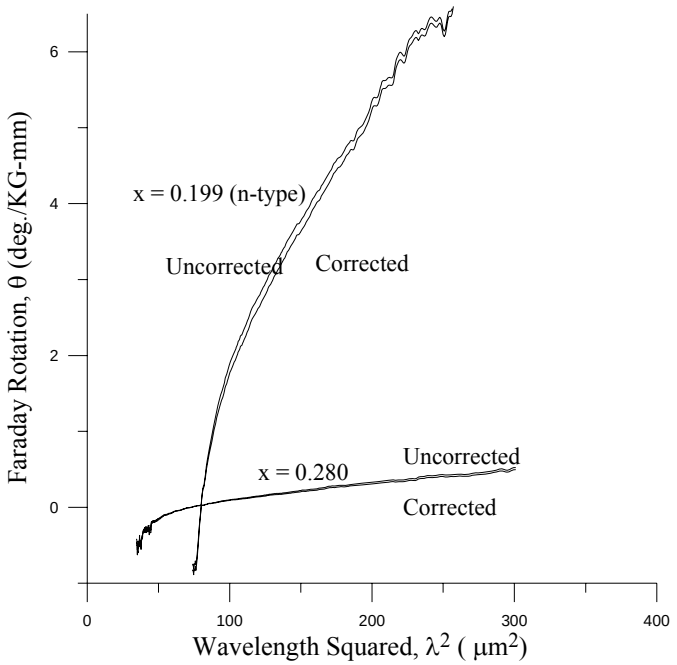


Fig. 68. Corrected rotation curves for multiple internal reflection (MIR) in two $Hg_{1-x}Cd_xTe$ samples with x = 0.199 and 0.280 samples previously plotted in figure 29. The top plot is an n-type sample with low absorption. The bottom plot for x = 0.280 has low carrier concentration, low absorption and low rotation, maximizing the needed MIR correction according to Eq. (53).


Fig. 69. Close up of the linear portion of the $Hg_{1-x}Cd_xTe$, x = 0.199 (n-type) sample shown in figure 68. The corrected curve is 9 % lower then the uncorrected curve with a 1% lower slope. This sample has low absorption due to low hole population, requiring increased MIR correction according to Eq. (53).

Given these results and the results in [217, 224], it appears that little or no MIR correction is required in determining the slopes of the spectra. Also, it appears that determining m* using the slope of the Faraday rotation spectrum is practically immune to the MIR effect. This applies to both the linear plot method using Eq. (27) and the FTIR method. The linear plot method is also a slope method. It uses $b\lambda^2$ from Eq. (27) to determine m* where b is the slope of the linear portion of the Faraday rotation vs. $\lambda^2$ plot. Any MIR encountered along with any residual interband rotation shows up in the intercept of the extended linear portion of the plot. This is another advantage using the slope of the Faraday rotation spectra rather than measurements at individual wavelengths. Si and Ge electrons have fairly large effective masses and give a weak, noisy signal at a magnetic field strength of 12.4 KG. Consequently, the slopes could not be determined with sufficient accuracy. Effective mass ratios for Si and Ge plotted in figures 64 and 65 were determined using measurements at individual wavelengths, summed and averaged over relatively flat portions of the spectra. These m* measurements were corrected for MIR using Eq. (53). As expected, the

correction for the higher doped samples with higher absorptions and rotations was negligible. Correction in m* measurements in lower doped samples, S7 ($N_{296K} = 9.18\times10^{16}$ $cm^{-3}$) and S8 ($N_{296K} = 11.83\times10^{16}$ $cm^{-3}$), was 5-6% between 77 K and 296 K. In the Ge sample ($N_{296K} = 24.5 \times10^{16}$ $cm^{-3}$) the MIR correction in the m* measurement was a consistent 6-7% between 77 K and 296 K.

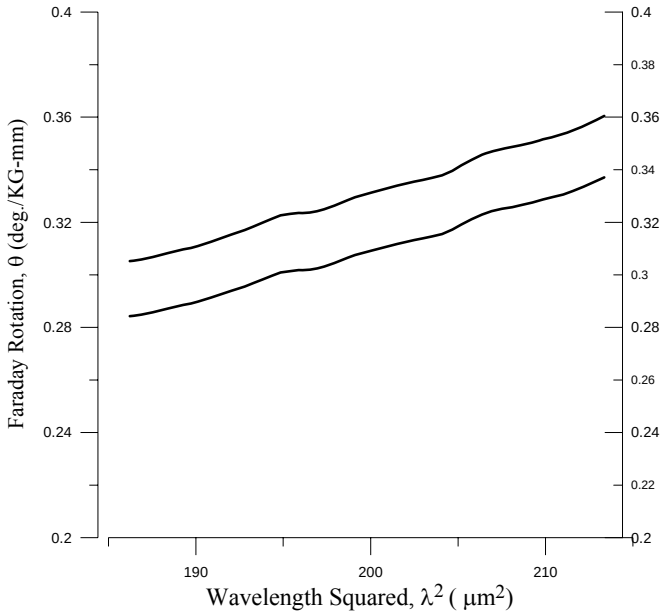


Fig. 70. Close up of the linear portion of the HgCdTe, x = 0.280 sample shown in figure 68. The corrected curve is 8 % lower then the uncorrected curve with a 4% lower slope. This sample has low rotation, low intrinsic carrier concentration, and free carrier absorption, maximizing MIR correction according to Eq. (53).

## SUMMARY and MAIN CONCLUSIONS

$Hg_{1-x}Cd_xTe$ was first synthesized in 1958 by British scientists at the Royal Radar establishment, Malvern, England specifically to engineer a semiconductor with a bandgap in the 8-12 micron atmospheric window [1-3]. It has since become the most important semiconductor for sensors and detectors in this region and beyond to the 3 to 30 μm range.

HgCdTe is a difficult material to synthesize due to the weak Hg-Te bond and the tendency towards formation of Te and HgTe precipitates and inclusions [4]. Considerable interest still exists in methods, especially non-destructive optical methods, of characterizing this material. Any optical test to assess electrical properties, such as mobility, μ, carrier concentration, N, conductivity, etc., requires that the effective mass, m*, of the carrier be known. The preferred method of measuring m* at higher than liquid helium temperatures is Faraday rotation (FR). In semiconductors Faraday rotation has two main components: one due to free carriers, called the plasma component, and one due to transitions across the bandgap, called the interband component. In narrow-gap semiconductors the interband component is large and significant well beyond the band edge. The free carrier component in the infrared is proportional to $N/m^{*2}$ and is immune to interfering influences such as defects and scattering mechanisms [13]. Separation of the free carrier component to allow determination of the effective mass has been problematic and the reason m*, has so far, not been measured systematically in HgCdTe at temperatures above liquid helium temperature. The industry and the literature report only theoretical band edge effective mass, $m^*_{be}$ calculations based on Kane's theory [9-10]. Due to the non-parabolic nature of the conduction band, it was expected that m* at higher temperature would be significantly larger than $m^*_{be}$ [12]. Ahrenkiel and Elizarov [11-12] found m* to be larger than $m^*_{be}$ by a factor of two at room temperature. To screen for carrier concentration and other electrical properties at higher temperatures, it is essential that the effective mass be known at those temperatures.

Initially in this work, Faraday rotation measurements were made at room temperature using a $CO_2$ laser capable of sustained output at wavelengths, λ, between 9.3 and 10.6 microns [159(4*), 197(5*), 202(6*), 318(9*)]. Measurements were made at individual wavelengths, 9.3, 9.6, 10.3 and 10.6 μm. The signal was chopped at 100 Hz and extracted with a lock-in amplifier to increase signal to noise to mitigate instabilities and mode hopping in the laser. The Faraday rotation components were separated using a linear plot method assuming a $\lambda^{-2}$ dependence for the interband component and a $\lambda^2$ dependence for the free carrier component. These experiments yielded a compensation factor, m**, of 2.14, where

$m^* = m^{**}m^*_{be}$, in good agreement with Ahrenkiel and Elizarov. The method is accurate and adequate for a laboratory environment but clumsy and slow and not amenable to automation with currently available equipment.

A device and method was developed by adding a dc magnet, polarizer/analyzer pair, and other optical elements to a Fourier Transform Infrared Spectrometer (FTIR) to generate high resolution Faraday rotation spectra between 5 and 20 μm [199(1*), 200(2*), 201(3*), 318(9*)]. The slope of the linear portion of the infrared Faraday rotation spectrum of a narrow gap semiconductor such as HgCdTe or InSb gives $N/m^{*2}$ unambiguously, from which either carrier concentration or m* may be derived, if the other is known, and has a number of advantages: separation of the free carrier component of the Faraday rotation spectrum is achieved automatically; determination of the slope of the high resolution spectra can typically be achieved within 5% allowing determination of N within 5% or m* within 2-3%; the measurement is minimally sensitive to multiple internal reflection; the method is fast, accurate, nondestructive, and easily automated. The device was used to systematically measure m* in HgCdTe at temperatures between 77 K and 296 K and Cd mole fractions, x, between 0.20 and 0.30 [199(1*), 200(2*), 201(3*)]. The factor, m**, relating empirical values with theoretical band edge effective mass values, $m^*_{be}$, was derived from the measurements to be $4.52 \times 10^{-3}$ T + 0.78. The compensation factor, m**, at 296 K is equal to 2.12 in good agreement with previous results using the $CO_2$ laser apparatus. This will be useful generally in the study of HgCdTe and will allow screening of carrier concentration in HgCdTe at any temperature. Effective masses in n-type InSb and GaAs were measured using the FTIR slope method and compared to literature values to validate the method.

A device and method [323] was proposed for measuring Faraday rotation in thin films to make Faraday rotation and the methods developed in this work useful in examining modern materials and devices that use thin semiconductor films. Since Faraday rotation is linearly dependent on thickness, thin films used in modern devices give little or no signal. The proposed device was based on the nonreciprocal nature of Faraday rotation to exploit multiple internal reflection in the sample, which is maximally occurring in thin films, and multiple passes through the sample using mirrored chambers to multiply the signal many times and in effect amplify the signal significantly. The device was submitted for a patent as a concept only and as yet has not been built or characterized.

Carrier concentrations were measured in all samples using Hall tests. Hall tests require electrical contacts to the material. Soldered contacts to HgCdTe can result in a massive

infusion of carriers from the indium solder and drastic decrease in mobility in this very high mobility material. A "cold contact" technique was devised where indium is burnished onto the material without heat or contamination to get accurate measurements and preserve expensive samples [199(1*)]. Contamination is especially critical in modern devices that use HgCdTe thin films.

The resonant spin flip Faraday rotation effect is a huge rotation that has been observed in HgCdTe and InSb at liquid helium temperatures. This effect has been modeled by authors as linear with carrier concentration [203, 204(7*), 206]. A semi classical model of the components of Faraday rotation that included the free carrier (plasma) component (Eq. (36)) and two interband components; one independent of carrier concentration (Eq. (40)) that will be called the "interband" component, and the resonant spin flip component (Eq. (49)), in HgCdTe and InSb was pieced together from the literature and compared to experimental results. The model was examined with the objective of using the huge spin rotation observed in HgCdTe and InSb as a means of measuring carrier concentration. The combination of interband (without spin) and plasma components of the model alone, appear to predict actual experimental results in HgCdTe and InSb fairly well especially at higher temperatures. The spin component of the model appears to be inconsistent with actual results in most cases especially at higher temperatures. The spin flip, interband, and small plasma component models were more successfully verified with observations at liquid helium temperatures near the bandgap energy by Aggarwal. The only carriers present at this temperature are the residual n-type carriers. The intrinsic carriers are frozen out to insignificant levels. The spin flip and interband components are both infinite singularities at the bandgap energy with similar wavelength dependencies and are impossible to separate. But very near the bandgap, the spin flip, according to the model, far exceeds the interband to the point where the interband component becomes negligible in the total rotation. Here the spin flip component and N can be measured without interference. But this point is very near the bandgap and requires knowledge of x in HgCdTe to within $\Delta x = \pm 0.0002$ and wavelength, $\Delta\lambda < 14$ nm. These requirements are probably not practical for measuring N. Also, the spin flip component has only been observed at liquid helium temperatures, although theoretically it could be observed at any temperature. Measurements of carrier concentration at liquid helium temperature and projection to higher temperatures is probably not particularly accurate or reliable in HgCdTe.

According to classical theory, a free carrier's mobility is proportional to a ratio of its Faraday rotation, $\theta$, and its absorption, $\alpha$ [13]. The beauty of this relationship is that

mobility can be measured using a combination of two simple measurements, using different scans of the same apparatus, without knowledge of the refractive index, the effective mass, or the carrier concentration of the material. The problems with this measurement are that the ratio, $\theta/\alpha$, must be due to only to one carrier, either electron or hole, and that the proportionality is only known for the classical regime where the measuring light energy is smaller than the energy of the carrier, i.e. $\hbar\omega < kT$, where k is the Boltzman constant. The FTIR region of the infrared spectrum between 5 and 20 microns, is in the quantum regime where $\hbar\omega > kT$. The proportionality in the quantum regime is very complex but adequate models for HgCdTe, InSb, GaAs, Si and Ge exist in the literature to derive it. In this work, the proportionality was measured for particular n-type InSb, GaAs, Si and Ge samples vs. temperature [200(2*), 201(3*), 202(6*)]. An absorption cross section taken from the literature was used to determine the proportionality in intrinsic and low doped n-type HgCdTe and InSb. These narrow gap semiconductors contain large amounts of natural carriers, both holes and electrons. The effective mass of holes in both these materials is significantly larger than electrons so the Faraday rotation due to holes is insignificant compared to electrons. However, absorption of holes is much larger than electrons. Also, the wavelength dependence of absorption for holes and electrons is very similar in these materials [129] so that there is no way to separate them. Therefore, the absorption part of the ratio had to be calculated for intrinsic and slightly n-type HgCdTe and InSb. The method can be used to measure mobility in n-type HgCdTe where electrons out number holes by 100 to 1 or more. For x = 0.20 in $Hg_{1-x}Cd_xTe$ this corresponds to a doping level of $N \geq 10^{17}$ $cm^{-3}$. In n-InSb it was found the method could be used to determine mobility (figure 53) for doping concentrations of $N \geq 20 \times 10^{16}$ $cm^{-3}$.

The effective mass ratios in Si and Ge are too large to obtain a strong rotation signal with the magnetic fields used. Consequently, Faraday rotation spectra obtained were too noisy to use the slopes. Effective masses were calculated, summed, and averaged, point by point using rotations in relatively smooth, flat regions of the spectra roughly between 10 and 15 μm. The bandgap in Si is 1.14 eV and 0.67 eV in Ge [356-357]. The interband rotation effect on the effective mass measurements was considered negligible at these wavelengths.

Faraday rotation and m* measurements using the slope of the spectra, that is the $CO_2$ linear plot and the FTIR slope methods above, were not corrected for multiple internal reflection (MIR). Two extreme examples where MIR was expected to be maximized, that is, in samples with low rotation and low absorption, were corrected for MIR using formulas found in the literature [217, 224-225]. The resulting corrections were negligible or within

the experimental variability normally encountered in these measurements. It was not exhaustively tested or proven that the slope method is immune to MIR, but these examples and examples in the literature seem to show this. Using the slopes of Faraday rotation spectra appears at least to be significantly less susceptible to MIR. Si and Ge measurements had to be corrected for MIR since they were averaged individual measurements. Correction factors were 5-6% in lower doped Si samples were the effect is maximal and 6-7% in the Ge sample between 77 K and 296 K.

## References


[1] P. Norton, Opto-Electronics Review **10**, 159 (2002).
[2] D. Long and J. L. Schmit, Mercury-Cadmium Telluride and Closely Related Alloys, in *Semiconductors and Semimetals*, eds. R. K. Willardson and A. C. Beer, vol. 5, p. 175 (Academic, New York 1970).
[3] A. Rogalski, Infrared Physics and Technology **43**, 187 (2002).
[4] A. Rogalski, J. Appl. Phys. **93**, 4355 (2003).
[5 ] W. Abdelhakiem, J. D. Patterson, and S. L. Lehoczky, Materials Letters **11**, 47 (1991).
[6 ] J. D. Patterson, W. A. Gobba, and S. L. Lehoczky, J. Mater. Res. **7**, 2211 (1992).
[7 ] Y. Sha, C. Su, and S. L. Lehoczky, J. Appl. Phys**. 81**, 2245 (1997).
[8 ] W. G. Spitzer and H. Y. Fan, Phys. Rev. **106**, 882 (1957).
[9] M. H. Weiler, Magneto-Optical Properties of $Hg_{1-x}Cd_xTe$ Alloys, in *Semiconductors and Semimetals*, eds. R. K. Willardson and A. C. Beer, vol. 16, p. 119 (Academic, New York 1981).
[10] D. G. Seiler, C. L. Littler, and M. H. Weiler, *Semiconductors and Semimetals*, eds. D. G. Seiler and C. L. Littler, vol. 36 (Academic, Boston 1992)**.**
[11] R. K. Ahrenkiel, P. Weiss, D. Watkins, S. K. Gulati and W. W. Granneman, J. Appl. Phys. **49**, 2265 (1978).
[12] A. I. Elizarov, E. K. Martynchuk, V. A. Petryakov and F. F. Sizov, J. Appl. Spectrosc. **41**, 1416 (1984).
[13] T. S. Moss, G. J. Burrell, and B. Ellis, *Semiconductor Opto-Electronics*, p. 23 (New York: Wiley 1973),.
[14] T. S. Moss, T. D. F. Hawkins. And G. J. Burrell, J. Phys. C: Solid State Phys.**1,** 1435 (1968).
[15] E. D. Palik and G. B. Wright, Free Carrier Magneto-Optical Effects, in *Semiconductors and Semimetals*, eds. R. K. Willardson and A. C. Beer, vol. 3, p. 421 (New York: Academic 1967).
[16] D. Zahn, Reflection Difference Techniques, in *Epioptics, Linear and Nonlinear Optical Spectroscopy of Surfaces and Interfaces*, J. F. McGlip, D. Weaire, C. H. Patterson eds., p. 77 (New York, Springer 1995).
[17] S. Schirar, L. Bayo, A. Melouah, J. Bougnot, C. Llinares, A. Montaner, and M. Galtier, Thin Solid Films **155**, 125 (1987).
[18] W. G. Spitzer and J.M. Whelan, Phys. Rev. **114**, 59 (1959).
[19] J. F. Black, E. Lanning, and S. Perkowitz, Infrared Physics **10**, 125 (1970).
[20] S. Perkowitz and J. Breecher, Infrared Physics **13**, 321 (1973).
[21] R. T. Holm, J. W. Gibson, and E. D. Palik, J. of Appl. Phys **48**, 212 (1977).
[22] J. K. Kung and W. G. Spitzer, J. Electrochem. Soc: Solid State Science and Technology **121**, 1482 (1974).
[23] D. B. Kushev and N. N. Zheleva, Semicond. Sci. Technol. **8**, S322 (1993).
[24] M. B. Thomas and J. C. Woolley, Can. J. Phys. **49**, 2052 (1971).
[25] B. Rheinländer, Phys. Stat. Sol. **38**, 193 (1970).
[26] V. Gopal, Infrared Physics **21**, 101 (1981).
[27] R. M. Culpepper and J. R. Dixon, J. Opt. Soc. of Am. **58**, 96 (1968).

[28] G. P. Boronina, M. A. ll'in, P. Yu. Karasev, V. Ya. Kovarskii, A. V. Laptev, A. V. Naumov, Industrial Laboratory **54**, 953 (1989).
[29] G. Carelli, N. Ioli, A. Messina, A. Moretti, S. Schepis, and F. Strumia, International J. of Infrared and Millimeter Waves **19**, 1191 (1998).
[30] Y. B. Li, R. A. Stradling, T. Knight, J. R. Birch, R. H. Thomas, C. C. Phillips, and I. T. Ferguson, Semicond. Sci. Technol. **8**, 101 (1993).
[31] L. C. Barcus, A. Perlmutter, and J. Callaway, Phys. Rev. **111**, 167 (1958).
[32] K. Okada and T. Oku, Jap. J. Appl. Phys. **6**, 276 (1967).
[33] V. V. Nelayev, G. V. Litvinovich, and B. B. Sevruk, SPIE **3345**, 55 (1997).
[34] M. Schubert, T. Hofmann, and C. Herzinger, J. Opt. Soc. Am. A **20**, 347 (2003).
[35] P. Grosse, B. Harbecke, B. Heinz, W. Jantz, and M. Maier, Appl. Phys. A **50**, 7 (1990).
[36] U. Nowak, J. Saalmüller, and W. Richter, Appl. Phys. A. **35**, 27 (1984).
[37] J. K. Kung and W. G. Spitzer, J. Electrochem. Soc.: Solid-State Science and Technology **121**, 1485 (1974).
[38] T. Hofmann, M. Schubert, and C. M. Herzinger, SPIE **4779**, 90 (2002).
[39] E. P. Rashevskaya, V. I. Fistul', and M. G. Mil'vidskii, Soviet Physics-Solid State **8**, 2515 (1967).
[40] M. B. Thomas and J. C. Woolley, Can. J. of Phys **49**, 2052 (1971).
[41] C. Pickering, J. Phys. C: Solid State Phys. **13**, 2959 (1980).
[42] R. Ferrini, G. Guizzetti, M. Patrini, A. Bosacchi, S. Franchi, and R. Magnanini, Solid State Communications **104**, 747 (1997).
[43] U. Nowak, J. Saalmueller, W. Richter, M. Heyen, H. Janz, Appl. Phys. A: Solids and Surfaces **A35**, 27 (1984).
[44] A. Zeng, J. E. Eldridge, C. Lavoie, and T. Tiedje, Solid State Communications **87**, 1039 (1993).
[45] Z. C. Feng, Y. T. Hou, S. J. Chua, and M. F. Li, Surface and Interface Analysis **28**, 166 (1999).
[46] E. Frayssinet, W. Knap, P. Prystawko, M. Leszczynski, I. Grzegory, T. Suski, B. Beaumont, P. Gibart, Journal of Crystal Growth **218**, 161 (2000).
[47] J. P. Lavine, F. C. Lo, F. Moser, E. C. Burkey, and F. T. J. Smith, Proceedings -The Electrochemical Society **80-5**, 96 (1980).
[48] L. E. Howarth and J. F. Gilbert, J. Appl. Phys. **34**, 236 (1963).
[49] A. H. Tong, P. A. Schumann Jr., and W. A. Keenan, J. of the Electrochemical Society **119**, 1381 (1972).
[50] H. Bergner, V. Brueckner, and B. Schroeder, Optical and Quantum Electronics **14**, 245 (1982)
[51] R. Bernini, L. Zeni, R. Pierri, SPIE **4099**, 31 (2000).
[52] M. Geddo, D. Maghini, A. Stella, M. Cottini, J. Electrochem. Soc. **133**, 1414 (1986).
[53] S. Hava and M. Auslender, SPIE **1972**, 210 (1993).
[54] E. E. Gardner, W. Kappallo, and C. R. Gordon, Appl. Phys. Lett. **9**, 432 (1966).
[55] W. G. Spitzer, G. W. Gobeli, and F. A. Trumbore, J. Appl. Phys. **35**, 206 (1964).
[56] F. R. Kessler, U. Barkow, U. Paetzold, Physica Status Solidi (A) Appl. Res. **92**, k37 (1985).
[57] L. Xiangyang, Z. Jianhua, Z. Wenjuan, J. Runqing, X. Yueyuan, H. Xiaoning, Z. Jun, L. Huiqing, H. Xinwen, F. Jiaxiong, SPIE **3437**, 284 (1998).

[58] I. M. Nesmelova, N. S. Baryshev, F. P. Volkova, and A. P. Cherkasov, Soviet Physics-Semicond. **6**, 822 (1972).
[59] T. C. Harman, A. J. Strauss, D. H. Dickey, M. S. Dresselhaus, G. B. Wright, and J. G. Mavroides, Phys. Rev. Lett. **7**, 403 (1961).
[60] J. Kavaliauskas, G. Krivaite, D. Senuliene, and A. Šileika, phys. stat. sol. (a) **126**, K201 (1991).
[61] J. Kavaliauskas, G. Krivaite, R. Mickunas, and A. Shileika, Lithuanian J. of Phys. **32**, 159 (1992).
[62] J. Kavaliauskas, G. Krivaite, R. Mickunas, Sov. Phys.-Collection **30**, 551 (1990).
[63] G. Eidžiūnas, J. Kavaliauskas, G. Krivaitė, and A. Šileika, phys stat. sol. (a) **107**, K75 (1988).
[64] J. Kavaliauskas, L. Bovina, E. Gurauskas, A. Šileika, Lietuvos Fizikos Rinkinys **17**, 605 (1977) (in Russian).
[65] P. A. Schumann, Jr. and R. P. Phillips, Solid-State Electronics **10**, 943 (1967).
[66] K. Peter, G. Willeke, K. Prasad, A. Shah, and E. Bucher, Philosophical Mag. B **69**, 197 (1994)
[67] H. Fujiwara, M. Kondo, and A. Matsuda, Appl. Phys. Lett. **82**, 1227 (2003).
[68] Y. Mishima, M. Hirose, and Y. Osaka, J. Appl. Phys. **51**, 1157 (1980).
[69] R. W. Miles, Electron and hole effective masses in HgCdTe, in *Properties of Narrow Gap Cadmium based Compounds*, Ed. P. Capper, emis Datareview Seris, No. 10, p. 215 (INSPEC, London 1994).
[70] Seeger, K., Semiconductor Physics, An Introduction, Fourth Ed., Ch. 4 p. 46, Ch. 6 p. 153, Ch. 11 p. 302 (New York:Springer-Verlag 1989).
[71] H. Y. Fan and M. Becker, Semiconducting Materials, H. K. Henisch, ed., p. 132 (Butterworth, London 1951).
[72] H. Y. Fan, Rept. Progr. Phys **19**, 107, (1956).
[73] H. Y. Fan, Effects of Free Carriers on Optical Properties, in *Semiconductors and Semimetals*, eds. R. K. Willardson and A. C. Beer, vol. 3, p. 405 (New York: Academic 1967).
[74] L. H. Hall, J. Bardeen, and F. J. Blatt, Phys. Rev. **95**, 559 (1954).
[75] I. C. Cheeseman, Proc. Phys. Soc. A **65**, 25 (1952).
[76] E. Haga and H. Kimura, J. Phys. Soc. Japan **19**, 1596 (1964).
[77] E. Haga and H. Kimura, J. Phys. Soc. Japan **18**, 777 (1963).
[78] W. P. Dumke, Phys. Rev. **124**, 1813 (1961).
[79] E. Haga and H. Kimura, J. Phys. Soc. Japan **19**, 658 (1964).
[80] H. Brooks, *Adv. Electronics Electron Phys.*, vol. VII, 85 (Academic Press, N. Y. 1955).
[81] R. DE L. Kronig, Proc. R. Soc. **133**, 245 (1931).
[82] R. DE L. Kronig, Proc. R. Soc. **133**, 255 (1931).
[83] H. Y. Fan, W. Spitzer, and R. J. Collins, Phys. Rev. **101**, 566 (1956).
[84] W. Heitler, *The Quantum Theory of Radiation*, 3rd ed., p. 242 (Oxford University Press, London 1954).
[85] R. Wolfe, Proc. Phys Soc. **A67**, 74 (1954).
[86] L. J. Slutsky and C. A. Swenson, Phys. Rev. **113**, 167 (1959).
[87] R. F. Potter, Phys. Rev. **103**, 47 (1956).

[88] Yu. A. Burenkov, Yu. M. Burdukov, S. Yu. Davidov, and S. P. Nikanorov, Sov. Phys. Solid State **15**, 1175 (1973).
[89] A. Dargys and J. Kundrotas, *Handbook on Physical Properties of Ge, Si, GaAs, and InP* (Vilnius Science and Encyclopedia Publishers 1994).
[90] P. H. Nguyen, K. R. Hofmann, and G. Paasch, J. Appl. Phys. **94**, 375 (2003).
[91] H. J. McSkimin, J. Appl. Phys. **24**, 988 (1953).
[92] S. P. Nikanorov, Yu. A. Burenkov, and A. V. Stepanov, *Sov*. Phys. Solid State **13**, 2516 (1971).
[93] F. J. Morin and J. P. Martin, Phys. Rev. **96**, 28 (1954).
[94] O. V. Vakulenko and M. P. Lisitsa, Soviet Phys.-Solid State **9**, 769 (1967).
[95] S. Perkowitz, J. Appl. Phys. **40**, 3751 (1969).
[96] S. Perkowitz, J. Phys. Chem. Solids **32**, 2267 (1971).
[97] H. Ehrenreich, Phys. Rev. **120**, 1951 (1960).
[98] S. M. Sze and J. C. Irvin, Solid State Electronics **11**, 599 (1968).
[99] K. Osamura and Y. Murakami, Jap. J. Appl. Phys. **11**, 365 (1972).
[100] J. Bardeen and W. Shockley, Phys. Rev. **80**, 72 (1950).
[101] S. Visvanathan, Phys. Rev. **120**, 376 (1960).
[102] S. Visvanathan, Phys. Rev. **120**, 379 (1960).
[103] R. Rosenberg and M. Lax, Phys. Rev. **112**, 843 (1958).
[104] W. Walukieticz, J. Lagowski, L. Jastrzebski, M. Lichensteiger, and H. C. Gatos, J. Appl. Phys. **50**, 899 (1979).
[105] W. Walukieticz, J. Lagowski, and H. C. Gatos, J. Appl. Phys. **53**, 769 (1982).
[106] L. Jastrzebski, J. Lagowski, W. Walukieticz, and H. C. Gatos, J. Appl. Phys. **51**, 2301 (1980).
[107] M. G. Mil'vidskii, V. B. Osvenskii, E. P. Rashevskaya, and T. G. Yugova, Soviet Physics-Solid State **7**, 2784 (1966).
[108] E. P. Rashevskaya and V. I. Fistul', Soviet Physics-Solid State **9**, 1443 (1967).
[109] B. Jensen, Annals of Physics **80**, 284 (1973)
[110] B. Jensen, phys. stat. sol. (b) **86**, 291 (1978).
[111] H. J. G. Meyer, J. Phys. Chem. Solids **8**, 264 (1959).
[112] H. Y. Fan and P. Fisher, J. Phys. Chem. Solids **8**, 270 (1959).
[113] H. J. G. Meyer, Phys. Rev. **112**, 298 (1958).
[114] Z. A. Demidenko, Solid State Comm. **8**, 533 (1970).
[115] R. von Baltz and W. Escher, phys. stat. sol. (b) **51**, 499 (1972).
[116] B. Jensen, Solid State Comm. **9**, 1587 (1971).
[117] H. J. Ehrenreich, J. Phys. Chem. Solids **2**, 131 (1956).
[118] S. W. Kurnick and J. M. Powell, Phys. Rev. **116**, 597 (1959).
[119] D. Kranzer and E. Gornik, Solid State Comm. **9**, 1541 (1971).
[120] W. Szymanska, and J. P. Maneval, Solid State Comm. **8**, 879 (1970).
[121] Y. J. Jung, M. K. Park, S. I. Tae, K. H. Lee, and H. J. Lee, J. Appl. Phys. **69**, 3109 (1991).
[122] K. Tsukioka, Jap. J. Appl. Phys. **25**, 1258 (1986).
[123] J. J. Whalen and C. R. Westgate, Appl. Phys. Lett. **15**, 292 (1969).
[124] E. M. Gershenzon, I. N. Kurilenko, L. B. Litvak-Gorskaya, and R. I. Rabinovich, Soviet Physics- Semiconductors **7**, 1005 (1974).

[125] R. Asauskas, Z. Dobrovol'skis, and A. Krotkus, Soviet Physics- Semiconductors **14**, 1377 (1980).
[126] W. Kaiser and H. Y. Fan, Phys. Rev. **98**, 966 (1955).
[127] G. W. Gobeli and H. Y. Fan, Phys. Rev. **119**, 613 (1960).
[128] E. Blount, J. Callaway, M. Cohen, W. Dumke, and J. Phillips, Phys. Rev. **101**, 563 (1956).
[129] J. A. McOczkowski and D. A. Nelson, J. Appl. Phys. **54**, 2041 (1983).
[130] E. Finkman and S. E. Schacham, J. Appl. Phys. **56**, 2896 (1984).
[131] E. Finkman and Y. Nemirovsky, J. Appl. Phys. **50**, 4356 (1979).
[132] C. A. Hougen, J. Appl. Phys. **66**, 3763 (1989).
[133] V. Gopal, R. Ashokan, and V. Dhar, Infrared Phys. **33**, 39 (1992).
[134] J. G. Tian, C. P. Zhang, and G. Y. Zhang, Appl. Phys. Lett. **59**, 2591 (1991).
[135] E. Gurauskas, J. Kavaliauskas, G. Krivaitė, and A. Šileika, phys. stat. sol. (b) **115**, 195 (1983).
[136] Q. Dingrong, T. Wenguo, S. Jie, C. Junhao, and Z. Guozhen, Solid State Comm. **56**, 813 (1985).
[137] Q. Dingrong, phys. stat. sol. (a) **94**, 573 (1986).
[138] Q. Dingrong and W. Szuszkiewicz, Philosophical Mag. Lett. **55**, 147 (1987).
[139] S. Goettig, Solid State Comm. **55**, 611 (1985).
[140] B. Jensen, J. Phys. Chem. Solids **34**, 2235 (1973).
[141] B. V. Dutt, M. Al-Delaimi, and W. G. Spitzer, J. Appl. Phys. **47**, 565 (1976).
[142] B. M. Vul, A. F. Plotnikov, V. M. Sal'man, A. A. Sokolova, and V. A. Chapnin, Soviet Physics-Semiconductors **2**, 1045 (1969).
[143] Q. Dingrong and T. Wenguo, Chinese J. Infrared Res. Series B **7**, 13 (1988).
[144] J. Baars and F. Sorger, Solid State. Comm. **10**, 875 (1972).
[145] D. Long, Phys. Rev. **176**, 923 (1968).
[146] E. Burstein, Phys. Rev. **93**, 632 (1954).
[147] T. S. Moss, Proc. Phys. Soc. Lond. **B67**, 775 (1954).
[148] A. S. Filipchenko, D. N. Nasledov, L. N. Radaikina, and I. I. Ratner, phys. stat. sol. (a) **A14,** 71 (1972).
[149] P. Y. Yu and M. Cardona, *Fundamentals of Semiconductors*, p. 324 (Springer-Verlag, Berlin 1996).
[150] J. Isenberg and W. Warta, Appl. Phys. Lett **84**, 2265 (2004).
[151] D. K. Schroder, R. N. Thomas, and J. C. Swartz, IEEE Transactions Electron Devices **ED-25**, 254 (1978).
[152] Y. Mishima, M. Hirose, Y. Osaka, J. Appl. Phys. **51**, 1157 (1980).
[153] Y. Mishima, T. Hamasaki, H. Kurata, M. Hirose, and Y. Osaka, Jap. J. Appl. Phys. **20**, L121 (1981).
[154] P. A. Schumann, Jr., W. A. Keenan, A. H. Tong, H. H. Gegenwarth, and C. P. Schneider, J. Electrochem. Soc. **118**, 145 (1971).
[155] L. Jastrzebski, J. Lagowski, H. C. Gatos, J. Electrochem. Soc. **126**, 260 (1979).
[156] W. Spitzer and H. Y. Fan, Phys. Rev. **108**, 268 (1957).
[157] V. S. Vavilov, *Soviet Phys-Solid State* **12**, 346 (1960).
[158] A. H. Khan, Phys. Rev. **97**, 1647 (1955).
[159(4*)] F. W. Clarke, SPIE **2554**, 97 (1995).

[160] S. Usui and N. Kikuchi, J. Non-Crystalline Solids **34**, 1 (1979).
[161] T. Watanabe, T. Sameshima, K. Nakahata, T. Kamiya, and I. Shimizu, Thin Solid Films **383**, 248 (2001).
[162] M. Heintze, E. Lotter, C. D. Abel, M. B. Schubert, Mat. Res. Soc. Symp. Proc. **452**, 815 (1997).
[163] D. K. Ferry, Phys. Rev. B **14**, 1605 (1976).
[164] H. Piller, Faraday Rotation, in *Semiconductors and Semimetals*, eds. R. K. Willardson and A. C. Beer, vol. 8, p. 103 (Academic, New York 1972).
[165] E. W. J. Mitchell, Proc. Phys. Soc. London **68**, 973 (1955).
[166] T. S. Moss and A. K. Walton, Infrared Faraday Effect in Semiconductors, in *Proc. Intl. Conf. on Semicond. Phys. Prague 1960,* p. 338 (Academic, New York 1961).
[167] T. S. Moss, phys. stat. sol. **2**, 601 (1962).
[168] S. D. Smith and C. R. Pidgeon, Ellipticity Associated with Free Carrier Faraday Rotation in Semiconductors, in *Proc. Intl. Conf. on Semicond. Phys.*, *Prague 1960,* p. 342 (Academic, New York 1961).
[169] M. J. Stephen and A. B. Lidard, J. Phys. Chem. Solids **9**, 43 (1958).
[170] M. I. Klinger and M. M. Chaban, Soviet Phys.- Tech. Phys. **1**, 921 (1956).
[171] C. R. Pidgeon amd S. D. Smith, Infrared Physics **4**, 13 (1964).
[172] L. R. Ingersoll and W. L. James, Rev. of Sci. Inst. **24**, 23 (1953).
[173] B. J. Zook and C. R. Pollock, Applied Optics **28**, 1991 (1989).
[174] B. Donovan and T. Medcalf, Physics Lett. **7**, 304 (1963).
[175] B. Donovan and T. Medcalf, Brit. J. Appl. Phys. **15**, 1139 (1964).
[176] H. Piller, J. Appl. Phys. **37**, 763 (1966).
[177] H. Piller, High Temperature Magneto-Optical Investigations of Gallium Arsenide Conduction Bands with Coherent Radiation, in *Ninth Int'l Conf. on Phys. of Semicond., Moscow*, vol. 1, p. 353 (Nauka, Leningrad,1968).
[178] C. J. Gabriel, Applied Optics **10**, 2332 (1971).
[179] E. D. Palik, J. R. Stevensen, and J. Webster, J. Appl. Phys. **37**, 1982 (1966).
[180] B. Donovan and J. Webster, Proc. Phys. Soc. London **78**, 120 (1961).
[181] B. Donovan and J. Webster, Proc. Phys. Soc. London **79**, 46 (1962).
[182] B. Donovan and J. Webster, Proc. Phys. Soc. London **81**, 90 (1963).
[183] R. W. Ure Jr., Thermoelectric Effects in III-V Compounds, in *Semiconductors and Semimetals*, eds. R. K. Willardson and A. C. Beer, vol. 8, p. 67. (Academic, New York 1972).
[184] H. S. Bennett and E. Stern, Phys. Rev. **137**, A448 (1965).
[185] Yu. I. Ukhanov, Soviet Physics-Usp **16**, 236 (1973).
[186] M. Balkanski and E. Amzallag, phys. stat. sol. **30**, 407 (1968).
[187] J. K. Furdyna and M. E. Brodwin, Phys. Rev. **124**, 740 (1961).
[188] E. D. Palik, B. W. Henvis, and R. F. Wallis, Magneto-Optical Studies of Semiconductors Using Polarized Radiation, in *Proc. Intl. Conf. Phys. Semicond*. , Exeter 1962, ed. A. G. Strickland, p. 288. (The Institute of Physics and The Physical Society, London 1962)
[189] B. Lax and S. Zwerdling, Magneto-Optical Phenomena in Semiconductors, in *Prog. In Semicond.*, vol. 5**,** p. 221 (New York, John Wiley & Sons Inc. 1960).
[190] L. Ŝniadower, J. Raułusziewicz, and R. R. Gałązka, phys. stat. sol. **6**, 549 (1964).

[191] H. A. Lyden, Phys. Rev. **134,** A1106 (1964).
[192] E. D. Palik, Applied Optics **2**, 527 (1963).
[193] S. Teitler, E. D. Palik, and R. F. Wallis, Phys. Rev. **123**, 1631 (1961).
[194] S. Teitler amd E. D. Palik, Phys. Rev. Lett. **5**, 546 (1960).
[195] A. I. Elizarov, E. K. Martynchuk, and V. A. Petryakov, phys. stat. sol. (a) **125**, K47 (1991).
[196] A. Sh. Abdinov, G. S. Seidli, E. B. Khydyrova, and N. M. Shukyurov, J. Inorganic Mat. **23,** 1616 (1987).
[197(5*)] A. J.Syllaios, J. M. Anderson, L. Colombo, C. L. Littler, G. J. Brostow, C. R. Christensen, J. A. Grisham, and F. W. Clarke, SPIE **2228**, 309 (1994).
[198] J. K. McDonald, G. A. Tanton, J. A. Grisham, C. R. Christensen, and A. J. Syllaios, SPIE **2228**, 316 (1994).
[199(1*)] F. W. Clarke, S. Balevičius, J. K. McDonald, and J. A. Grisham, SPIE **5564**, 73, (2004).
[200(2*)] F.W. Clarke, Journal of Electronic Materials **26**, 592 (1997).
[201(3*)] F.W. Clarke, SPIE **2775**, 197 (1996).
[202(6*)] F. W. Clarke, J. Appl. Phys. **75**, 4319 (1994).
[203] S. Y. Yuen, P. A. Wolff, P. Becla, and D. Nelson, J. Vac. Sci. Technol. **A5**, 3040 (1987).
[204(7*)] A. J. Syllaios, C. L. Littler, X. N. Song, V. C. Lopes, C. R. Christensen, J. A. Grisham, and F. W. Clarke, Semicond. Sci. Technol. **8**, 953 (1993).
[205] R. Dornhaus and G. Nimtz, *The Properties and Applications of the Hg1-xCdxTe Alloy System*, in *Narrow-Gap Semiconductors*, *Springer Tracts in Modern Physics*, vol. 98, p. 119 (Springer-Verlag, Berlin 1983).
[206] R. L. Aggarwal, R. F. Lucey Jr., and D. P. Ryan-Howard, Appl. Phys. Lett. **53**, 2656 (1988).
[207] S. D. Smith, T. S. Moss, and K. W. Taylor, J. Phys. Chem. Solids **11**, 131 (1959).
[208] T. S. Moss, S. D. Smith, and K. W. Taylor, J. Phys. Chem. Solids **8**, 323 (1959).
[209] S. D. Smith, C. R. Pidgeon, and V. Prosser, Temperature Dependence of Effective Mass in InSb: A Detailed Study of Free Carrier, Interband, and Oscillatory Faraday Rotation in Germanium, in *Proc. Intl. Conf. Phys. Semicond.*, Exeter, 1962, ed. A. G. Strickland, p. 301 (The Institute of Physics and The Physical Society, London 1962).
[210] Yu. I. Ukhanov and Yu. V. Mal'tsev, Soviet Phys.-Solid State **4**, 2354 (1963).
[211] F. P. Kesamanly, Yu. V. Mal'tsev, D. N. Nasledov, Yu. I. Ukhanov, and A. S. Filipchenko, Soviet Phys. –Solid State **8**, 938 (1966).
[212] Yu. I. Ukhanov and Yu. V. Mal'tsev, Soviet Phys.-Solid State **5**, 2144 (1964).
[213] A. K. Walton and P. L. Reimann, J. Phys. C: Solid State Phys. **3**, 1410 (1970).
[214] H. Piller and R. F. Potter, Phys. Rev. Lett. **9**, 203 (1962).
[215] Yu. I. Ukhanov, Soviet Physics-Solid State **4,** 2010 (1963).
[216] H. Stramska, Z. Bachan, P. Byszewski, and J. Kolodziejczak, phys. stat. sol. **27**, K25 (1968).
[217] T. H. Lee and H. Y. Fan, Phys. Rev. **165**, 927 (1968).
[218] A. K. Walton and T. S. Moss, Proc. Phys. Soc. **78**, 1393 (1961).
[219] A. K. Walton and T. S. Moss, J. Appl. Phys **30**, 951 (1959).
[220] A. K. Walton and C. R. Everett, Solid State Comm. **4**, 211 (1966).

[221] I. M. Boswarva and A. B. Lidiard, Faraday Rotation in Germanium, in *Proc. Intl. Conf. Phys. Semicond. Exeter 1962*, ed. A. G. Strickland, p. 308 (The Institute of Physics and The Physical Society, London 1962).
[222] M. Cardona, Phys. Rev. **121**, 752 (1961).
[223] Yu. P. Mashukov, Soviet Physics-Semiconductors **1**, 828 (1968).
[224] R. R. Alfano and D. H. Baird, J. Appl. Phys. **39**, 2931 (1968).
[225] H. Piller, Electron Effective Mass in Gallium Arsenide as a Function of Doping, in *Proc. Intl. Conf. Phys. of Semicond, Kyoto*, J. of Physical Soc. of Japan Supplement **21,** 206 (1966).
[226] Yu. I. Ukhanov, Soviet Phys-Solid State **5**, 75 (1963).
[227] T. S. Moss and A. K. Walton, Proc. Phys. Soc. **74**, 131 (1959).
[228] C. Constantinescu and S. Nan, phys. stat. sol. (a) **18**, 277 (1973).
[229] E. D. Palik, S. Teitler, and R. F. Wallis, J. Appl. Phys. Supplement **32**, 2132 (1961).
[230] B. Lax and J. G. Mavroides, Interband Magneto-Optical Effects, in *Semiconductors and Semimetals*, eds. R. K. Willardson and A. C. Beer, vol. 3, p. 321 (Academic, New York 1967).
[231] E. Conwell and V. F. Weisskopf, Phys. Rev **77**, 388 (1950).
[232] E. M. Conwell, Proc.of the I.R.E. **40**, 1327 (1952).
[233] E. M. Conwell, Proc. of the I.R.E. **46**, 1281 (1958).
[234] P. P. Debye and E. M. Conwell, Phys. Rev. **93**, 693 (1954).
[235] H. Brooks, Phys. Rev. **83**, 879 (1951).
[236] C. Erginsoy, Phys. Rev. **79**, 1013 (1950).
[237] V. Karpus, Soviet Physics-Semicond. **20**, 6 (1986).
[238] V. Karpus**,** Semiconductor Science and Technology **5**, 691 (1990).
[239] V. Karpus and D. Lehmann, Semiconductor Science and Technology **12**, 781 (1997).
[240] E. O. Kane, J. Phys. Chem. Solids **1**, 249 (1956).
[241] H. Ehrenreich, J. Phys. Chem. Solids **2**, 131 (1957).
[242] P. Pfeffer and W. Zawadzki, Physica Status Solidi (B): Basic Research **88**, 247 (1978).
[243] W. Zawadzki and W. Szymanska, J. Phys. Chem. Solids **32**, 1151 (1971).
[244] W. Zawadzki and W. Szymanska, phys. stat. sol. (b) **45**, 415 (1971).
[245] J. Kossut, Physica Status Solidi (B): Basic Research **72**, 359 (1975).
[246] D. J. Howarth and E. H. Sondheimer, Proc. Royal Soc. **A219** , 53 (1953).
[247] E. Litwin-Staszewska, W. Szymanska, R. Piotrzkowski, Physica Status Solidi (B): Basic Research **106**, 551 (1981).
[248] W. Szymanska and T. Dietl, J. Phys. Chem. Solids **39,** 1025 (1978).
[249] K. M. Demchuk and I. M. Tsidilkovskii, phys. stat. sol. (b) **82**, 59 (1977).
[250] A. A. Kokin and V. I. Tolstikhin, Soviet Microelectronics **13**, 8, (1984).
[251] O. Ozabas, M. Akarsu, Turkish J. of Phys. **26**, 283 (2002).
[252] V. W. L. Chin, R. J. Egan, and T. L. Tansley, J. Appl. Phys. **69**, 3571 (1990).
[253] E. Preuss, Phys. Rev B **1**, 3392 (1970).
[254] M. Oszwaldowski, J. Phys. and Chem. Solids **46**, 791 (1985).
[255] E. M. Gershenzon, I. N. Kurilenko, L. B. Livak-Gorskaya, and R. I. Rabinovich, Soviet Phys-Semiconductors **7,** 1005 (1974).
[256] H. Morisaki, Y. Inuishi, Physical Soc. of Japan Journal **20**, 1814 (1965).

[257] M. Oszwaldowski, Thin Solid Films **56**, 331 (1979).
[258] N. Kotera, J. Shigeta, K. Narita, T. Oi, K. Hayashi, K. Sato, IEEE Transactions on Magnetics **MAG-15**, 1946 (1979).
[259] R. G. van Welenis and B. K. Ridley, Solid-State Electronics **27,** 113 (1984).
[260] R. W. Miles, Electron and hole mobilities in HgCdTe, in *Properties of Narrow Gap Cd-based Compounds*, ed. P. Capper, EMIS Datareviews Series, No. 10, p. 221 (INSPEC, London 1994).
[261] J. J. Dubowski, T. Dietl, W. Szymanska, and R. R. Galazka, J. Phys. Chem. Solids **42**, 351 (1981).
[262] J. R. Meyer and F. J. Bartoli, J. Vac. Sci. Technol. **21**, 237 (1982).
[263] S. Krishnamurthy and Arden Sher, J. Appl. Phys. **75**, 7904 (1994).
[264] D. Chattopadhyay and B. R. Nag, J. Appl. Phys. **45**, 1463 (1974).
[265] B. R. Nag, phys. stat. sol. (b) **66**, 719 (1974).
[266] S. D. Yoo and K. D. Kwack, J. Appl. Phys. **81**, 719 (1997).
[267] G. Nimtz, G. Bauer, R. Dornhaus, and K. H. Muller, Phys. Rev. B **10**, 3302 (1974).
[268] M. Averous, *phys. stat. sol. (b)* **95**, 9 (1979).
[269] B. L. Gel'mont, V. I. Ivanov-Omskii, B. T. Kolomiets, V. K. Ogorodnikov, and K. P. Smekalova, Soviet Physics-Semiconductors **5**, 228 (1971).
[270] W. Scott, J. Appl. Phys. **43,** 1055 (1972).
[271] C. T. Elliot and I. L. Spain, J. Phys. C: Solid State Phys. **7**, 727 (1974).
[272] W. M. Higgins, G. N. Pultz, R. G. Roy, and R. A. Lancaster, J. Vac. Sci. Technol. **A7**, 271 (1989).
[273] N. T. Gordon, S. Barton, P. Capper, C. L. Jones, and N. Metcalfe, Semicond. Sci. Technol. **8**, S221 (1993).
[274] A. Schenk, phys. stat. sol. (a) **122**, 413 (1990).
[275] S. L. Lehoczky, C. J. Summers, F. R. Szofran, B. G. Martin, Mat. Res. Soc. Symposia Proc. **9**, 421 (1982).
[276] S. L. Lehoczky (private communication).
[277] S. L. Lehoczky, J. G. Broerman, D. A. Nelson, and C. R. Whitsett, Phys. Rev. B **9**, 1598 (1974).
[278] W. Szymanska, Electron Scattering and Transport Phenomena in Narrow Gap Mercury Compounds and Alloys, in *Physics of Narrow-Gap Semiconductors*, *Proc. III Intl. Conf., Warszawa 1977,* p. 357 (Elsevier, Amsterdam 1978).
[279] T. Dietl and W. Szymanska, J. Phys. Chem. Solids **39**, 1041 (1978).
[280] J. A. Nelson, J. G. Broerman, C. J. Summers, and C. R. Whitsett, Phys. Rev. **18**, 1658 (1978).
[281] R. J. Iwanowski, T. Dietl, and W. Szymanska, J. Phys. Chem. Solids **39**, 1059 (1978).
[282] D. L. Rode, Low-Field Electron Transport, in *Semiconductors and Semimetals*, eds. R. K. Willardson and A. C. Beer, vol. 10, p. 1 (Academic, New York, 1975).
[283] B. Pelliciari, G. L. Destefanis, and L. Di Cioccio, J. Vac. Sci. Technol. **A7**, 314 (1989).
[284] K. K. Parat, N. R. Taskar, I. B. Bhat and S. K. Ghandhi, J. of Crys. Growth **102**, 413 (1990).

[285] R. Dornhaus, H. Happ, K. H. Muller, G. Nimtz, W. Schlabitz, P. Zaplinski, and G. Bauer: in *Proc. XII Int. Conf. Phys. Semicond*., Stuttgart 1974, ed. M. H. Pilkuhn, p. 1157 (Teubner, Stuttgart 1974).
[286] W. Hoerstel, A. Klimakov, R. Kramer, and A. Schmiede, phys. stat. sol. (a) **119**, 589 (1990).
[287] M. C. Chen, S. G. Parker, and D. F. Weirauch, J. Appl. Phys. **58**, 3150 (1985).
[288] D. S. Pan and Y. Lu, Appl. Phys. Lett. **53**, 307 (1988).
[289] M. C. Chen, S. G. Parker, and D. F. Weirauch, Appl. Phys. Lett. **54**, 1480 (1989).
[290] J. H. Basson and H. Booyens, Semicond. Sci. Technol. **3**, 150 (1988).
[291] E. D. Palik and R. T. Holm Nondestructive Evaluation of Semiconductor Materials and Devices, *Proceedings of NATO Summer School*, ed. J. N. Zemel, p. 315 (Plenum Press, New York 1978).
[292] R. R. Rau and M. E. Caspari, Phys. Rev. **100**, 632 (1955).
[293] J. K. Furdyna and S. Broersma, Phys. Rev. **120**, 1995 (1960).
[294] J. M. Goldey and S. C. Brown, Phys. Rev. **98**, 1761 (1955)
[295] K. S. Champlin, Physica **28,** 1143 (1962).
[296] H. Stuhl and L. R. Walker, Phys. Rev. **122** (1952).
[297] A. Bouwknegt and J. Volger, Physica **30**, 113 (1964).
[298] M. E. Baldwin and T. J. Burgess, Appl. Phys. Lett. **5**, 224 (1964).
[299] A. M. Portis, J. Phys. Chem. Solids **8,** 326 (1959).
[300] R. Mansfield and M. R. Borst, *Brit*. J. Appl. Phys. **16**, 570 (1965).
[301] J. White, R. J. Dinger, and H. H. Wieder, J. Appl. Phys. **38**, 3171 (1967).
[302] D. J. White, J. Appl. Phys. **39**, 5083 (1968).
[303] D. M. Zengin, J. of Phys D: Applied Physics **16**, 653 (1983).
[304] P. J. Allen, Rev. Sci. Instr. **25**, 394 (1954).
[305] I. Ogawa, K. Yamada, T. Idehara, A. Tsiushima, and S. Yamaguchi, Intl. J. Infrared and Millimeter Waves **24**, 651 (2003).
[306] B. A. Johnson, Plasmas in Semiconductors and Semimetals*,* in *Semiconductors and Semimetals*, eds. R. K. Willardson and A. C. Beer, vol. 1, Ch. 11, p. 379. (Academic, New York 1966)
[307] R. Bowers and M. C. Steele, Proc. IEEE **52**, 1105 (1964).
[308] E. D. Palik and J. K. Furdyna, Rep. Prog. Phys. **33**, 1193 (1970).
[309] J. K. Furdyna, Appl. Optics **6,** 675 (1967).
[310] J. K. Furdyna, Rev. Sci. Inst. **37,** 462 (1966).
[311] A. Laurinavičius, P. Malakauskas, and J. Požela, Intl. J. of Infrared and Millimeter Waves **7**, 573 (1987).
[312] A. Laurinavičius, J. Požela, and R. Tolutis, Helicon Diagnostics of Narrow-Band Semiconductor Quality, in *Proc. 10th World Conf. Non-Destructive Testing, Moscow 1982*, p 265. (Moscow, R.S.F.S.R. 1982).
[313] A. Laurinavičius, J. Požela, and A. Vitkus, Application of Microwave Helicons for Diagnostics of Narrow-Band Semiconductors, in *Proc. Intl. Symp. Microwave Diagnostics of Semicond. Porvoo, Finland*, Medd.-Sven. Tek. Vetenskapsaked. Finl **31**, 250 (1977).
[314] J. D. Wiley and R. N. Dexter, Phys. Rev. **181**, 1181 (1969).
[315] R. S. Brazis, J. K. Furdyna, and J. K. Požela, phys. stat. sol. (a) **53**, 11 (1979).
[316] R. S. Brazis, J. K. Furdyna, and J. K. Požela, phys. stat. sol. (a) **54**, 11 (1979).

[317] R. S. Brazis and J. K. Furdyna, J. Appl. Phys. **48**, 4267 (1977).
[318(9*)] J. A. Grisham, F. W. Clarke, C. R. Christensen, and J. L. Stensby, *"Modulated High Sensitivity Infrared Polarimeter"*, U. S. Patent 5,210,417. May 11, 1993.
[319] G. A. Tanton, J. A. Grisham, *"High-Sensitivity Infrared Polarimeter"*, U. S. Patent number 4,818,881. April 4, 1989.
[320] G. A. Tanton, J. A. Grisham, C. R. Christensen, and S. Razi, Proc. SPIE **505**, 221 (1984).
[321] J. A. Stensby, Electronics and Computer Engineering Dept., The University of Alabama in Huntsville, Huntsville, AL., (private communication).
[322(8*)] F. W. Clarke, J. K. McDonald, C. R. Christensen, and J. A. Grisham, *"Device and Method for Performing an Optical Hall Test"*, U. S. Patent 5,907,401. May 25, 1999.
[323] F. W. Clarke and S. Balevičius, *"Multiple Pass Faraday Rotation Amplifier"*, patent application submitted Aug. 2005.
[324] E.H. Hall, Am. J. Math. **2**, 287 (1879).
[325] L. J. van der Pauw, Phillips Res. Repts. **13**, 1 (1958).
[326] V. I. Fistul, *Heavily Doped Semiconductors*, p. 77 (New York: Plenum 1969).
[327] American Society for Testing Materials, ASTM, Standard Test Methods for Measuring Resistivity and Hall Coefficient and Determining Hall Mobility in Single Crystal Semiconductors, Designation F76-86 (1986).
[328] M. B. Reine, Principle Engineering Fellow, BAE Systems, 2 Forbes Rd., Lexington, Mass., (private communication).
[329] W. F. H. Micklethwaite, J. Appl. Phys. **63**, 2382 (1988).
[330] G. L. Hansen, J. L. Schmit, and T. N. Casselman, J. Appl. Phys. **53**, 7099 (1982).
[331] W. M. Higgins, G. N. Pultz, R. G. Roy, R. A. Lancaster, and J. L. Schmit, J. Vac. Sci. Technol. **A7**, 271 (1989).
[332] M. B. Reine, K. R. Maschhoff, S. P. Tobin, P. W. Norton, J. A. Mroczkowski, and E. E. Krueger, Semicond. Sci. Technol. **8**, 788 (1993).
[333] J. H. Basson and H. Booyens, Semicond. Sci. Technol. **3**, 150 (1988).
[334] G. L. Hansen and J. L. Schmit, J. Appl. Phys. **54**, 1639 (1983).
[335] D. A. Nelson, W. M. Higgins, and R. A. Lancaster, SPIE **225**, 48 (1980).
[336] P. W. Kruse, Indium Antinomide Photoconductive and Photoelectromagnetic Detectors, in *Semiconductors and Semimetals*, eds. R. K. Willardson and A. C. Beer, vol. 5, p. 15 (Academic, New York, 1970).
[337] C. Hilsum and A. C. Rose-Innes, *Semiconducting III-V Compounds*, in *International Series of Monographs on Semiconductors*, p. 114 (Pergamon Press, New York 1961),
[338] G. Masetti, M. Severi, and S. Solmi, IEEE Trans. Electr. Devices **ED-30**, 764 (1983).
[339] N. D. Arora, J. R. Hauser, and D. J. Roulston, IEEE Trans. Electr. Devices **ED-29**, 292 (1982).
[340] F. Mousty, P Ostoja, and Passari, J. Appl. Phys. **45**, p. 4576 (1974).
[341] G. Baccarani, and P. Ostoja, Solid-State Electron. **18**, p. 579 (1975).
[342] C. Jacobi, C. Canali, G. Ottaviani, and A. A. Quaranta, Solid-State Electronics **20**, 77 (1977).
[343] Dr. David C. Look, Professor, Wayne State University Research Institute (private communication).
[344] A. S. Jordan, Met. Trans. **1**, 239 (1970).

[345] V. G. Smith, W. A. Tiller, and J. W. Rutter, Can. J. Phys. **33**, 723 (1953).
[346] B. Lax and Y. Nishina, Suppl. J. Appl. Phys **32**, 2128 (1961).
[347] L.M. Roth, Phys. Rev. **133**, A542 (1964).
[348] H. J. Jiménez-González, R. L. Aggarwal, and G. Favrot, Phys. Rev. B. **49**, 4571 (1994).
[349] R. Romestain, S. Geschwind, and G. E. Devlin, Phys Rev. Lett **35**, 803 (1975).
[350] P. S. Pershan, J. P. van der Zeil, and L. D. Malmstrom, Phys Rev**. 143,** 574 (1966).
[351] Y. R. Shen and N. Bloembergen, Phys. Rev. **143**, 372 (1966).
[352] M. H. Weiler J. Magn. Magn. Mater. **11**, 131, (1979).
[353] CRC *Handbook of Laser Science and Technology*, ed. Marvin Weber, v. 3, p. 106. (CRC, Boca Raton, FL 1986).
[354] M. Born and E. Wolf, *Principles of Optics*, (Pergamon Press, Oxford 1970).
[355] W. Grevendonk, P. Van Den Keybus, G. Ruymbeek, and B. Vanhuyse, Physica **100 B**, 88 (1980).
[356] M. E. Levinshtein, S. L. Rumyantsev, M. S. Shur, *Properties of Advanced Semiconductor Materials GaN, AlN, InN, BN, SiC, SiGe*, p. 149 (John Wiley & Sons, Inc., New York 2001).
[357] Y. M. Niquet, C. Delerue, G. Allan, and M. Lanno, Phys. Rev. B **62**, 5109 (2000).

# LIST OF PUBLICATIONS

The main results of the research described in this dissertation have been published in the following scientific journals and proceedings of the international conferences:

1* F. W. Clarke, S. Balevičius, J. K. McDonald, and J. A. Grisham, Measurement of electron effective mass ratios in $Hg_{1-x}Cd_xTe$ for $0.20 \leq x \leq 0.30$ between 77 K and 296 K (Invited Paper), SPIE **5564**, 73 (2004). ISSN 0277-786X, ISBN 0-8194-5502-4.

2* F.W. Clarke, An Optical Alternative to the Hall Test, Journal of Electronic Materials **26**, 592 (1997). ISSN 0361-5235.

3* F.W. Clarke, An Optical Characterization Technique for N-type Semiconductors, Including Infrared Detector and Other Optical Materials, SPIE **2775**, 197 (1996). ISBN 0-8194-2160-X.

4* F. W. Clarke, A Nondestructive Characterization Technique for Most N-type Semiconductors, Including Infrared Detector Materials, SPIE **2554**, 97 (1995). ISBN 0-8194-1913-3

5* A.J. Syllaios, J.M. Anderson, L. Colombo, C.L. Littler, G.L. Brostow, C.R. Christensen, J.A.Grisham, and F.W. Clarke, Magneto-optical characterization of HgCdTe thin films, SPIE **2228**, 309 (1994). ISBN 0-8194-1532-4.

6* F.W. Clarke, Nondestructive Determination of Free Electron Concentration and Mobility in $Hg_{1-x}Cd_xTe$, n-Type InSb and N-type GaAs, Journal of Applied Physics **75**, 4319 (1994). ISSN 0021-8979.

7* A.J. Syllaios, C.L. Littler, X.N. Song, V.C. Lopes, CR. Christensen, J.A.Grisham, and F.W. Clarke, Faraday Rotation Analysis of HgCdTe, Semicond. Sci. Technol. **8**, 953 (1993). ISSN 0268-1242.

**Patents Awarded**

8* Frederick W. Clarke, Joseph K. McDonald, Charles R. Christensen and John A.Grisham, Device and Method for Performing an Optical Hall Test, Patent 5,907,401, May 25, 1999.

9* John A. Grisham, Frederick W. Clarke, Charles R. Christensen, and John L.Stensby, Modulated High Sensitivity Infrared Polarimeter, Patent 5,210,417, May 11, 1993.

**Other publications not included in the dissertation**

10*A. K. Sood, R. Singh, Y. R. Puri, F. W. Clarke, O. Laboutin, P. Deluca, R. Welser, T. J. Deng, and J. C. M. Hwang, Growth and Characterization of AlGaN/GaN Epitaxial Layers by MOCVD on SiC Substrates for RF Device Applications, SPIE **6121**, 107 (2006). ISBN 0-8194-6163-6.

11*A. K. Sood, R. Singh, Y. R. Puri, F. W. Clarke, A. Dabiran, P. Chow, T. J. Deng, and J. C. M. Hwang, Design and Development of MBE Growth AlGaN/GaN HEMT Devices on SiC Substrates for RF Applications, Mat. Res. Soc. Symp. Proc. **892**, FF-13-12 (2006).

12*S. Balevičius, N. Žurauskienė, V Stankevič, S. Keršulis, J. Novickij, L. L. Altgibers, and F. Clarke, High Pulsed Magnetic Field Sensor Based on La-Ca-Mn-O Thin Polycrystalline Films, ACTA Physica Polonica A **107**, 207 (2005). ISSN 0587-4246.

13*A. K. Sood, E. J. Egerton, Y. R. Puri, F. W. Clarke, J. C. M. Hwang, A. Dabiran, and P. Chow, Development of High Performance AlGaN/GaN High Electron Mobility Transistors for RF Applications, SPIE **5550**, 130 (2004). ISBN 0277-786X. ISBN 0-8194-5488-5

14*Frederick W. Clarke, Fat Duen Ho, M. Asif Khan, Grigory Simin, J. Yang, Remis Gaska, Michael S. Shur, Jianyu Deng, and S. Karmalkar, Gate Current Modeling for Insulating Gate III-N Heterostructure Field Effect Transistors, Mat. Res. Soc. Symp. Proc. **743**, L9.10 (2002). ISSN 1-55899-680-X.

15*J. Milton Harris, John R. Moffatt, Martha G. Case, Frederick W. Clarke, Judith S. Polley, Thomas K. Morgan, Jr., Thomas M. Ford, and Roger K. Murry, Jr., Reactivity of Geometrically Constrained Cyclopropylcarbinyl and Homoallyl Substrates. Solvolysis of 2,4-Dehydro-5-homoadamantyl and 2-Homoadamant-4-enyl Derivatives, J. Org. Chem. **47**, 2740 (1982). ISSN 0022-3263.

**Patents Awarded**

16*Henry C. Allen and Frederick W. Clarke, Tetra-Alkyl Titanates as Bonding Agents for Thermoplastic Propellants, Patent 4,597,924, July 1, 1986.

# Santrauka (abstract in Lithuanian)

Disertaciją sudaro įvadas, trys skyriai, apibendrinimas ir pagrindinės išvados, cituojamos literatūros sąrašas, mokslinių darbų disertacijos tema sąrašas ir santrauka lietuvių kalba.

**Įvade** pagrįstas darbo aktualumas, nurodyti pagrindiniai darbo tikslai, spręsti uždaviniai, mokslinis naujumas ir ginamieji teiginiai.

**I skyriuje** pateikta literatūros apžvalga. Čia apžvelgti pagrindiniai optiniai (infraraudonosios srities) metodai, naudojami krūvininkų koncentracijos N ir judrio μ matavimams puslaidininkiuose. Šioje disertacijos dalyje taip pat apžvelgiami infraraudonosios srities absorbcijos koeficiento, kuris svarbus proporcingumo koeficiento C tarp μ ir θ/α nustatymui klasikinio ir kvantinio artėjimų atvejais, matavimai tokiose medžiagose: HgCdTe, InSb, GaAs, Si ir Ge. Taip pat trumpai apžvelgiami mikrobangų ruožo Faradėjaus sukimo ir helikoninių bangų tyrimai puslaidininkiuose.

**II skyriuje** pateikti trijų Faradėjaus efekto tyrimo metodikų aprašymai. Pirmoji metodika yra skirta padidinti signalo ir triukšmų santykį ir išmatuoti Faradėjaus sukimą, esant skirtingiems bangų ilgiams λ. Taip pat pateiktas antrosios metodikos aprašymas. Ši metodika leido patobulinti Faradėjaus efekto tyrimus, papildomai šalia Fourier infraraudonosios srities spektrometro (FTIR) panaudojant magnetą ir poliarizatoriaus-analizatoriaus porą ir taip gauti didelės skiriamosios gebos Faradėjaus sukimo spektrus. Trečioji Faradėjaus efekto matavimo metodika yra skirta Faradėjaus efekto tyrimams plonuosiuose sluoksniuose. Šios metodikos tikslas – sustiprinti Faradėjaus efektą, naudojant vidinį atspindį ir veidrodžius, kuriais spindulys daug kartų nukreipiamas į bandinį. Šiame skyriuje taip pat aprašoma "šaltojo kontakto" metodika, skirta atlikti Holo matavimams. Indžio kontaktai, pasižymintys stabilumu ir omiškumu iki žemų temperatūrų (10 K), gali būti uždėti ant n-tipo HgCdTe, InSb, Si, ir Ge be papildomo atkaitinimo, siekiant išvengti medžiagos užteršimo. Tai ypač svarbu didelio judrio medžiagoms, tokioms kaip HgCdTe ir InSb, kuriose, lituojant kontaktus, dėl kaitimo gali padidėti krūvininkų koncentracija ir sumažėti judris.

**III skyriuje** pateikti eksperimentiniai Faradėjaus efekto tyrimai ir absorbcijos matavimai n-tipo HgCdTe, InSb, GaAs, Si, ir Ge, siekiant nustatyti krūvininkų koncentraciją ir judrį. Kiekvienam bandiniui, įskaitant ir HgCdTe, buvo išmatuota efektinė masė. Tai pirmieji, kiek žinoma, sisteminiai m* tyrimai $Hg_{1-x}Cd_xTe$ temperatūrų ruože nuo 77 K iki 296 K ir x vertėms: $0{,}20 \leq x \leq 0{,}30$. Taip pat pateikti „pataisos" koeficiento m** skaičiavimai, kuris sieja efektinę masę m* su teorine efektine mase $m^*_{be}$, nustatyta ties laidumo juostos dugnu. Taip pat buvo nustatytas proporcingumo koeficientas C tarp laisvųjų elektronų judrio ir santykio tarp Faradėjaus sukimo ir absorbcijos koeficiento, esant tam tikriems infraraudonosios srities bangų ilgiams n-tipo HgCdTe, InSb, GaAs, Si, ir Ge. Tai leidžia nustatyti tiriamų bandinių judrį, atliekant du paprastus matavimus: Fardėjaus spektrų polinkio kampo ir absorbcijos koeficiento matavimus, nežinant N, n arba m*. HgCdTe ir

InSb atveju abi medžiagos pasižymi didele nuosava krūvininkų koncentracija. Todėl neįmanoma išmatuoti atskirai skylių ir elektronų absorbcijos koeficientų. Tuo būdu šis metodas gali būti panaudotas, siekiant išmatuoti judrį n-HgCdTe, kur elektronų yra keliomis eilėmis daugiau, negu skylių. n-InSb buvo nustatyta, kad metodas gali būti panaudotas judriui nustatyti, kai $N \geq 20 \times 10^{16}$ $cm^{-3}$. Be to, buvo panaudotas kvaziklasikinis Faradėjaus efekto dedamųjų modelis HgCdTe ir InSb medžiagoms, sujungiant literatūroje pateiktas laisvųjų krūvininkų (plazminę), tarpjuostinę ir sukinio dedamąsias. Eksperimentiniai rezultatai buvo palyginti su teoriniais skaičiavimais, atliktais naudojant šį modelį. Gauta, kad tarpjuostinė ir plazminė dedamosios gerai aprašo eksperimentinius rezultatus HgCdTe ir InSb, ypač aukštesnėse temperatūrose, o sukinio dedamosios įskaitymas, ypač aukštesnėse temperatūrose, žymiai padidina eksperimento ir teorijos nesutapimą.

**Apibendrinime ir pagrindinėse išvadose** pateiktos bendrosios išvados ir rezultatai bei jų praktinio panaudojimo svarba.

**Literatūros sąraše** pateikti darbai, kurių rezultatai buvo apžvelgti ir cituojami šiame darbe.

**Mokslinių darbų sąraše** pateiktos disertacijos tema spausdintos publikacijos bei patentai.